A Comparative Look at Structure-Function Roles in Light-Harvesting Dynamics of Purple Bacteria

By

Ashley Tong

B.S. Biochemistry

Indiana University South Bend, 2014

SUBMITTED TO THE DEPARTMENT OF CHEMISTRY IN PARTIAL FULFILLMENT OF THE REQUIREMENTS FOR THE DEGREE OF

DOCTOR OF PHILOSOPHY IN CHEMISTRY

AT THE

MASSACHUSETTS INSTITUTE OF TECHNOLOGY

September 2019

Signature redacted

Signature of Author: ______________________

Ashley Tong

July 03, 2019

Signature redacted

Certified by: ______________________

Gabriela Schlau-Cohen

Assistant Professor of Chemistry

Thesis Supervisor

Signature redacted

Accepted by: ______________________

Robert Field

Hslam and Dewey Professor of Chemistry

Chair, Department Committee on Graduate Students

This doctoral thesis has been examined by a committee of the
Department of Chemistry as follows

Signature redacted

Professor Alex Shalek: ______ ______________________

Thesis Commitee Chair
Associate Professor of Chemistry

Signature redacted

Professor Gabriela Schlau-Cohen: ___ ______________

Thesis Supervisor
Assistant Professor of Chemistry

Signature redacted

Professor Cathy Drennan: _______ ______________

Thesis Committee Member
Professor of Biology and Chemistry

A Comparative Look at Structure-Function Roles in Light-Harvesting Dynamics of Purple Bacteria

By

Ashley Tong

Submitted to the Department of Chemistry on July 03, 2019 in Partial Fulfillment of the Requirements for the Degree of Doctor of Philosophy in Chemistry

Abstract

Using a unique approach to solar energy conversion, photosynthetic organisms have developed a light-harvesting process with near unity quantum efficiency. Light-harvesting proteins transfer energy from the sun to reach a central location, the reaction center, where charge separation occurs and energy is converted to chemical energy. Moreover, these proteins are able to carry out this efficient transfer in cellular membranes despite the complex environment found in these membranes. Particularly, light-harvesting in photosynthetic purple bacteria uses a diverse set of tools from species to species to efficiently transfer energy through this protein network. Induced by their habitats, external environmental pressures on the fitness of purple bacteria have caused species to evolve different mechanisms in order to deal with thesel pressures. Although these complexes have been studied for some time, there is still very little known about particular species. Additionally, most previous work has been on non-native samples, such as detergent solubilized proteins, or on complex membranes such as vesicles, chromatophores, or whole membranes that contain multiple proteins with multiple processes occurring simultaneously. This work investigates how photosynthetic light-harvesting complexes are able to achieve their impressive efficiency using ensemble ultrafast spectroscopy to measure energy transfer dynamics and near-native discoidal model membrane-discs. These model membrane-discs provide a controlled environment to effectively study how energy is transferred in a single protein and between particular sets of proteins, allowing individual steps in the light-harvesting process to be probed without other processes interfering. They also provide a near-native system to explore how lipid-protein and protein-protein interactions affect the energy transfer kinetics in these proteins. Additionally, this work explores the differences in energy transfer kinetics of light-harvesting proteins between species of purple bacteria. Overall, this provides new insights into the role the membrane plays in light-harvesting and how the composition of proteins within the native membrane of different species of purple bacteria can add variation to energy transfer kinetics.

Thesis Supervisor: Gabriela Schlau-Cohen

Title: Assistant Professor of Chemistry

Contents

Introduction

Photosynthesis powers most life on Earth and is responsible for the generation of over 100 gigatons of biomass on an annual basis [1, 2]. Photosynthetic purple bacteria convert light energy into chemical energy via a cyclic electron transport mechanism with >90% quantum efficiency [3, 4]. The photosynthetic machinery in purple bacteria contain light-harvesting antenna proteins LH2 and LH1 (Figure 1) [5–7]. LH2 is peripheral to the reaction center, while LH1 encircles the reaction center and directly interacts. These antennae absorb energy from light and funnel it to the reaction center where it is used to power the electron transport chain and synthesize ATP. It is in the first few steps of energy transfer within the photosynthetic antennae that >90% quantum efficiency is achieved. One of the fascinating features of the light-harvesting complexes of purple bacteria is that this efficiency is always maintained with major differences between complexes of different species and under various light conditions, even with light restriction. Although vital to photosynthetic biomass production, the *in vivo* dynamics of the initial energy transfer steps within this network have not been determined due to the intrinsic difficulties associated with production, purification, and sample preparation of membrane proteins. Specifically, producing spectroscopically amenable samples that mimic the *in vivo* membrane architecture and environment has proven challenging. While much research has been done to characterize the energy transfer dynamics within light-harvesting complexes, there has been little direct comparison of these complexes under the exact same experimental conditions. Also, given the wide diversity of differences between proteins across species, most research thus far has been done on only *Rhodopseudomonas (Rps.) acidophila* and *Rhodobacter (R.) sphaeroides.*

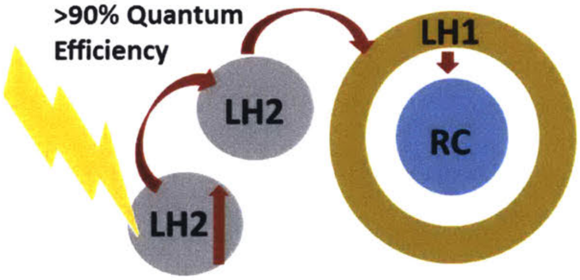

Figure 1: Light-Harvesting energy flow through the photosynthetic protein network in purple bacteria.

LH2 (Figure 2A) is a nonomer or an octomer of heterodimers (Figure 2B) consisting of two peptides (~100 amino acids each) known as the α and β peptides [8]. It contains two rings of bacteriochlorophyll a (BChla) that mediate the energy flow within the protein, three BChla per heterodimer. Each BChla has a central Mg^{2+} atom that serves a structural role [9]. One ring absorbs at 800 nm and is known as the B800 band. The other ring absorbs at 850 nm and is known as the B850 band. Two of the BChla in each heterodimer (one per peptide) make up the B850 band, while the third forms the B800 band. The BChla that makes up the B800 band is singly ligated by a carboxylated N-terminal methionine of the α peptide and is hydrogen bonded to β-Arg20, β-His12 and α-Gln3. The BChla of the B850 band are ligated by a single histidine, one from the α peptide and one from the β peptide, and hydrogen bonded by residues in both peptides as well. The B800 band BChlas lie parallel to the surface of the membrane, while those in the B850 band lie perpendicular. The BChla in the B850 band are held closer together and are more strongly coupled than those in the B800 band. One carotenoid per dimer is also present and aids in broadening the spectral window for light energy collection and also serves a photoprotective

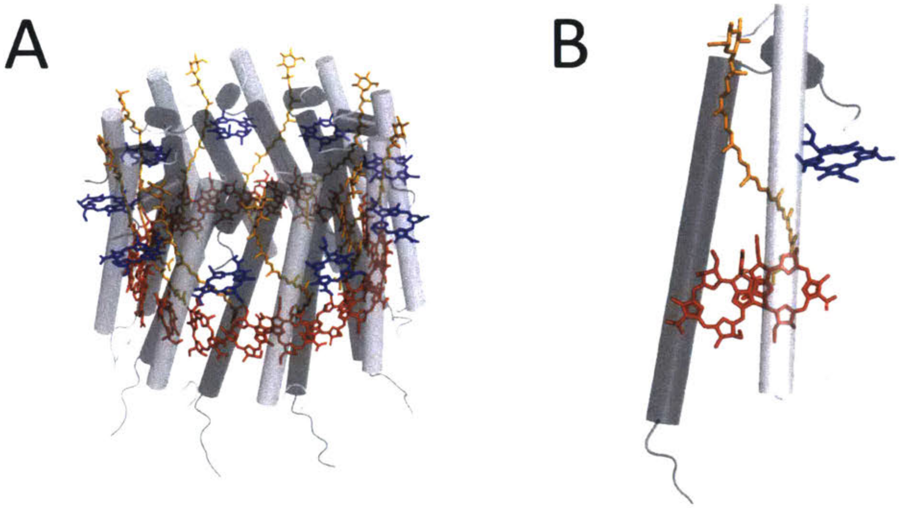

Figure 2: Structure of LH2. (A) Complete structure of LH2 from *Rsp. acidopillus* showing the organization of pigments. Dark gray shows the α peptide and light gray shows the β peptide. BChla in blue are part of the B800 ring and those in red are part of the B850 ring. (B) Hetero-dimer of LH2. Colors are the same as (A).

role [8,10]. Some species of purple bacteria contain spectral variations of the LH2 antennae known as LH3 [11–13]. These spectral variants have a blue-shifted B850 band, absorbing at 820 nm (B820 band) as shown in Figure 3. LH3 is produced under stressed conditions, such as low light and low temperature. Its major roles *in vivo* are to broaden the spectral range over which light can be absorbed and to increase the energy gap from the peripheral antennae to LH1, prohibiting back transfer to LH3 and increasing the overall efficiency of energy transfer [14,15]. LH3 can be present in varying ratios that depend on the stressed condition. The membrane can contain anywhere from 100% LH2 to almost 100% LH3 [16].

A high resolution structure of LH2 from *R. sphaeroides* is not available but projection structures from negative stain electron microscopy with resolution at 8 Å determined it to be a nonomer of heterodimers in resemblance to LH2 from *Rps. acidophilus* [17,18]. Additionally, these LH2 variants have a high sequence percent identity of 45% and 66% between the α and β subunits, respectively [19]. Thus, these two LH2 variants have similar energy transfer dynamics. In this work, LH2 from *Rps. acidophilla* will be used as the *R. sphaeroides* model. The structure of LH2 from *Ph. molischianum* reveals that is is an octomer of heterodimers, producing B800 pigments that are rotated 90° and have a 20° tilt with respect to *R. sphaeroides* B800 pigments (Figure 4A) [20]. The inter-ring distances of the B800 BChla and the closest B850 BChla are shorter for *R. sphaeroides* with Mg-Mg distances between B800 BChla and B850 BChla within a heterodimer being 18.4 and 20.2 Å for *R. sphaeroides* and *Ph. moliscianum*, respectively (Figure 4B). The Mg-Mg distances between B800 BChla and B850 BChla between adjacent heterodimers are 19.0 and 17.1 Å for *R. sphaeroides* and *Ph. moliscianum*, respectively. The 90° rotation of the B800 BChlas in *Ph. molischianum* align the transition dipoles to be parallel to the B850 BChlas' dipole moment, whereas the transition dipoles lie more perpendicular to each other in *R. sphaeroides* (Figure 4C). The intra-ring Mg-Mg distances are 21.2 and 22.0 Å for the B800 pigments and 9.2 and 8.7 Å for the B850 pigments for *Ph. molischianum* and *R. sphaeroides*, respectively [18,20].

The structure of LH3 from *Rps. acidophilla* shows an almost identical structure to the LH2

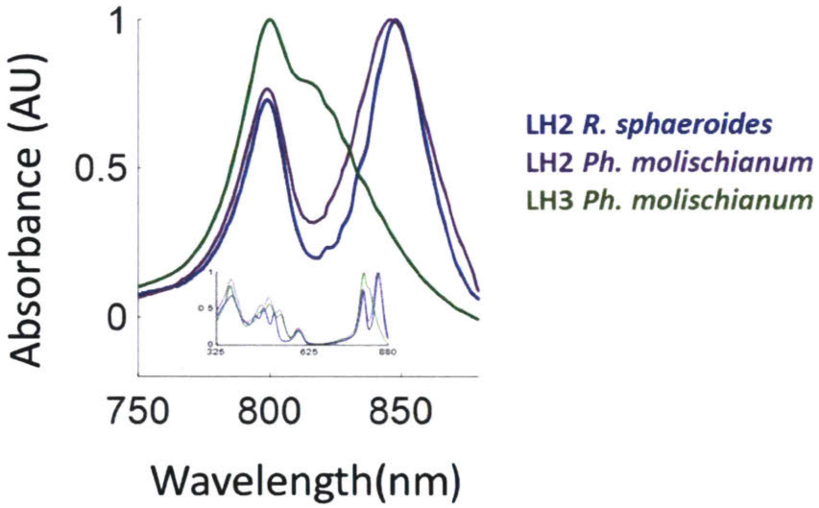

Figure 3: Linear absorption of all proteins showing difference in their spectral properties. In LH3 the 850 nm absorption is shifted to 820 nm.

from the same species [11, 14]. Interestingly, the overall pigment-protein interactions between the BChlas in the B800 and B850 are very similar in the two complexes. CD spectra report on the electronic structure of the B850 and B820 bands and are almost identical between LH2 and LH3 besides the wavelength dependent shift of the peak location in LH3 from 850 to 820 nm [21]. In fact, the peptide sequences are identical except for two amino acids in the α peptide of the heterodimer [22, 23]. The residue α-Tyr44 in LH2 is switched to α-Phe44 in LH3 and α-Trp45 of LH2 is changed to α-Leu45 in LH3. These two changes in amino acids restructures the hydrogen bonding network of the BChlas in the B850 band, blue-shifting the absorption to 820 nm (Figure 5A,B). Through site-directed mutagenesis and Raman spectroscopy, this has been attributed to the rotation of the C_3-acetyl chain of a BChla pigment out of the plane of the macrocycle (Figure 5C) [11, 14, 24, 25]. This rotated bond reduces the number of conjugated bonds in the macrocycle thus increasing the BChla's site energy [7, 26, 27].

To date, there have been a significant number of studies using spectroscopic methods to determine energy transfer rates within LH2 and other components of the photosynthetic apparatus of purple non-sulfur bacteria [15, 28–45]. Energy transfer rates from LH2 in *R. sphaeroides* were previously determined with transient absorption spectroscopy and anisotropy [46]. Energy transfer within the B800 and B850 bands was found to be ~450 fs and ~60 fs, respectively. Inter-band energy transfer from B800 to B850 was determined to be ~850 fs in detergent solubilized complexes. This rate was enhanced by 30% in a native-like membrane model system as will be discussed more in Chapter 2 [46]. These rates were in agreement with many past works [30, 33, 37, 47–51]. Energy transfer rates of LH2 from *Ph. molisciànum* has not been as well established as that from *R. sphaeroides* but has been shown to have similar rates as observed in *R. sphaeroides* with the B800-B850 energy transfer slightly longer (1-1.2 ps) [52–55]. Energy transfer taking place in the B800 band of LH2 has been described by de Caro *et al.* as a two-pool model [56]. In this model the B800 pigments are divided into two groups, one on the blue side and one on the red side of the B800 band. Pigments of the red pool can transfer exclusively to B850 and those in the blue pool can transfer energy via two pathways that compete with one another. The blue pool of BChlas can transfer to the red pool of BChlas in the B800 band and can also transfer energy directly to the

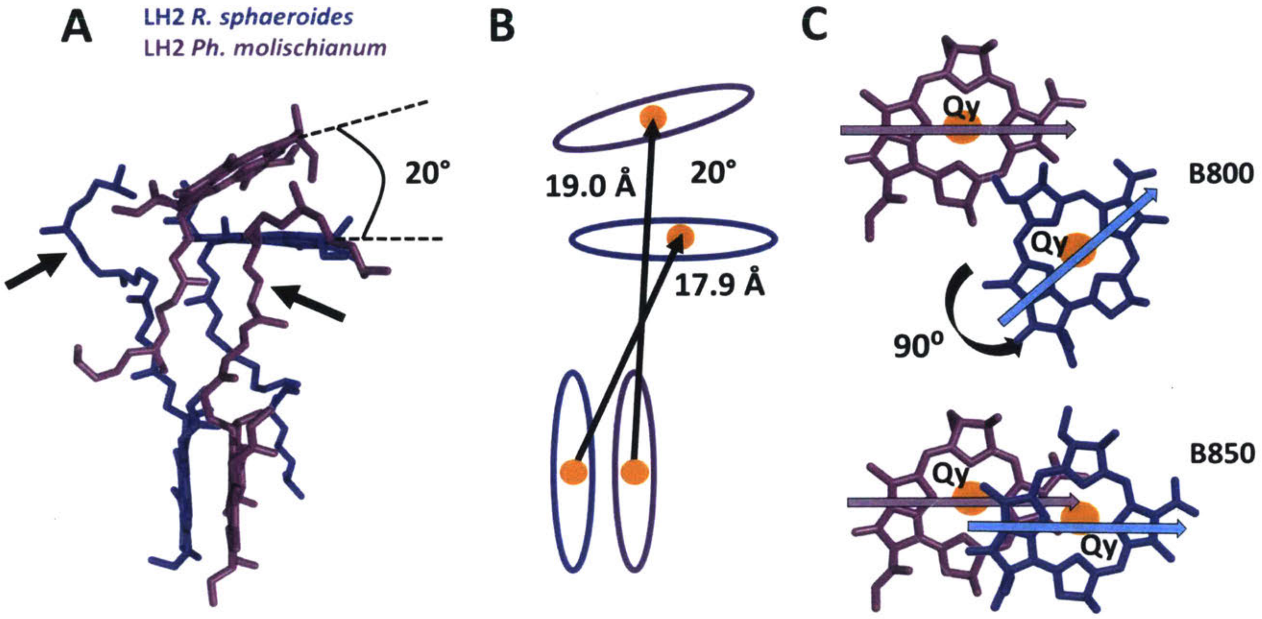

Figure 4: Differences in BChla orientations in *Rsp. acidophilla* (our *R. sphaeroides model*) and *Ph. moliscianum.* (A) Closest B800 and B850 BChlas showing 20° tilt between two species. Arrows point to a macrocycle substituent that is a long alkyl chain known as the phytol tail. (B) BChla schematic showing differences in Mg-Mg distances for two species. BChlas are depicted as ovals and Mg^{2+} atoms are depicted as orange circles. (C) Closest BChlas of the B800 and B850 bands showing changes in Qy dipole moments due to 90° rotation. The Qy dipole of B800 BChla in *Ph. moliscianum* better aligns with the Qy dipole of the B850.

B850 band [54, 56].

Energy transfer dynamics for LH3 *Ph. molischianum* have not been characterized in any previous work. Some information is available for LH3 in *Rps. acidophilus* which ultimately concludes that the energy transfer dynamics of LH3 is very similar to LH2 and that the large blue-shifted B820 does not have a substantial effect on the interband energy transfer [42, 57]. However, single-molecule fluorescence studies have shown distinctive heterogeneous spectral features in the B820 band of LH3 that are significantly different than LH2 [58]. This heterogeneity was ascribed to the sensitivity of the B820 BChlas to light-induced local conformational changes. The change in hydrogen bonding and rotation of the C_3-acetyl bond was suggested to be the cause of observed heterogeneity in the B820 band of single-molecule experiments because of the increase in conformational flexibility [58]. Compared to LH2, there is a red-shift of the upper excitonic energy level from 755 to 790 nm which is attributed to ~2-fold decrease in B820 intra-pigment coupling [42].

The energy transfer in LH2 and LH3 can be viewed as two types. The first is a non-coherent hopping mechanism between weakly coupled pigments as described by Förster theory, which can be described as energy transfer from a donor to an acceptor molecule whose rate is determined by the distance between the two [59]. The second is a coherent energy transfer mechanism between pigments or chromophores that are coupled to one another that is better described using Redfield

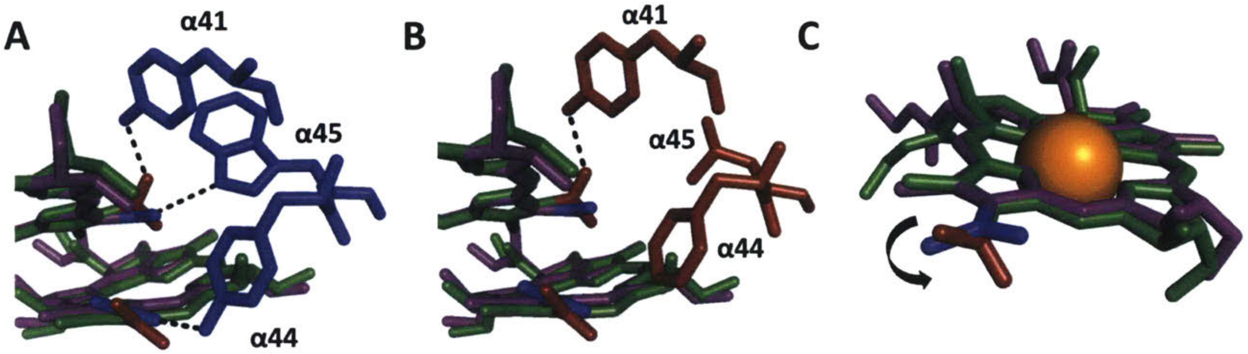

Figure 5: Restructuring of hydrogen bonding network in LH3 of *Rsp. acidophilla*. (A) B850 (purple) and B820 (green) BChlas showing hydrogen bonding framework of LH2 (blue). (B) B850 (purple) and B820 (green) BChlas showing hydrogen bonding framework of LH3 (red). (C) Rotation induced at C_3-acetyl bond due to loss of two hydrogen bonds.

theory [60]. Excitation energy transfer (EET) occurs within the B800 band, within the B850 band, and from the B800 to B850 band within LH2. The B850 band has a higher lying set of excited states known as B850* that absorb near 800 nm (770-815 nm), overlapping with the B800 band [61]. EET is driven by electrostatic interactions between pigments. The BChla of the B800 band of LH2 in *R. sphaeorides* are weakly coupled (J = $\sim$1-20 cm^{-1}), whereas the coupling of the BChla in the B850 band are quite strongly coupled (J = $\sim$300^{-1}) [16, 29]. Additionally, the bands are weakly coupled to each other (J = $\sim$20-50 cm^{-1}) [29]. Using Förster theory, energy transfer is inversely proportional to the sixth power of the distance between donor and acceptor. For coherent energy transfer, the distance between donor and acceptor equally affects the energy transfer but the intrapigment coupling must also be considered. Therefore these subtle changes in pigment distances, pigment tilt, and pigment coupling between species would predict differences in energy transfer rates. In practice, because the B800 pigments are somewhat coupled as well as the interband pigments between B800 and B850, modified Förster and Redfield theory best describes energy transfer within LH2 and LH3 [44, 62–64].

Ensemble transient absorption (TA) spectroscopy is used in this work to study energy transfer kinetics. TA monitors the dynamics of an excited state, which can then be fit with a sum of exponentials to extract EET rates. Each exponential component has a timescale (τ) and a relative percent amplitude (A). For each component a physical process must be assigned, such as a specific energy transfer step. This can be determined theoretically, experimentally using control experiments, and through molecular intuition. In some cases assignments are limited to the likely physical process, as it is difficult to prove definitively that the assignment is correct. The percent amplitudes report on whether a process is non-negligible. If the amplitude is very small it may be an insignificant process or even an artifact of the fitting altogether. If it is very large that may indicate that process dominates the kinetics or the technique was not sensitive enough to discern some processes. Additionally, the sign (-/+) of the amplitude reports on which processes are dominating at that specific energy transition. TA kinetic curves are composed of ground state bleach (-), stimulated emission (-), and excited state absorption (+). The net sign of the curve (-/+) provides some information about which of these processes dominate and when energy transfer is occurring. TA is ideally suited because EET occurs on a femtosecond to picosecond timescale. In pump-probe TA, the pump excites the sample while the probe measures the signal. LH2 is excited and the decay of the difference spectrum (probe with pump – probe without pump) reports on the timescale for this EET process. In a one color experiment, the pump and probe are the same wavelength. In one variation of this experiment, the polarization of the pump and probe was set orthogonal and, from monitoring anisotropy decay of the transition dipole moments, EET rates within degenerate states around the ring are extracted. In a two-color experiment, the wavelength of the pump and probe vary. Pump and probe wavelengths and bandwidths can be selectively chosen. Because of the competitive pathways of energy transfer in B800, experimentally determined B800 to B850 rates vary according to the pump wavelength, getting faster as the pump wavelength shifts from 790 to 830 nm causing conflicting information in literature [53]. To mitigate ambiguity, in this work, a comparative analysis between species was done under the same experimental conditions with a narrow (10 nm) pump bandwidth. In contrast, due to the spectral overlap of the B800 and B850 band, experiment has found that LH3 is insensitive to choice in pump wavelength [42]. One color and two color pump-probe TA was used to investigate energy transfer dynamics within several light-harvesting proteins. Due to experimental flexibility, this technique is ideally suited to answer fundamental questions about changes in EET dynamics in light-harvesting systems.

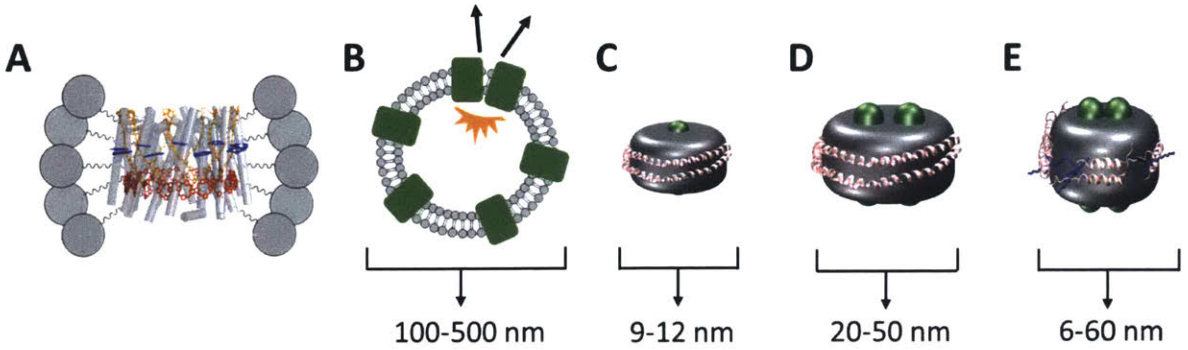

Figure 6: Membrane-model systems. Membrane proteins (green) are solubilized with various membrane mimicking tools. Membrane discs are surrounded by a belting protein (pink). Lipids are shown in gray. (A) LH2 in a detergent micelle. (B) Membrane proteins in a liposome or chromatophore. (C) Single membrane protein in a Nanodisc. (D) Two membrane proteins in ApoE422K or covalently circularized disc. (E) Telodendrimer Nano-Lipoparticles. Telodendrimers are shown in blue.

1 Chapter 1: Model Membrane-Discs

1.1 Membrane Protein Studies

Previous works have employed three predominant methodologies to solve the problems of photosynthetic membrane protein production and purification as well as appropriate sample preparation. The first relies on detergent micelle formation surrounding the hydrophobic portion of the protein to produce a soluble protein-detergent complex (Figure 6A) [65,66]. Although effective in solubilizing membrane proteins, the harsh conditions of detergents can produce drastic changes to protein structure, including loss or change of function as well as denaturation [67–69]. The second method reconstitutes membrane proteins into lipid vesicles *in vitro* (Figure 6B) [47,70–72]. Although this provides a hospitable membrane environment, these systems are heterogeneous in size, have varied and uncontrolled local membrane curvature, and are highly scattering, which can overwhelm spectroscopic signals. Furthermore, membrane vesicles often incorporate multiple proteins, which have been shown to introduce effects from protein-protein interactions that alter the dynamics in photosynthetic light-harvesting complexes [73]. The third method uses LH2-only chromatophores, membrane sections, or live cells [34,68,72,74–78]. Similar to vesicles, this provides a hospitable membrane environment but also includes effects from protein-protein interactions. Furthermore, the membrane morphology and composition can be heterogeneous or even unknown [79]. Thus, the intrinsic energy transfer dynamics of light-harvesting complexes in the membrane environment, without the effects of protein-protein interactions, have not been determined before this work. These effects illustrate that benchmarking the dynamics of individual light-harvesting complexes in the membrane environment requires a near-native system with isolated proteins.

1.2 Nanodiscs

One emerging platform developed by the Sligar lab at the University of Illinois Urbana-Champaign, membrane-discs commonly known as Nanodiscs, overcomes the limitations of the sample preparation methods commonly employed by the spectroscopic community (Figure 6C). Nanodiscs provide a simplified near-native environment to solubilize individual membrane proteins [80–84]. They are similar in structure to nascent discoidal high-density lipoprotein particles in humans that transport lipids, cholesterol, and fats through the circulatory system [85]. Nanodiscs are biochemically produced from subcomponents that are comprised of an amphiphilic belting protein, termed membrane scaffolding protein (MSP), a mixture of lipids used to form a bilayer, and the target membrane protein of interest [82, 86, 87]. The MSPs are derivatives of the human protein ApoA1 which assembles the high-density lipoprotein particles *in situ*. The resultant Nanodiscs exhibit remarkably homogeneous diameters that can be straightforwardly characterized [86]. These Nanodiscs range in outer diameter from 9.8 to 17 nm (Table 1). The size of the Nanodisc can be tuned by the length of the MSP [81]. The type of lipids used to form the Nanodiscs can be selected for length and head group composition to best mimic the native environment. When mixed in precise stoichiometric ratios, these components self-assemble such that the MSP surrounds a lipid bilayer with the target membrane protein embedded (Figure 7) [87]. Key features in the self-assembly process have been identified previously [88]. The two main factors affecting size and shape of Nanodiscs are the choice of solubilizing detergent and the addition of detergent-absorbing resin beads, which removes the detergent from solution to allow the Nanodiscs to form without resolubilization. Because the size of Nanodiscs are still small relative to the wavelengths of UV through near-IR light, they produce very little scattering, making the membrane proteins embedded within this platform amenable to spectroscopic studies [89]. The number of proteins embedded can be controlled by the ratio of target protein to belting protein and the choice of MSP, which determines Nanodisc size. Finally, the lipid bilayer produced within the Nanodiscs forms a natively flat landscape versus an irregularly curved environment as in the membrane vesicles [84].

Although little is known about how well the Nanodisc mimics the native membrane, the flat landscape and bilayer nature suggests they mimic more sufficiently than vesicles or detergent. There are some disadvantages in using Nanodiscs. The first is that it is unknown if the belting proteins interact with the target protein inserted within the membrane-disc. While structural studies have not suggested this occurs in systems studied thus far, it is possible to occur in other systems. The second difficulty is incorporating multiple proteins in the correct orientation. This requires some additional chemical biology to ensure correct protein orientation and stoichiometry within the membrane-discs. Additionally, because the Nanodiscs are formed by a self-assembly process, it can prove difficult to assemble a homogeneous sample with the same stoiciometry of proteins embedded. For example, some discs may contain one protein while others contain two or even none. Lastly, if one would wish to study the reactivity of both hydrophillic ends of the protein which require different concentrations of reagents or different reagents all together, the Nanodiscs do not provide the ability for this type of investigation because both the hydrophillic portions are exposed to the exact same solution. These types of experiments can be done in vesicles, entrapping a different solution on the inside of the vesicle versus outside the vesicle.

Using a small Nanodisc size and substoichiometric ratios of target protein to belting protein allows a single protein to be incorporated into the membrane-discs. The control over membrane-disc composition allows the energy transfer dynamics of individual proteins to be explored without the complexity of protein-protein interactions [82, 90, 91]. The work in the Sligar lab was the beginning of discoidal model membrane-discs. Since their establishment, a wide variety of different types of membrane-discs have emerged.

1.3 Other Discoidal Model-Membrane Platforms

ApoE422K

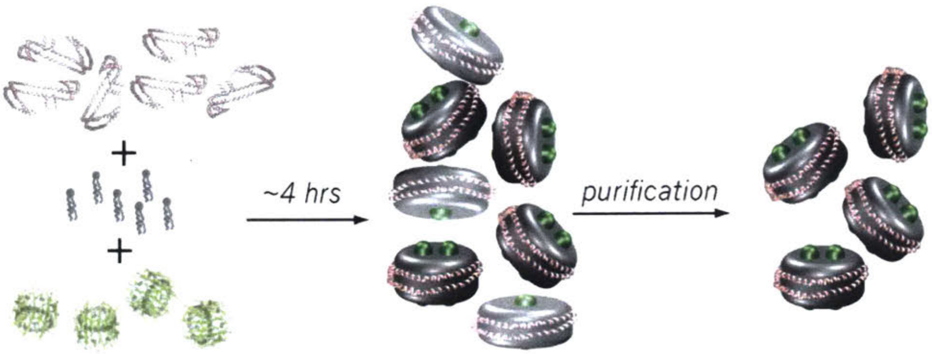

Figure 7: Assembly of model membrane-discs. Specific ratios of target protein (green), lipids (gray), and belting proteins (pink) are mixed together. Upon detergent removal, membrane-discs are spontaneously formed.

A similar protein to ApoA1 named ApoE422K (N-terminal 22 kDa fragment of ApoE4) forms discs of varying size determined by the ratios of belting protein and lipid mixed together in a similar fashion as Nanodiscs (Figure 6D, Table 1) [92,93]. Although ApoE422K is shorter than the largest MSP belting protein MSP1E3D1 for Nanodics, the purified ApoE422K protein was shown to elute in a single peak in size-exclusion chromatography at an elution volume indicative of a hexameric form (data not shown). MSP1E3D1 elutes as monomers, dimers, and trimers in three peaks (data not shown). This suggests that the initial oligomerization of the belting protein, in addition to its length, contributes to the size of membrane-disc formed. Because ApoE422K can form larger membrane-discs and is assembled by the self assembly process the size distribution of final particles can be quite large. Additionally, other larger aggregates form more readily during the assembly process. This makes ApoE422K membrane-discs much more sensitive to assembly stoichiometries of belting protein, lipids, and target protein.

	Model Membrane-Discs
	Size (nm)
Nanodiscs	~10-17
SMALPS	~5-15
Covalently Circularized	~9-50
ApoE422K	~15-35
TD-NLPs	~6-60

Table 1: Model membrane-discs toolkit and their various sizes.

Telodendrimer Nanolipoparticles

In addition to using only belting proteins to form membrane-discs, other types of model membrane systems have been developed. The first type of model-membrane discs are known as telodendrimer nanolipoparticles (TD-NLPs) established by the Coleman lab at University of California Davis School of Medicine (Figure 6E). These membrane-discs utilize a telodendrimer (TD) polymer in addition to the belting protein that improves stability of the discs by allowing the polymer to interweave with the belting protein, increasing the size of the membrane-discs [94]. The TD polymer consists of polyethylene glycol (PEG) with cholic acid (CA) moieties. Changing the composition of the telodendrimer allows for adjustment of disc size (6-60 nm). Δ49ApoA1 (1-49 fragment of Apo A1) and ApoE422K belting proteins produce 16-25 nm discs by including a telodendrimer polymer [94]. Due to the larger sizes, these membrane-discs are ideally suited for experiments measuring energy transfer between multiple proteins. However, the larger sizes have a greater size distribution of final particles. The main concern with such a large size distribution is the possibility of a heterogeneous sample with variable numbers of target protein embedded. The increased sample stability is very beneficial in experiments that take longer periods of time. The TD polymer does add the ability to ligate various ligands onto the polymer allowing for many types of additional experiments. Dyes can be added for FRET experiments. Specific tags can be added to attach the membrane-discs to a variety of different surfaces. Soluble proteins or additional ligands can be attached via a linker to investigate how two proteins function together or how a protein interacts with its ligand. However, caution must be used to determine whether the TD polymer and any additional substituents will interact with your target protein during the assembly process. It is possible that either of these could interfere with the assembly process or cause damage to your target protein.

Styrene Maleic Acid Lipid Particles

Another type of model-membrane disc uses a styrene maleic acid co-polymer (SMA) as a belting tool to form discoidal membrane particles [95–97]. The advantage to these particles is that the polymer can be used to directly remove membrane proteins from the native membrane without the use of detergent. This prohibits any interaction of the protein with detergent which can cause alterations to the protein structure and loss of function. Additionally, it provides the membrane-disc with the most native lipid composition. However, because the SMA essentially extracts a section of the native membrane, the composition of the membrane-discs can be completely unknown. While incorporating protein-tags onto the *in vivo* protein of interest can allow one to select the membrane-discs with their target protein embedded, it is still unknown how many of the target proteins are present and if any additional proteins are present. Because protein-protein interactions can affect biological processes this may make any results difficult to determine definitively. Finally, these are limited to only smaller sized membrane-discs (Table 1).

Covalently Circularized Membrane-Discs

Finally, the Wagner group at Harvard has created a covalently circularized membrane-disc [98]. Using a sortase reaction, newly made variants of ApoA1 were covalently linked at the C and N termini. Varying lengths of ApoA1 variants led to membrane-discs of sizes varying from 9-50 nm (Table 1). These were shown to have increased stability as well as a more homogeneous size distribution. However, the larger membrane-discs have much less stability overall in comparison to Nanodiscs. In practice, forming the larger particles is very sensitive to reagents, stoichiometries, and the incubation with the detergent-absorptive beads. Additionally, the covalently linked belting proteins do not produce only the size of membrane-disc expected. They produce smaller sized membrane-discs in the same reaction as well. It is unclear how the covalently linked belts made for a precise size are generating membrane-discs of a variety of sizes. Perhaps the covalently linked protein wraps around the disc twice, but this would yield membrane-discs much smaller than what is actually observed. More likely, the covalently circularized belt may assemble in a fashion that it does not actually encircle the target protein but forms the membrane-disc by interacting in a similar way to Nanodiscs, in a side on side fashion.

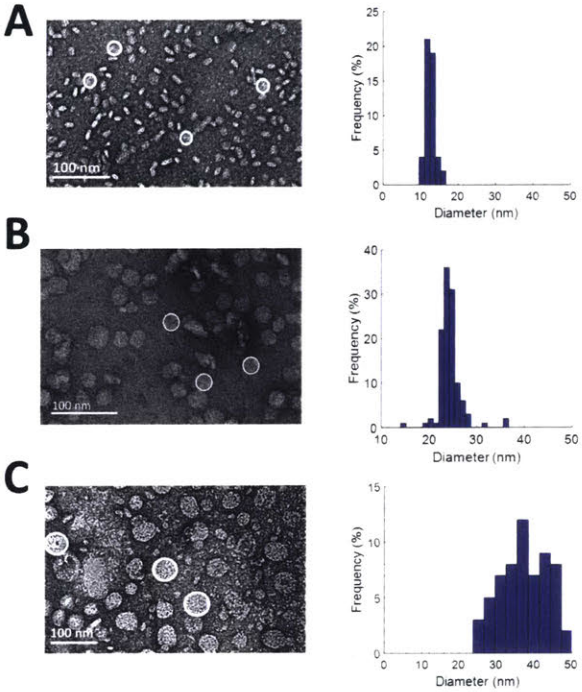

Figure 8: Optimal ratios of belting protein and lipids were determined to produce a platform of empty model-membrane discs. (A) 12 nm membrane-discs produced with MSP1E3D1. (B) 25 nm membrane-discs produced with NW50. (C) 30-45 nm Discs produced with ApoE422K.

1.4 Conclusion

Belting proteins MSP1E3D1, ApoE422K, and covalently circularized belting protein NW50 were used with DMPC and POPC to establish a platform of membrane-discs for various studies (Figure 8). MSP1E3D1 produces 12 nm membrane-discs as expected (Figure 8A). NW50 produced 25 nm membrane-discs (Figure 8B). ApoE422K was shown to produce 30-50 nm membrane-discs by adjusting the ratio of protein to lipids (Figure 8C). Figure 8 illustrates the variety of different sizes available for future studies. In this work, using ApoE422k and a Nanodisc belting protein MSP1E3D1, membrane-discs are utilized to achieve both a spectroscopically viable sample and a simplified near-native membrane. With the combination of model-membrane discs and spectroscopy the effect that specific lipid-protein and protein-protein interactions have on the energy transfer dynamics within photosynthetic light-harvesting proteins was investigated.

2 Chapter 2: Impact of the Lipid Bilayer on Energy Transfer Kinetics in the Photosynthetic Protein LH2

2.1 Summary

The energy transfer dynamics of LH2 are highly sensitive to intermolecular distances and relative organizations. As a result, minor structural perturbations can cause significant changes in these dynamics. Previous experiments have primarily been performed in two ways. One uses non-native samples where LH2 is solubilized in detergent, which can alter protein structure. The other uses complex membranes that contain multiple proteins within a large lipid area, which make it difficult to identify and distinguish perturbations caused by protein-protein interactions and lipid-protein interactions. Here, we introduce the use of the biochemical platform of model membrane-discs to study the energy transfer dynamics of photosynthetic light-harvesting complexes in a near-native environment. We incorporate a single LH2 (nonamer of heterodimers) from *R. sphaeroides* into membrane discs that provide a spectroscopically amenable sample in an environment more physiological than detergent but less complex than traditional membranes. This provides a simplified system to understand an individual protein and how the lipid-protein interaction affects energy transfer dynamics. We compare the energy transfer rates of detergent-solubilized LH2 with those of LH2 in membrane-discs using transient absorption spectroscopy and transient absorption anisotropy (Figure 9A). For one key energy transfer step in LH2, we observe a 30% enhancement of the rate for LH2 in membrane-discs compared to that in detergent. Based on experimental results and theoretical modeling, we attribute this difference to tilting of the peripheral bacteriochlorophyll in the B800 band. These results highlight the importance of well-defined systems with near-native membrane conditions for physiologically-relevant measurements. This work has been published in Chemical Science [46].

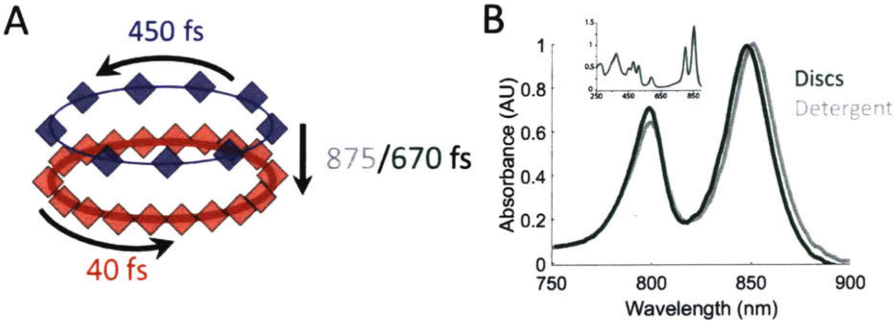

Figure 9: Summary of results. (A) Time constants for energy transfer as measured by transient absorption spectroscopy on both the detergent solubilized LH2 and the membrane disc embedded LH2. Energy transfer within the B800 and B850 bands is similar for both samples (blue and red, respectively) but energy transfer between bands indicates structural differences induced by the membrane condition (detergent – gray; membrane discs – green). (B) UV-VIS linear absorption spectra for LH2 in LDAO detergent (gray) and solubilized in DMPC membrane discs (green) in the B800/B850 region. The data are normalized to the B800 peak on the wavelength scale and shows a peak shift of the B850 band from 849 nm to 852 nm for LH2 in detergent and discs, respectively. Insert: the full spectrum of LH2 in detergent and discs from 250 to 900 nm showing the nearly identical structure of the two LH2 samples, independent of solubilization condition.

2.2 Results and Discussion

2.2.1 LH2 in Membrane Discs

A single LH2 from *R. sphaeroides* (nonomer of heterodimers) was embedded into a membrane-disc as described in Chapter 1. The linear absorption spectra (Figure 9B) show that the LH2 complexes maintain integrity within the membrane-disc. The same peaks are observed in detergent-solubilized and disc-embedded LH2, demonstrating that the structure of the protein is robust to the disc assembly process. However, the linear absorption spectra of LH2 in detergent and in discs shows a consistent shift of the B850 absorption peak from 849 nm in detergent to 852 nm in membrane-discs, as previously reported [72, 99]. Pressure-dependent spectral shifts have also been previously reported [100]. The electronic structure of the pigments is highly sensitive to the protein environment so structural perturbations can alter the absorption spectra. The 3 nm shift highlights that the local environment of the B850 pigments changes due to solubilization environment. The complex and varied interactions of membrane proteins with detergents are both protein and detergent specific. As a result, it is difficult to identify the molecular origin of spectral shifts.

2.2.2 Time-Correlated Single Photon Counting Measurements

Time-correlated single-photon counting (TCSPC) was used to determine the fluorescence kinetics of detergent-solubilized and disc-embedded LH2 (Figure 10). All four samples exhibit mono-exponential decays with a time constant of ~1 ns, consistent with previous work (Table 2) [72]. Fluorescence decays of detergent-solubilized and membrane-embedded LH2 have previously been shown to have a mono-exponential decay and bi-exponential decay, respectively, where the bi-exponential decay exhibits shorter time constants [72,79]. The shorter time constants are attributed to protein-protein energy transfer enabling exciton-exciton annihilation, which does not occur in the membrane-discs. The mono-exponential decays observed here, therefore, are consistent with previous work and illustrate the utility of membrane-discs as model systems for energy transfer kinetics of single LH2s in a near-physiological environment.

	TCSPC	
	A1	$\tau 1$
β-OG	1	1.018 ns
LDAO	1	1.113 ns
DMPC	1	1.119 ns
POPC	1	0.974 ns

Table 2: Parameters extracted from fits of the TCSPC data. Each fluorescence decay curve was fit mono-exponentially. The amplitudes and time constants are shown.

2.2.3 Transient Absorption Spectroscopy and Transient Absorption Anisotropy

To probe the effect of solubilization environment on LH2, the energy transfer kinetics were measured in two detergents, LDAO and β-OG, and two lipid compositions of the membrane, DMPC and POPC. Detergents that have been shown to solubilize LH2 while maintaining the integrity of the complex are LDAO, DDM, and β-OG. LDAO and DDM are the most commonly used detergents, while β-OG is more rarely used. However, the detergent tails of LDAO and DDM are the same length, while the tail of β-OG is significantly shorter [74, 102, 103]. Specifically, the hydrocarbon chain of β-OG is six carbons shorter than that of LDAO. β-OG also has a much bulkier head

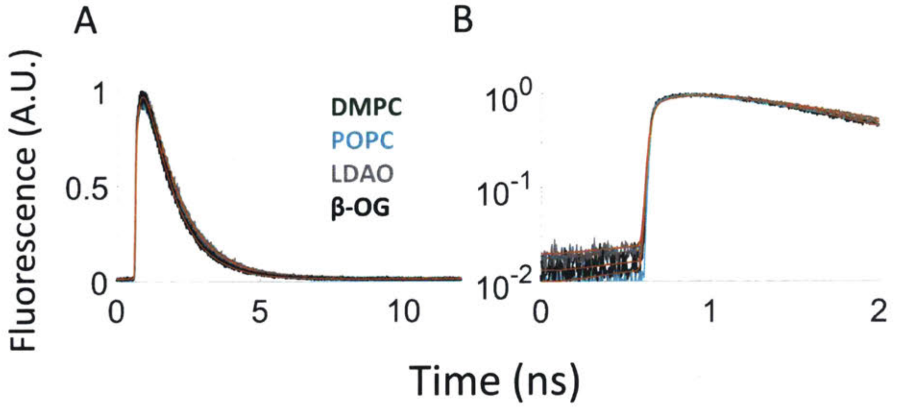

Figure 10: Time-correlated single photon counting (TCSPC) experiments and curve fitting were performed as described previously [101]. For the experiments presented here, the direct output of the Ti:sapphire oscillator (Vitara-S, Coherent, Inc.) was used as the excitation source (λ=800 nm, 80 MHz). The excitation wavelength was selected with a 800 nm center-wavelength bandpass (FF01-7851/62-25, Semrock Inc.). The emission wavelength was selected with a 875 center-wavelength bandpass filter (FF01-834/LR 25-L2, Semrock Inc.). Excitation density for these experiments was 6.22 mW/cm^2. Fluorescence lifetime data for all four samples in (A) full linear scale and (B) logarithmic scale to 2 ns. Data are shown in color and fits are shown as red lines. All samples were fit to a mono-exponential decay.

group than LDAO (Figure 11). Therefore, LDAO and β-OG were selected to provide two distinct detergent tail lengths. The hydrocarbon chain of POPC is two carbons longer than that of DMPC, although both are similar lengths to the majority of native lipids in *R. sphaeroides*.

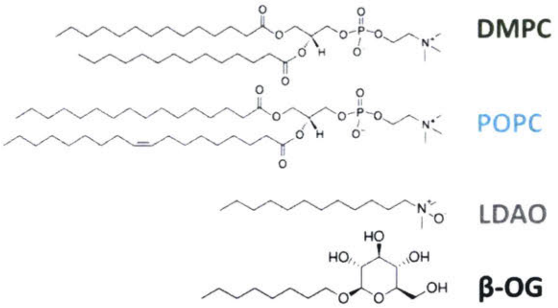

Figure 11: Lipid and detergent structures for the samples used in these experiments.

Figure 12A presents 800 nm pump - 850 nm probe transient absorption spectra recorded with the pulse polarization set to the magic angle (MA = 54.7°) for all four samples. This pulse combination directly probes the time evolution of the population of states at 850 nm (in the B850 ring) after initial excitation of states at 800 nm (in the B800 ring). The spectra are fit to a sum of three exponentials, the results of which are shown in Table 3. The spectrum of LH2 in β-OG collapses to a sum of two exponentials, indicating different energy transfer pathways than the other three samples. For the three component spectra, the fast decay component is assigned to B850* to B850 (as described in the introduction) and decays over the course of the first 0.5 ps, in line with previous experimental and theoretical work [62]. The second decay is assigned to the transfer

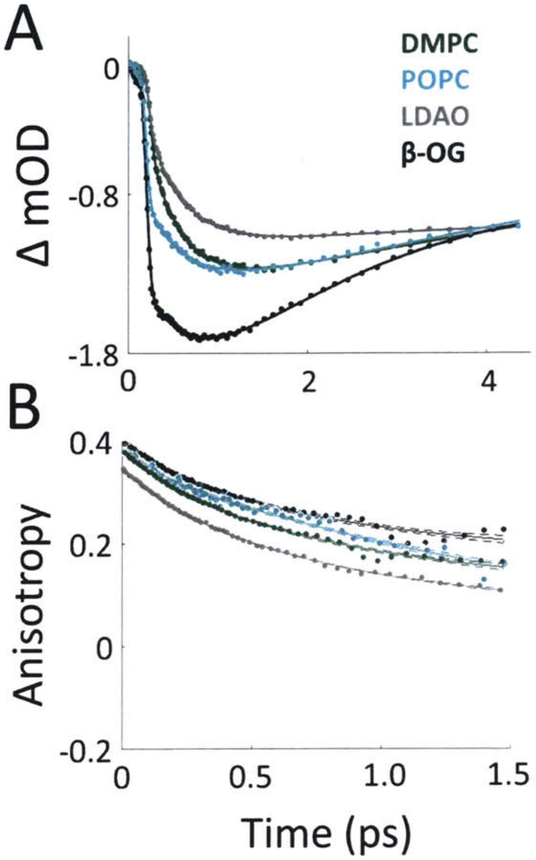

Figure 12: Transient absorption data of LH2 in different solubilization environments. (A) Magic angle 800 nm pump - 850 nm probe transient absorption spectra for LH2 in DMPC membrane discs (green), POPC membrane discs (teal), LDAO detergent (gray), and β-OG detergent (black). (B) 800 nm pump - 800 nm probe anisotropy for the four LH2 solubilization conditions. Data is shown as points and three exponential fits are overlaid as lines with 95% confidence intervals indicated by the shaded region around each line.

of population between the B800 and B850 Q_y excited states (lowest lying energy states), directly reporting on inter-band energy transfer dynamics. According to previous work, transfer from B800 to B850 occurs directly and via B850* with approximately the same timescale [62]. A 30% increase in the timescale of this decay component was observed in membrane-discs, revealing a difference in B800 to B850 energy transfer between detergent-solubilized and membrane-reconstituted LH2 due to one or both of the energy transfer routes. Longer timescale processes, i.e. vibrational relaxation (Stokes' shift) and the decay back to the ground state, are collectively fit by the third time component of picoseconds.

While the rate of energy transfer from B800 to B850 changes with local environment, the dynamics of energy transfer within both the B800 and B850 rings do not. Transient absorption anisotropy measurements decay due to the orientational change of the excitation as it transfers within the band. Thus, the experiment identifies and quantifies energy migration around the ring. The 800 nm anisotropy (Figure 12B) is initially fit to a sum of two exponential decays. The long time

	800 Pump - 850 Probe Magic Angle		800 Pump - 800 Probe Anisotropy	
	τ	Weight	τ	Weight
β-OG	400 fs	24%	425 fs	49%
	5 ps	-76%	>5 ns	51%
LDAO	280 fs	19%	420 fs	58%
	875 fs	36%	>5 ns	42%
	>10 ps	-45%		
DMPC Discs	325 fs	8%	419 fs	58%
	670 fs	32%	>5 ns	42%
	>10 ps	-60%		
POPC Discs	325 fs	16%	413 fs	43%
	670 fs	15%	>5 ns	57%
	9 ps	-69%		

Table 3: Time constants and relative weights for magic angle 800 nm pump - 850 nm probe transient absorption (left column, data shown in Figure 12A) and 800 nm pump - 800 nm probe anisotropy (right column, data shown in Figure 12B) for the four solubilization conditions. Each spectrum was initially fit to a sum of three exponential decays. When two components collapsed to a single decay value, a two exponential fit was performed.

component (>5 ns) is then fixed as an offset to improve the fit for the short time decay to produce the timescales shown in Table 3. For all four LH2 solubilization conditions, these components are similar in time and relative weight. The faster decay component of ~420 fs corresponds to energy transfer within the B800 ring. The 850 nm anisotropy is fit in the same manner as the 800 nm anisotropy with an additional decay component. The results are shown in Figure 13 and Table 4. The data show a rapid decay component corresponding to energy transfer within the B850 ring of ~55 or ~65 fs for LH2 solubilized in LDAO and in DMPC discs, respectively. The energy transfer dynamics within the B850 ring are much faster because the pigments are much strongly coupled [29]. In addition to the <1 ps energy transfer dynamics discussed here, in all data sets there is a long (nanoseconds) component that arises from excited state decay and in the B850 anisotropy there is a picoseconds component that arises from vibrational relaxation.

	850 Pump - 850 Probe	
	τ	Weight
Detergent	65 fs	24%
	1700 fs	53%
	>5 ns	41%
Discs	55 fs	22%
	1340 fs	31%
	> 5 ns	47%

Table 4: Anisotropy decay rates and relative weights. Each anisotropy curve was fit to a sum of three exponential decays and the time constants and relative weights of each component are shown in the table.

The energy transfer rates are similar not only in DMPC and POPC membrane-discs, as observed here, but are also consistent with previously published experiments for LH2 in LH1-knockout *R. sphaeroides* [30]. Collectively, these results suggest that protein-protein interactions

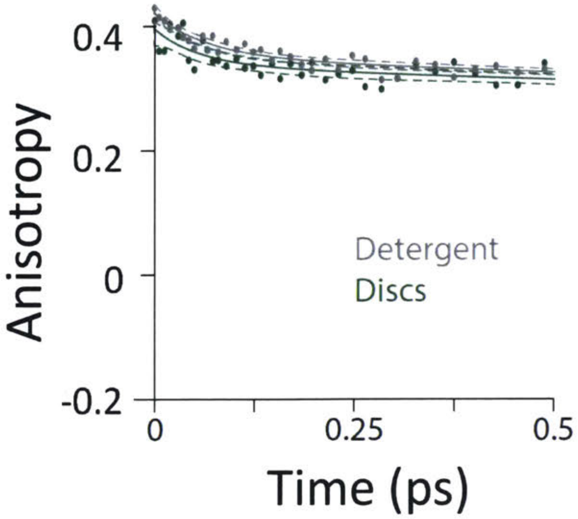

Figure 13: Anisotropy for LH2 in LDAO detergent (grey) and in DMPC discs (green) calculated from simultaneously measured parallel and perpendicular components (V-V and V-H, respectively) for 850 nm pump, 850 nm probe.

are not impacting the photophysics, in contrast to green plants [73]. Furthermore, the similarity in energy transfer rates illustrates that a membrane maintains a similar local environment for LH2 regardless of lipid composition. This similar local environment is likely due to the structured assembly of a membrane where the acyl chains predominantly interact with the protein in a side-by-side orientation, thus decreasing lipid-pigment interactions. The additional two carbon chain length of the POPC versus DMPC (Figure 11) does not have a significant effect on energy transfer between the B800 and B850 bands. This result excludes the possibility that the membrane height is the driving factor behind the increase in the rate of energy transfer in the membrane-disc samples. Interestingly, although DMPC discs are in a structured gel phase while POPC discs are in a liquid crystalline phase at the temperature of our experiments (4°C), there is no change to the energy transfer rates. This lack of change suggests that membrane phase has little effect on the energy transfer rates, and thus on the protein structure. Furthermore, these results highlight that energy transfer dynamics are robust to the dynamic lipid composition of the purple bacterial membrane.

To determine the molecular origin of the effect of solubilization environment, the energy transfer rates within the B800 band and from B800 to the B850 band were calculated using generalized Förster theory as a function of tilt of the BChla in the B800 band (See Appendix 2," Calculation of Relative Energy Transfer Rates") [105]. Because the BChla in the B800 band protrude from the protein scaffold (Figure 2A) and interact with the lipid or detergent used for solubilization, they are much more susceptible to perturbation due to solubilization environment than the BChla in the B850 band. Figure 14 shows the calculated relative energy transfer rates within the B800 band and between the B800 and B850 band as a function of the tilt of the BChlas in the B800 band. These calculations determine relative rates, and so take into account all the experimental energy transfer steps, including those via the B850* states. The rate of energy transfer from B800 to B850 is much more sensitive (purple) than the rate within the B800 ring (blue). Flattening the B800 Bchlas by 2° causes an enhancement of the B800-B850 rate by more than 30%, while the B800 rate remains almost constant with less than 1% enhancement. The sharp dependence of the B800-B850 relative rate on the tilt angle arises from sensitivity to the distance between the coupled dipoles,

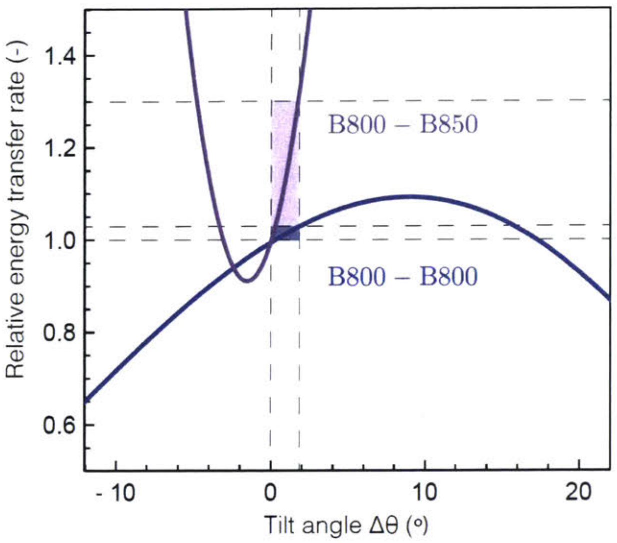

Figure 14: Theoretical energy transfer rates within LH2. The energy transfer rates within B800 (blue) and between B800 and B850 (purple) as a function of a tilt in the orientation of the B800 transition dipole moments relative to the original structure [104]. A positive tilt results in a steady increase of the B800 rate from the original geometry, up to a maximum obtained for a tilt of $\Delta\theta = 9^\circ$ corresponding to a flat B800 ring. The shaded domains illustrate the range for which the B800 rate increases by 1% (blue) and the corresponding, drastic change in the inter-ring transfer rate (purple). Flattening the B800 BChls by 2° enhances the B800-B850 rate by more than 30%. The presented B800-B850 rate displays the average rate from one B800 BChl to the six nearest B850 BChls.

and hence on how the tilt is simulated. It can become smoother by including disorder [106]. These theoretical predictions are consistent with our experimental results, which find a change in B800 to B850 energy transfer but similar energy transfer rates within the B800 band in the anisotropy measurements at 800 nm as a function of solubilization (Table 3). This model would also predict similar energy transfer rates within the B850 band as a function of solubilization environment as observed in the short time component of the anisotropy measurements at 850 nm (Table 4). Essentially, the B800 BChla tilt towards the orientation of the B850 BChla, which increases the inter-band coupling, speeding up the overall B800 to B850 energy transfer step including contributions from both B800 to B850 and B800 to B850*. Because the B800 BChla tilt symmetrically together, their orientation relative to each other is largely unchanged, which leaves the intra-band coupling the same.

While the microscopic origin of the perturbation cannot be definitively determined, three possibilities are hydrophobic mismatch, lateral membrane pressure, or direct interaction of solubilizing environment with pigments. We consider these three physical processes. Hydrophobic mismatch occurs when the height of the membrane or detergent used does not match the hydrophobic region of the protein. *In vivo*, the hydrophilic headgroups of the bilayer interact with the hydrophilic protein regions, which are the N- and C- terminal regions of the β subunit in the case of LH2. The hydrophobic acyl chain region of the bilayer associates with the hydrophobic protein regions, which are the center of transmembrane alpha helices. The *in vivo* membrane height surrounding LH2 in *R. sphaeroides* is measured to be between 40 and 45 Å [107]. To properly emulate the native environment, the solubilizing membrane or detergent should span a similar distance and have the hydrophilic and hydrophobic regions properly matched to the corresponding regions of the membrane protein [74, 108]. Hydrated DMPC and POPC (Figure 11) bilayers measure ~44 Å in thickness, have a phosphatidylcholine headgroup, and a two acyl chain tail, which produce an environment that matches the native conditions [109]. LDAO is an intermediate detergent with a weakly polar headgroup and a tail with 12 carbons [110]. Although advantageous for solubilization, purification, and crystallization, LDAO produces micelles with a single acyl chain length of ~15-16 Å [111, 112]. This reduced lipid height means that LDAO is shorter than the hydrophobic region of native LH2, producing a hydrophobic mismatch of ~7 Å as measured from the crystal structure [104, 110]. Hydrophobic mismatch has been shown to alter membrane protein function, and thus is a likely candidate to change the tilt of the Bchla in the B800 band [113, 114]. Hydrophobic mismatch would also explain the greater perturbation of β-OG due to its even shorter hydrocarbon tail and bulkier head group.

The lateral membrane pressure profile is a second possible cause of the changing tilt of the B800 band BChlas. A blue shift of the B850 band has been previously observed with increasing pressure [100]. Here, we observe the same shift in moving from membrane solubilized to detergent solubilized LH2, as shown in Figure 9B. In addition, only a very small shift is observed in the B800 band in either the membrane solubilized LH2 or the pressure-dependent absorption spectra. These similarities suggest that pressure may be the physical origin of the differences observed here. Furthermore, LH2 can induce curvature to the membrane that changes the lateral membrane pressure profile, as seen in previous work [115]. Although difficult to measure *in situ*, the lateral pressure profile for membrane bilayers has been extensively studied using computational methods, which have included the effects on integral membrane proteins [116–119]. In a lipid bilayer, such as the native environment or the membrane-discs used in this work, the lateral stress profile has a positive (inward toward the membrane protein) pressure at the furthest extent due to the electrostatic interactions of the headgroups, a negative pressure due to the interfacial tension at the polar-apolar interface, and a positive pressure in the acyl chain region due to the repulsion between the hydrocarbon chains [120]. In a protein-detergent system, it has been suggested that single chain, small headgroup detergents increase the pressure in the headgroup region while decreasing the pressure in the acyl chain relative to the bilayer system [121]. The LDAO headgroup (Figure 11) is an amine oxide zwiterionic group which is small (2.8 nm^2) compared to the phosphatidylcholine headgroup of the DMPC (5.7 nm^2) and POPC (6.9 nm^2) [87]. The β-OG headgroup is a glucoside that is nonionic, polar, and similar in size (~5.1 nm^2) compared to DMPC or POPC but is much bulkier due to its ring structure. In combination, LDAO's small headgroup, β-OG's bulkier headgroup, and the single acyl chain of detergents produce a very different intra-membrane region and thus a very different lateral membrane pressure profile than the DMPC or POPC discs [122]. Finally, direct intermolecular interactions of single chain detergent molecules with pigments rather than the protein scaffold is a third possible cause of the changing tilt of the B800 band BChlas. Similar effects have previously been reported in other photosynthetic systems (LHCII from *Pisum sativum*, peas) and perturbations in protein-pigment interactions due to detergent have been shown to alter the excited state lifetimes of LH2 [123, 124].

Our data reveals a change in energy transfer kinetics which suggests that varying the solubilization environment alters the structure of LH2 in such a way as to increase the B800-B850 energy transfer rate. The energy transfer rates within individual proteins also determine the pathways of energy transfer between proteins to reach the reaction center. Energy transfer from one LH2 to another via the B850 rings is thought to occur on a 1-5 ps timescale [16]. Currently, inter-protein energy transfer kinetics have been done in model systems that have multiple proteins incorporated and have multiple other processes occurring that may influence those kinetics. Because the B800 ring protrudes from the protein, energy transfer from one LH2 to another via the B800 rings may occur even faster than via the B850 rings. If the B800 to B850 energy transfer time were 875 fs, energy transfer from one LH2 to another via the B800 rings would be likely. However, we have determined the energy transfer time from B800 to B850 to be 670 fs in a near-native membrane environment, which means most energy transfer from one LH2 to another occurs via the B850 rings. While the timescales observed here suggest B850 to B850 transfer, further experiments are required to definitively determine the pathway of energy flow to the reaction center. The use of model membranes, as introduced here for studies of energy transfer in photosynthetic light-harvesting, could be expanded to look at protein-to-protein energy transfer processes, such as LH2 to LH1.

2.3 Conclusion

Here, we have introduced the use of membrane-discs as a tool to study the energy transfer dynamics of photosynthetic light-harvesting complexes in a near-native environment and demonstrated the utility of this approach for LH2. In contrast to traditional sample preparation methods, membrane-discs allow the dynamics of individual proteins to be explored free from both non-physiological effects in detergent solubilization and the complications of protein-protein interactions. In LH2, one important energy transfer step, from the B800 to the B850 band, was found to be 30% faster in the membrane environment than in detergent, the typical experimental environment. Our experimental and theoretical results suggest that this change in dynamics is caused by an environment-induced tilt of the BChla in the B800 band. Future structural studies may provide experimental evidence for tilting of the B800 BChlas. While X-ray crystallography relies on detergent-solubilized protein, nuclear magnetic resonance or circular dichroism could confirm the tilt of the B800 BChla as the structural change upon membrane incorporation, similar to approaches used to observe other structural changes [90, 125–128].

Overall, our results highlight that detergent solubilization introduces non-physiological effects on dynamics in membrane proteins. The impact of detergent solubilization observed here suggests that detergent solubilization may similarly perturb the behavior of other membrane proteins, such as enzymes, photoreceptors, and ion channels. Furthermore, these results open the possibility to manipulate the membrane environment to produce systems with desired activity or functionality. Additionally, these experiments accentuate the need to study photosynthetic light-harvesting systems, and, more generally, membrane proteins, in near-native environments.

2.4 Materials and Methods

2.4.1 Purification of MSP1E3D1

Over-expression of disc belting protein MSP1E3D1 was adapted from previously reported protocols [86, 87]. The plasmid for the belting protein MSP1E3D1 was acquired from Addgene (plasmid #20066) containing a 6X histidine tag and kanamyacin antibiotic resistance. MSP1E3D1 was transformed into One Shot BL21 Star (DE3) Chemically Competent *E. coli* (ThermoFisher Scientific #C601003) and glycerol stocks were made by flash freezing in liquid nitrogen and storing at -80°C. Over-expression was carried out on a shaker at 37°C. A 10-mL starter culture of Luria Bertani Broth was inoculated with the glycerol stock and grown overnight. The starter culture was used to inoculate 1-L of terrific broth. Protein over-expression was induced between 0.6-0.8 OD (at 600 nm) with a final concentration of 1 mM isopropyl β-D-1-thiogalactopyranoside. Cells were allowed to produce protein for five hours. The cell pellet was collected by centrifuging at 3k rpm at 4°C for 20 minutes. The supernatant was discarded and the cell pellet was resuspended in 25 mL of 20 mM Tris, 150 mM NaCl, pH 7.4. Phenylmethylsulfonyl fluoride was added to a final concentration of 1 mM. Triton X-100 was added to 0.1% v/v. DNase I (New England Biolabs) was added (300 units) with a final concentration of 2.5 mM for magnesium chloride and 0.5 mM calcium chloride. Solution was homogenized in a tissue homogenizer. Solution was probe sonicated on ice for 3 minutes at 30% power for 30 seconds on and 30 seconds off. Solution was centrifuged at 4k rpm at 4°C for one hour to remove cellular debris. The supernatant lysate was loaded onto a 25-mL Ni-NTA chromatography column and allowed to equilibrate with the beads on a nutating mixer at 4°C overnight. Protein purification was carried out by previously established protocols [86, 87]. Protein mass was verified by reverse-phase liquid-chromatography mass-spectrometry (LC-MS). Purity was determined by denaturing gel electrophoresis (SDS-PAGE). To ensure there was no nucleic acid contamination, the 260/280 nm ratio was inspected by UV-VIS. Protein was concentrated to $\sim$500 μM and aliquoted into 50 μL aliquots, flash frozen in liquid nitrogen, and stored at -80°C for later experiments.

2.4.2 Lipid Preparation

1,2-dimyristoyl-sn-glycero-3-phosphocholine (DMPC) and 1-palmitoyl-2-oleoyl-sn-glycero-3-phosphocholine (POPC) were purchased from Avanti Polar lipids (#850345C and #850457, respectively). Chloroform was evaporated under a gentle stream of argon gas and dessicated overnight under vacuum. Lipid was resuspended in 20 mM Tris, 150 mM NaCl, 200 mM sodium cholate, pH 7.4 and sonified in a Branson Ultrasonic Bath until solution was clear. The concentration of lipid was determined by a phosphorus assay as previously reported [129]. Lipids were degassed of oxygen to prevent oxidation by bubbling in nitrogen, aliquoting, freezing in liquid nitrogen, and then storing at -80°C for later experiments.

2.4.3 LH2 Preparation

Production and purification of LH2 were performed similarly to the methodology used by Cogdell *et. al.* [130]. Wild type *R. sphaeroides* ATCC2.4.1 was provided by the Blankenship lab and single colonies were used to inoculate 1.6 L of growth media (1% w/w tryptone, 0.5% w/w yeast extract, 4 mM NaCl, 0.5 mM $CaCl_2$, and 0.8 mM $MgSO_4$). The culture was grown anaerobically for 3 days at approximately 30 °C with constant illumination from a 100 W incandescent light bulb. Cells were pelleted at 4k rpm at 4 °C and the supernatant was discarded. The pellet was resuspended in sonication buffer (20 mM Tris, 100 mM NaCl, 1 mM $MgSO_4$, pH 7.5), and the cells were lysed using ten 1 minute on – 1 minute off probe sonication cycles with the sample in an ice bath. The lysate was centrifuged for 8 hours at 28k rpm and the pellet resuspended in a minimal volume of solubilization buffer (20 mM Tris, pH 7.5). Linear absorption at 850 nm was used to quantify the concentration of LH2 and the concentration was adjusted with solubilization buffer to approximately 100 OD at 850 nm [131]. Lauryldimethylamine oxide (LDAO, Sigma Aldrich) was added, dropwise, while stirring, up to 1.5% (w/w) and the sample was homogenized on ice using a plunger homogenizer. Once homogenized, the sample was diluted with solubilization buffer to 0.1% LDAO and centrifuged for 4 hours at 28k rpm.

The supernatant, containing the detergent solubilized LH2, was loaded onto an ion exchange chromotography column (HiPrep DEAE FF 16/10, GE HealthSciences) and eluted with 20 mM Tris, 0.1% LDAO, pH 8 with a linear gradient from 0 to 400 mM NaCl over 18 column volumes (360 mL) at 4°C collecting 4 mL fractions. Fractions were combined based on their UV-VIS spectrum specifically separating the LH2 from reaction center and the fractions were concentrated to <5 mL with 30 kDa filters and centrifugation at 4k rpm. The concentrated LH2 was loaded onto a gel filtration column (HiPrep Sephacryl S-200 HR, GE HealthSciences) and eluted with 20 mM Tris, 100 mM NaCl, 0.1% LDAO, pH 8 buffer at 4 °C collecting 1 mL fractions. Fractions were selected based on LH2 content, purity was determined by SDS-PAGE, and LH2 was concentrated to approximately 20 uM. 0.01% sodium azide was added to purified LH2, aliquoted to 100 μL volumes, flash frozen with liquid nitrogen, and stored at -80 °C.

2.4.4 LH2 Disc Assembly

Loaded discs were produced using a construct from the common apolipoprotein ApoA1, MSP1E3D1 [80, 86]. MSP1E3D1, DMPC/POPC, and LH2 from *R. sphaeroides* were mixed together at ratios of 1:131:0.125. These ratios were selected to yield discs that were $1/4$ filled with LH2 to prevent contamination of LH2 not embedded in the disc or multiply embedded proteins. The reaction was allowed to incubate on a rocker for 1 hr at room temperature for DMPC and 4°C for POPC. Bio-Beads SM-2 Resin was added to $2/3$ the volume of the reaction. Bio-Beads were allowed to incubate with the reaction on a rocker for 1 hr at room temperature for DMPC and 4°C for POPC and then overnight at 4°C for both to ensure efficient detergent removal. Bio-Beads were removed through centrifugation. The reaction was purified by the 6×histidine tag of the belting protein on a 1 mL Ni-NTA column to remove any LH2 not incorporated into discs. The reaction was allowed to equilibrate with the beads for 1 hr at 4°C on a nutating mixer. Column flow-through was collected and the column was washed with 1 mL of 40 mM Tris, 300 mM NaCl, 20 mM imidazole, pH 8.0 three times. Discs were eluted with 40 mM Tris, 300 mM NaCl, 400 mM NaCl, pH 8.0. Fractions containing discs, as determined by SDS-PAGE, were dialyzed against 20 mM Tris, 100 mM NaCl, 0.5 mM EDTA, pH 7.4 to remove imidazole. Determined by SDS-PAGE, no excess LH2 was present in the flow-through or washes, indicating 100% incorporation of LH2 into discs.

LH2 discs were further purified by fast protein liquid chromatography (FPLC) with a BioLogic DuoFlow (Bio-Rad) on a Superdex 200 Increase 10/300 GL (GE Healthcare Lifesciences) at a flow rate of 0.75 mL/min with 20 mM Tris, 150 mM NaCl, pH 7.4. Fractions of main peaks were collected and analyzed by SDS-PAGE, linear absorption, and transmission electron microscopy (TEM) to identify the peak containing LH2 discs. The optimal lipid ratio was determined experimentally by maximizing the LH2 disc FPLC peak, which was found from characterization.

TEM samples were prepared on 400-mesh Cu-carbon coated films (Electron Microscopy Sciences) that were negatively glow-discharged. 5 μL of sample with appropriate dilution (1:20 after FPLC) was added to grid for 1 minute. Excess sample was removed with a Kimwipe from the edge to prevent deposition of fibers onto the grid. 5 μL of 2% uranyl acetate in water was added for 30 seconds. Excess stain was removed similarly to the sample. Samples were allowed to air dry for at least 1 hour. Samples were imaged on a FEI Tecnai (G2 Spirit TWIN) at 120 kV. The distribution of disc sizes was analyzed using more than 100 particles by ImageJ software (https://imagej.nih.gov).

2.4.5 Time-Correlated Single Photon Counting Measurements

Time-correlated single photon counting (TCSPC) experiments and curve fitting were performed as described previously [101]. For the experiments presented here, the direct output of the Ti:sapphire oscillator (Vitara-S, Coherent, Inc.) was used as the excitation source ($\lambda = 800\ nm$, $80\ MHz$). The excitation wavelength was selected with a 800 nm center-wavelength bandpass (FF01-7851/62-25, Semrock Inc.). The emission wavelength was selected with a 875 center-wavelength bandpass filter (FF01-834/LR 25-L2, Semrock Inc.). Excitation density for these experiments was 6.22 mW/cm^2.

2.4.6 Sample Preparation for Ultrafast Spectroscopy

After purification, the LH2 discs were diluted to a final volume concentration of ~500 nM corresponding to a visible absorption of ~1.5 OD at 850 nm in 20 mM Tris, 150 mM NaCl, pH 7.4. For detergent solubilized samples, LH2 in LDAO was taken from stocks and diluted to a similar concentration in 20 mM Tris, 150 mM NaCl, pH 7.4, 0.1% LDAO. LH2 in LDAO was buffer exchanged by centrifugation into 0.75% β-OG over the course of 12 hours with an exchange every 20 minutes. The linear absorption was measured for both the flow through and the sample during buffer exchange to ensure there was no loss of the Bchls in the B800 band by monitoring for the appearance of a Bchl peak at 775 nm. A peristaltic pump flowed the sample being interrogated through a 1 mm path length flow cell (Starna) at $>$ 4 mL/s, which ensures a new sample of protein for every laser shot. During acquisition, samples were stored on ice. Linear absorbance spectra were acquired pre and post-acquisition to monitor for degradation.

2.4.7 Transient Absorption and Transient Anisotropy Measurements

The transient absorption apparatus is described in detail in the Supporting Information. Transient absorption measurements were performed for 800 nm pump – 850 nm probe for all four samples. The 800 nm pulse was the direct output of the regenerative amplifier system that operates at a 5 kHz repetition rate. At the sample position the pulse duration was measured by SHG-FROG to be <45 fs with ~30 nm bandwidth FWHM. White light supercontinuum was generated by focusing a portion of the regenerative amplifier output through argon [132, 133]. The white light was compressed and spectrally filtered in a prism compressor and the resulting pulse was centered at 850 nm with a bandwidth of ~35 nm, <45 fs pulse duration. The power was adjusted such that the pump was ~50 nJ per pulse and the probe was ~2 nJ per pulse using neutral density filters and a waveplate-polarizer pair that also served to set the relative polarizations between the pump and probe. In the anisotropy experiments, simultaneously collected parallel (V – V) and perpendicular (V – H) transient absorption data were used to compute the numerator (N) and the denominator (D) of the anisotropy given by $N = \Delta A_{V-V} - \Delta A_{V-H}$ and $D = \Delta A_{V-V} + 2\Delta A_{V-H}$. These functions were globally fit to extract the anisotropy decay rates and relative weight of each decay component [134]. For transient anisotropy measurements with 800 nm pump – 800 nm probe and 850 nm pump – 850 nm probe, the probe path polarizer was set to 45° relative to the pump path polarizer. The transmitted probe pulse was then split into vertical and horizontal components with a polarizing beamsplitter and the individual components were detected on photodiodes with each output sent to separate lock-in amplifiers and detected with two GPIB channels.

3 Chapter 3: Comparison of Energy Transfer Kinetics for Light-Harvesting Proteins of *Rhodobacter sphaeroides* and *Phaeospirillum molischianum*

3.1 Summary

In photosynthetic purple bacteria, light-harvesting occurs with a remarkable near-unity quantum efficiency. Light-harvesting complex 2 (LH2) is the primary light-harvesting complex, and has been extensively studied as a model system for the initial light-harvesting steps of photosynthesis. LH2 contains bacterichlorophyll organized into two concentric rings, known as the B800 and B850 rings (Figure 2A). However, the spectral and structural properties of these rings vary depending on the species and growth conditions. While the dynamics of some these variants have been exhaustively characterized, others have not been measured. Furthermore, a study of how structural differences between variants affect these dynamics has not been performed. In this work, we utilize ultrafast transient absorption measurements to compare the B800 to B850 energy transfer rates of three variants of LH2: LH2 from *R. sphaeroides*, LH2 from *Ph. molischianum*, and LH3 from *Ph. molischianum.* These variants differ in number of constituent subunits, the pigment geometry, and the absorption energies (Figure 4 and 5). We find striking differences in their B800 to B850 energy transfer rates. LH2 from *R. sphaeroides* is about 40% faster than LH2 from *Ph. molischianum*, which is consistent with predictions from Förster theory based on the increased distance between the pigment rings in structural models of *Ph. molischianum.* In contrast, LH3 from *Ph. molischianum* is only about 20% faster than LH2 in *Ph. molischianum* despite the greater spectral overlap between absorption bands, which would be expected to produce a much larger increase in energy transfer rate. The similarity in energy transfer rates suggests the presence of dark, higher-lying excitonic states that bridge the energy gap. Overall, these results provide insight into how small variations between and within species can be used to optimize energy flow in photosynthetic systems. This manuscript is in preparation by myself, Olivia Fiebig, Marcel Giansly, Professor James Sturgis, and Professor Gabriela Schlau-Cohen.

3.2 Results and Discussion

3.2.1 Linear Absorption Analysis

Figure 15 presents linear absorption and fluorescence spectra of LH2 from *Ph. molischianum* and *R. sphaeroides* and the low-light variant LH3 from *Ph. molischianum.* The absorption spectra (Figure 15A) from both variants of LH2 show the expected peaks at 800 nm and 850 nm, corresponding to the B800 and B850 bands respectively. In LH3, the B850 band blue-shifts to give rise to a peak at 820 nm, corresponding to the B820 band. The fluorescence spectra (Figure 15B), show a peak at 860 nm for LH2 and a blue-shifted peak at 853 nm for LH3, consistent with the absorption spectra. A comparison of the B850 absorption peak shows that it broadens from a width of 28.1 nm for LH2 from *R. sphaeroides* to 35.4 nm for LH2 from *Ph. molischianum.* Similarly, the fluorescence peak broadens from 26.6 nm in LH2 from *R. sphaeroides* to 29.9 nm in LH2 from *Ph. molischianum.* The broadened peak for *Ph. molischianum* indicates a difference in excitonic structure between the B850 bands of the two species, likely due to the two-fold weaker coupling between the B850 BChla in *Ph. molischianum.*

Spectral decomposition (Figure 16) of the 850 nm and 820 nm peaks for LH2 and LH3, respectively, from *Ph. molischianum* shows a contribution from both spectral variants in each sample. At least 5% LH3 is always present in LH2, and 10% LH2 in LH3. This small contamination

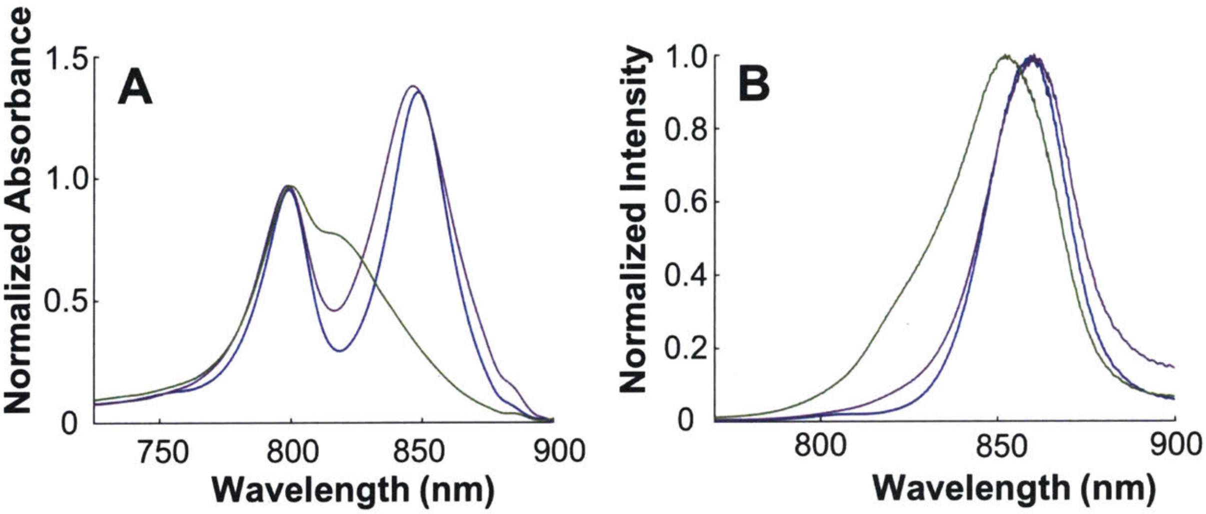

Figure 15: Linear absorption and fluorescence spectra of the three variants of LH2. LH2 from *R. sphaeroides* is shown in blue, LH2 from *Ph. molischianum* is shown in purple, and LH3 from *Ph. molischianum* is shown in green. (A) Room temperature linear absorption spectra normalized to unity at 800 nm. (B) Fluorescence emission spectra normalized to the emission maximum.

of spectral variants is confirmed by low temperature absorption spectra (Figure 17): LH3 from *Ph. molischianum* has a clear shoulder near 850 nm, indicating the presence of LH2. These results suggest a rapid timescale of interconversion in *Ph. molischianum*, and thus that 100% full conversion between LH2 and LH3 may not be possible. Notably, these results are in contrast to *Rps. acidophilla*, where 100% conversion of LH2 to LH3 has been reported with similar protocols [16].

3.2.2 Transient Absorption Spectroscopy

The B800 to B850 energy transfer rates in LH2 from *Ph. molischianum* and *R. sphaeroides* and LH3 from *Ph. molischianum* were directly compared with transient absorption (TA) spectroscopy. Figure 18 presents TA spectra for all three samples recorded at three different laser wavelengths. Figure 18A shows 800 nm pump – 800 nm probe data that reports on the decay in population of states at 800 nm (in the B800 ring) after its initial excitation, which is primarily due to B800 to B850 energy transfer on the femto- and picosecond timescale for magic angle polarization. The primarily overall negative TA signal is due to domination by ground state bleach of the 800 nm band, which decays on the short timescale due to energy transfer from B800 to the B850 and on the long timescale due to relaxation back to the ground state. Figure 18C shows 800 nm pump – 850 nm probe data that directly probes the time evolution of the population of states at 850 nm (in the B850 ring) after initial excitation of states at 800 nm (in the B800 ring), which grows in due to B800 to B850 energy transfer. The overall negative signal is due to ground state bleach and stimulated emission at 850 nm. Figure 18B shows 800 nm pump – 830 nm probe data. For LH2, this contains a combination of the signals in A and C and is positive due to the overall excited state absorption signal. For LH3 however, this probe wavelength directly probes the time evolution of the population of states at 820 nm (in the B820 ring) after initial excitation of states at 800 nm (in the B800 ring), resulting in the overall negative sign due to ground state bleach and stimulated emission around 820 nm, similar to what results for LH2 in the 800 nm pump – 850 nm probe data in 18C. The three spectra for each sample are globally fit to a sum of two exponentials as described

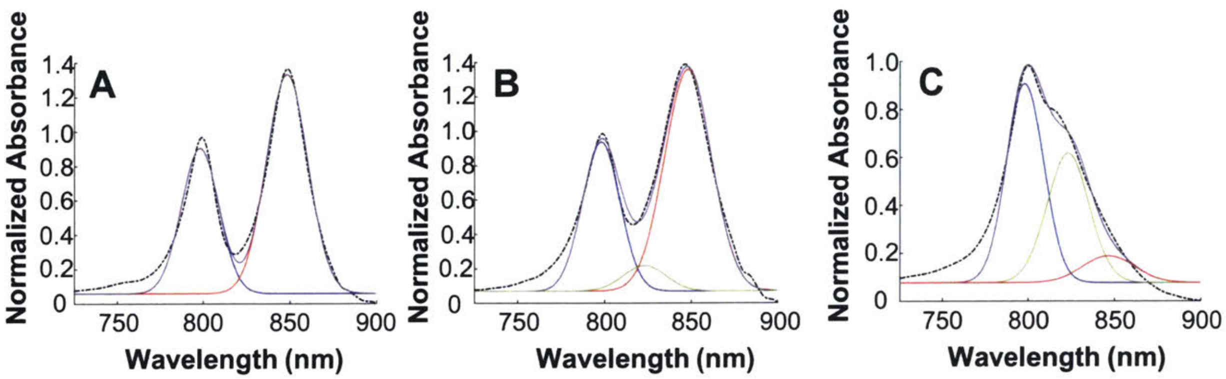

Figure 16: Spectral decomposition of the linear absorbance spectra for (A) LH2 of *R. sphaeroides*. The lnear absorption (black) is decomposed into a peak for B800 (blue) and B850 (red). (B) LH2 of *Ph. molischianum*. The lnear absorption (black) is decomposed into a peak for B800 (blue), B850 (red), and B820 (green). and (C) LH3 of *Ph. molischianum*. The lnear absorption (black) is decomposed into a peak for B800 (blue), B820 (green), and B850 (red).

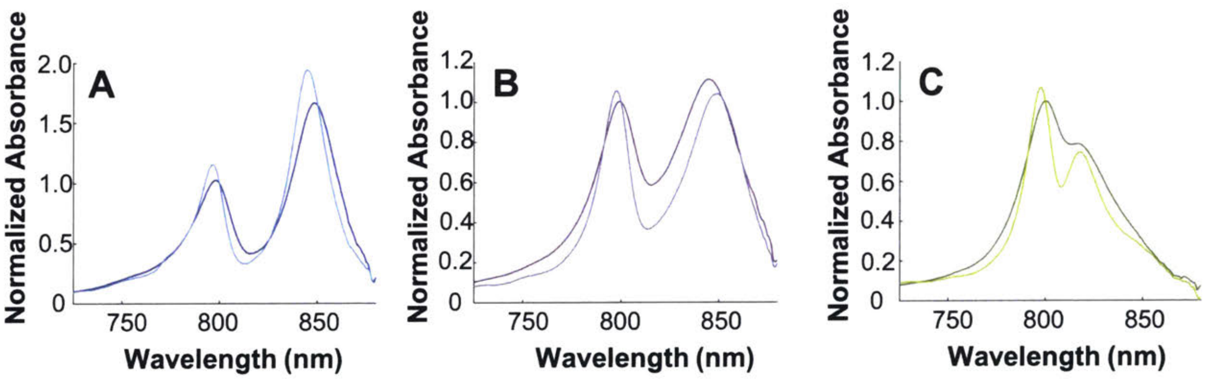

Figure 17: Overlay of room temperature and low temperature (80 K) linear absorption spectra (A) LH2 of *R. sphaeroides* (B) LH2 of *Ph. molischianum* and (C) LH3 of *Ph. molischianum*. The room temperature spectra are in darker colors and the low temperature spectra are in lighter colors.

in Appendix 2, the results of which are shown in Table 5. The first decay is assigned to energy transfer from B800 to B850 (or B820 for LH3). The second decay is assigned to relaxation back to the ground state, and is near-constant on the timescale investigated. The differences in structure between LH2 variants contribute to differences in the energy transfer rate within these systems, which appear as differences in the first decay (τ_1 in Table 5). We first discuss LH2 from the two different species and second LH2 and LH3 from the same species.

To probe the variation across species, LH2 from *R. sphaeroides* and *Ph. molischianum* were compared. These two LH2 variants have only marginal sequence percent identity of 26% and 31% between the α and β subunits, respectively, which causes several structural differences. LH2 from *R. sphaeroides* is a nonamer of $\alpha\beta$ heterodimers, whereas LH2 from *Ph. molischianum* is an octamer of heterodimers, providing a platform to compare oligomeric state. Due to the decreased number of subunits, the B800 pigments in *Ph. molischianum* are tilted 20° in comparison to those of *R. sphaeroides* (Figure 4A). Additionally, the Mg atoms are ligated differently between the two

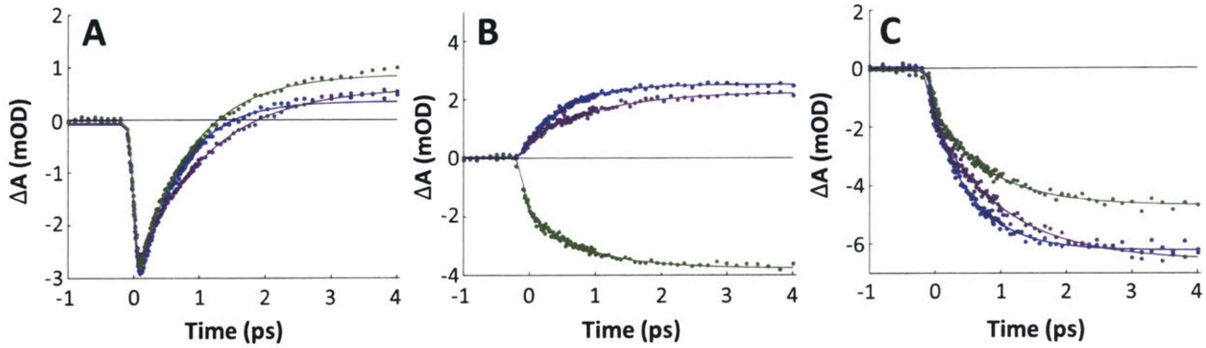

Figure 18: Transient absorption spectra of LH2 R. sphaeroides (blue), LH2 *Ph. molischianum* (purple), and LH3 *Ph. molischianum* (green) with (A) 800 pump – 800 probe, (B) 800 pump – 830 probe, and (C) 800 pump – 850 probe. The data were globally fit to two exponentials with the second exponential having a fixed time constant of 1 ns. Data are shown as points and the exponential fits are overlaid as lines.

	800 Pump - 800 Probe					800 Pump - 830 Probe			800 Pump - 850 Probe		
	$\tau1$	A1	$\tau2$	A2	RSME	A1	A2	RSME	A1	A2	RSME
LH2	630 fs	-89.9%	1 ns	10.1%	7.901e-5	-47.2%	52.8%	5.831e-5	44.3%	-55.7%	1.131e-4
LH2	1087 fs	-83.8%	1 ns	16.2%	4.981e-5	-43.4%	56.6%	6.731e-5	43.6%	-56.4%	1.311e-4
LH3	840 fs	-82.0%	1 ns	18.0%	6.541e-5	35.3%	-64.7%	8.791e-5	41.8%	-58.2%	1.121e-4

Table 5: Time constants (τ) and relative percent amplitudes (A) for magic angle 800 nm pump - 800 nm probe (left column), 800 nm pump - 830 nm probe (middle column) and 800 nm pump - 850 nm probe (right column) transient absorption for all three samples. LH2 from *R. sphaeroides* is in blue, LH2 from *Ph. molischianum* is in purple, and LH3 from *Ph. molischianum* is in green. Each spectrum was fit to a sum of two exponential decays fixing the second time constant at 1 ns. Root mean square deviations (RSME) are also listed.

species. The Mg atom of *Rsp. acidophilla* (our *R. sphaeroides* model) is ligated by a carboxylated N-terminal methionine and the Mg atom of *Ph. molischianum* is ligated by α-Asp6. This change in ligation rotates the B800 BChlas of *Ph. molischianum* 90° (Figure 4C). The rotation better aligns their Qy transition dipoles with those of the BChlas in the B850 band. Finally, in *Ph. molischianum*, the phytol tails of the B800 BChlas approach the B850 BChla as close as 4 Å whereas the closest approach within *R. sphaeroides* is 7.2 Å (Figure 4A), which can cause changes in Van der Waals interactions thus changing site energies. These changes in protein structure can vary the local electrostatic environments and the intermolecular interactions, both of which can dramatically affect energy transfer timescales.

The B800 to B850 energy transfer timescale is 630 fs in LH2 from *R. sphaeroides* as compared to 1087 fs in LH2 *Ph. molischianum*, and thus is approximately 40% faster in LH2 from *R. sphaeroides* (Table 5). The Mg-Mg distances between the B800 and B850 BChlas are 17.9 Å and 19.0 Å for *R. sphaeroides* (as determined from *Rsp. acidophila*, our model for *R. sphaeroides*) and *Ph. molischianum*, respectively (Figure 4B). Although the strong electronic coupling within LH2 means that energy transfer cannot be fully described by Förster theory, which can only be applied in the weak coupling limit [16], it can qualitatively capture the dynamics, in particular between the BChla in the B800 and B850 rings, which are more weakly coupled than the strong coupling within the BChla in the B850 band [135, 136]. Förster theory predicts that the energy transfer rate will scale to the sixth power as the distance between pigments increases. Based on this dependence, the distances between the B800 and B850 BChlas in *R. sphaeroides* are predicted to give rise to an energy transfer timescale approximately 30% faster than the distances in *Ph. molischianum*, similar to the relative timescales measured. The difference in timescales would perhaps be even more dramatic if not for the better alignment of the Qy transition dipoles in the B800 band with those in the B850 band in *Ph. molischianum* (Figure 4C). The alignment is expected to speed up energy transfer [137], and thus may be partially cancelling out the increase in distance between bands.

The B800 to B850 energy transfer timescale is 840 fs in LH3 from *Ph. molischianum* as compared to 1087 fs in LH2 *Ph. molischianum*, and thus is approximately 20% faster in LH3 (Table 5). The greater spectral overlap of the B820 band with the B800 band in LH3 would be expected to increase the energy transfer timescale much more than is observed. B800 to B850 energy transfer in LH2 is thought to partially occur through a higher set of optically dark B850 excited states that overlap with B800, called B850* [34,47,61,62]. Similarly, theoretical calculations of LH3 in *Rps. acidophilus* predict that the upper excitonic states of the B820 band overlap with and, in fact, are hidden under the B800 band [42]. Thus, the effective energy gap in LH2 is potentially much less than that observed in the absorption spectrum. The similarity in the measured energy transfer timescales between LH2 and LH3 supports these models, and points to the dark states playing a significant and general role in mediating energy transfer between the two rings of BChla across variants of LH2.

The similarity in energy transfer timescales also suggests that efficiency within the overall photosynthetic unit and/or energy capture is the primary reason for LH3 production, as opposed to changing the dynamics at the level of the individual antenna complex. Overall efficiency is determined by the rate-limiting step, which is energy transfer from LH1 to the reaction center for purple bacteria [138, 139]. The increased energy gap between LH3 and LH1 over that of LH2 and LH1 decreases the efficiency of back transfer, thereby allowing more time for energy transfer from LH1 to the reaction center and increasing the overall efficiency of this rate-limiting step. Increasing the rate of upstream steps, *i.e.*, energy transfer within LH3, would only create a bottleneck at the reaction center that could even induce photodamage upon a return to high light conditions. Whereas green plants have evolved additional complex photoprotective processes to dissipate excess energy as heat, purple bacteria only utilize the ability of carotenoids to quench potentially deleterious triplet states [140, 140, 141, 141, 142]. Furthermore, LH3 from *Rsp. acidophilla* contains a modified rhodopin glucoside with a π conjugation length increased by one. The increased conjugation length red-shifts the absorption and better fills the energy gap between the carotenoid absorption and the BChla Q bands. This spectral shift, along with the increased spectral coverage associated with the blue-shift of the B820 band, suggest the structural changes in LH3 are motivated by improved energy capture.

3.3 Conclusion

Although many species of purple non-sulfur bacteria co-exist in similar habitats, they have each developed unique strategies for light-harvesting including mechanisms to overcome the environmental pressures on their survival. Along with the variable oligomeric states of LH2 [18, 20, 143], most species have multiple gene sets that allow a variety of $\alpha\beta$ subunits to be mixed together, thereby creating spectral variants that broaden the window for light absorption and likely even increase the efficiency of energy transfer from LH1 to the reaction center [144]. Interestingly, although *R. sphaeroides* does not contain gene sets for spectral variants of LH2, it is has unique double LH1-

reaction center complexes resembling a figure eight shape [107]. Perhaps, there is an alternative mechanism for low-light adaptation in *R. sphaeroides* that involves this LH1-reaction center complex, which is yet to be discovered. The flexibility of LH2, however, is a particularly prevalent strategy, appearing across species. Our results demonstrate that the excited state manifold of LH2 is robust to variation in spectra, structure, and size. Therefore, these variations can alter the absorption, membrane organization, and energy transfer pathways through the photosynthetic unit while maintaining rapid and efficient energy transfer at the level of the individual LH2.

3.4 Materials and Methods

3.4.1 Purple Bacteria Growth

Wild type *Ph. molischianum* DSM120 was provided by the Sturgis lab and grown in Hutner's broth under anaerobic conditions. 500-mL of broth was bubbled with nitrogen for 1 hr in a 1-L bottle, sealed with an open cap and silicone septa, and then autoclaved for 20 minutes. Media was allowed to cool to room temperature and was inoculated with a live growing bacterial culture. For bacteria producing LH2, the flask was placed 6 inches from a 70 W Tungsten lamp to allow for high light and warm temperature (30° C) conditions. For bacteria producing LH3, the flask was placed 1 meter away from the lamp with a white paper napkin covering the flask to allow for low light and low temperature (23° C) conditions. Several rounds ($\approx$6-8) of inoculating new culture was necessary for conversion from LH2 to LH3 production. It was important to allow complete conversion, as it has been shown that there can be proteins containing a mixture of peptides from the LH2 and LH3 gene operons with intermediate spectral and electrostatic properties [12]. *R. sphaeroides* was grown as described previously [46].

3.4.2 Lysis and Purification of LH2 and LH3

Ph. molischianum cells were pelleted by centrifugation at 7500 rpm for 1 hour. Supernatant was discarded and pellets were resuspended in 20-mL of 20 mM Tris, 100 mM NaCl, 1 mM magnesium chloride, pH 7.5. Lysozyme was added to the solution to a final concentration of 100 μg/mL and allowed to stir at room temperature for 3 hours to remove the outer membrane and increase yield. The cells were lysed using a 5 min 30 s on – 30 s off probe sonication cycle with the sample in an ice bath. The remaining purification was done according to previous protocols [46] using *n*-Dodecyl β-D-maltoside (DDM) as the detergent. LH2 from *R. sphaeroides* was purified according to previous protocols using DDM as the detergent [46].

3.4.3 Linear Absorption and Fluorescence Measurements

Room temperature linear absorption measurements before TA measurements were taken on an Epoch microplate spectrophotometer (BioTek).

The low temperature linear absorption measurements were performed by drying each sample in a sugar matrix overnight in a quartz cuvette. The samples were placed in a cryostat that was depressurized and cooled down to 80 K using liquid nitrogen. A room temperature linear absorption spectrum of each sample was taken before each low temperature measurement on the same spectrometer for comparison. The absorbance spectra were recorded using a Cary 5000 UV–vis–NIR infrared spectrometer.

The fluorescence measurements were taken using a homebuilt fluorescence setup with 532 nm excitation, an 800 nm 150 g/mm grating, and a PIXIS CCD camera (Princeton Instruments).

3.4.4 Sample Preparation for Ultrafast Spectroscopy

After purification, LH2 variants were diluted to a final volume concentration of ~500 nM corresponding to ~1.5 OD at 850-820 nm in 20 mM Tris, 150 mM NaCl, pH 7.4, 0.1% DDM. A peristaltic pump flowed the sample being interrogated through a 1 mm path length flow cell (Starna) at > 4 mL/s, which ensures a new sample of protein for every laser shot. During data acquisition, samples were stored on ice. Linear absorbance spectra of all samples were acquired pre and post-acquisition to monitor for degradation.

3.4.5 Transient Absorption Measurements

The energy transfer kinetics of all three samples were measured using transient absorption spectroscopy at three wavelength conditions: 800 nm pump – 800 nm probe, 800 nm pump – 830 nm probe, and 800 nm pump – 850 nm probe. The transient absorption setup and analysis of the data is described in detail in Appendix 2. Briefly, the output of a 5 kHz regenerative amplifier was focused through a tube of argon gas to generate a white light-continuum [46] that was compressed and spectrally-filtered in a prism compressor. The 830 and 850 nm probe pulses were selected using 10-nm bandpass filters (FB840-10 and FB850-10, Thorlabs). The 800 nm pump pulse was taken directly from the output of the regenerative amplifier and spectrally-narrowed using a 10 nm bandpass filter (FB800-10, Thorlabs). The cross correlation was 100-120 fs depending on the wavelength conditions used. The spot size at the sample position was 300 μm. The pump and probe polarizations were set at the magic angle (54.7°) relative to each other. The pump power was set to 6 nJ and the probe power to 0.8 nJ using neutral density filters. The data was globally fit between all three pump-probe wavelength conditions to a sum of two exponential decays convolved with the pulse, with the time constants as shared fitting parameters. Time scales and the percent amplitudes (A) of each were extracteed from fitting.

4 Chapter 4: Inter-Protein Energy Transfer Between Antenna Complexes of Purple Bacteria

4.1 Summary

Within purple bacteria, the photosynthetic membranes are tightly packed with light-harvesting complexes [143, 145–148]. In fact, it is estimated that LH2 comprises 80% of the total protein within a cell [148]. The compostion and ratio of light-harvesting complexes and reaction centers contribute to the overall efficiency of excitonic energy transfer (EET) through the photosynthetic unit. Specifically, changes in the membrane composition are undergone in various cellular stress conditions that maintain the efficiency of the system [148]. LH2-LH2 inter-protein EET rates have been measured and modeled theoretically in whole cells, membrane chunks, chromatophores, and vesicles [30,35,149–151]. The EET rates were determined to be 1-5 ps. In whole cell and membrane chunks, these EET rates are averaged over many different interactions, including multiple lipid-protein and protein-protein interactions. With vesicles it is difficult to control the size of the vesicle as well as the number of proteins incorporated and the protein organization of the membrane is highly heterogeneous [152]. Additionally, one cannot easily employ ultrafast spectroscopy on vesicles or chromatophores due to their diameter being on the same scale as the experimental wavelength, causing a large amount of light scattering. Combining TA spectroscopy with membrane-discs will, for the first time, allow the identification of EET rates more directly within a near-native environment. The use of different sized membrane-discs can also be utilized to mimic different crowding effects of the proteins, which can be probed with spectroscopy to examine the effect crowding has on energy transfer kinetics (Figure 19).

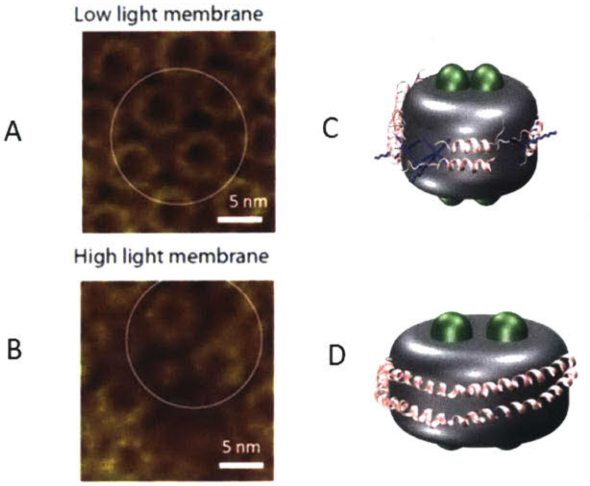

Figure 19: High resolution atomic force microscopy (AFM) of *in-vivo* membranes of purple bacteria [148]. (A) Under low light conditions more LH2 is produced and the membrane is more densely packed. (B) Under high light conditions less LH2 is produced and the membrane is less densely packed. (C) Telodendrimer (blue) nanolipoparticles. The size of belting protein 49Apo A1 (pink) provides a good model system for mimicking low light conditions of LH2 (green). (D) Membrane-Disc. The size of belting protein ApoE422K (pink) provides a good model system for mimicking high light conditions.

In this work, two light-harvesting complexes were incorporated into model membrane-discs of ~20 nm in diameter in order to look at energy transfer between the two in a simplified near-native system without a multitude of complex interactions (Figure 20). This doubly loaded membrane-disc yields a model-membrane environment that is tunable in composition and size. For inter-protein EET, the spectral variant LH3 must be used, as pumping at 800 nm and probing at 850 nm can indicate both intra- and inter-protein energy transfer. This allows the experiment to pump LH3 at 820 nm and probe LH2 at 850 nm, ensuring the majority of the spectroscopic signal is reporting on energy transfer between the two lower lying energy states.

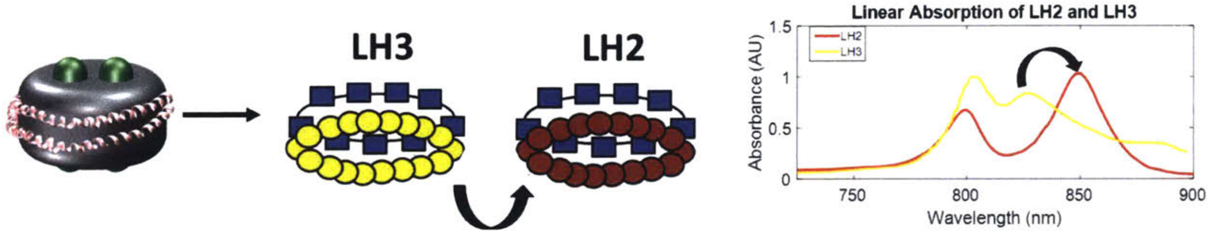

Figure 20: Schematic of experimental design for inter-protein energy transfer experiments using membrane-discs.

However, as all research thus far has been in complex membranes with multiple proteins, the exact architecture the two protein will adopt within the model membrane-discs is unknown. Although the vesicles, chromatophores, membrane chunks, and whole cells show tightly packed complexes, this may be due to the large amount of proteins embedded within the membrane which forces them close together. Alternatively, they may have an affinity for each other even without the external force of membrane protein packing. It has been shown that the LH2 packing within the native membrane does change with differing light conditions (Figure 19), which suggests the proteins would have the ability to dissociate from one another in a membrane-disc rather than being directly in contact with one another [148]. An additional complication arises when thinking about how the two proteins will be inserted into the model membrane-disc, such as their relative orientation to one another (Figure 21). The proteins may adopt the same orientation as *in vivo*, the opposite orientation, or as a mixture of the two orientations. As energy transfer rates are very sensitive to distance (r^{-6}) this may cause difficulties in interpreting the data without any information about the relative orientation or distances between the two proteins. The compounded effect of lacking information on the distance between the two proteins and their relative orientation can be seen in Figure 22. In Figure 22A, B the observed energy transfer kinetics should be quite different with $\tau_1 \ll \tau_2$. This expected difference is because the distance diagonally is greater than the horizontal distance between the B820 and B850 bands. The same logic can be applied to Figure 22C, D. However, in Figure 22E, the combination of the two effects could result in a similar distance between bands correctly oriented and those incorrectly oriented, thus complicating the analysis of the TA energy transfer data. One advantage to our technique for measuring the energy transfer kinetics of these proteins is that it is on a timescale much faster in magnitude (fs, ps) than diffusion of proteins within the membrane (ms, s). Therefore, this technique excludes the possibility of artifacts in the data due to changing distances between the two proteins during the experiment. But, the state of the variation of the initial sample is still important to interpret the final data.

4.2 Results and Discussion

LH2 and LH3 were successfully incorporated into membrane-discs (See Appendix 3 "Purification and Characterization of LH2 and LH3 Embedded Membrane-Discs Using ApoE422K" for protocols and characterization of these doubly loaded membrane-discs.). Initial experiments to characterize whether the discs were doubly loaded were completed. Firstly, fluorescence intensity was compared

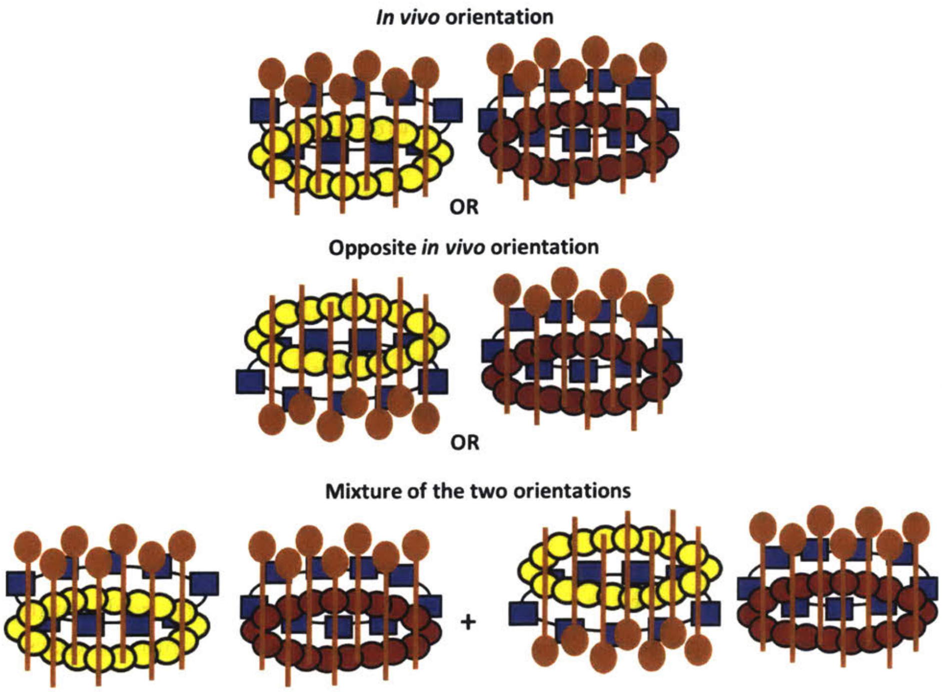

Figure 21: Schematic of the possible variable orientations within the membrane-discs with LH3 and LH2 embedded. Blue squares represent the BChla in the B800 band of both LH2 and LH3. Red circles represent the BChla in the B850 band of LH2. Yellow circles represent the BChla in the B820 band of LH3. Orange molecules indicate carotenoids.

among samples of LH2, LH3, a 50:50% mixture of the two detergent solubilized proteins from *Ph. molischianum*, and the doubly loaded membrane-discs (Figure 23A). In contrast to doubly loaded membrane-discs, in the 50:50% mixture of the two proteins, energy transfer cannot occur due to the long distances between particles in solution. The LH2 and LH3 fluorescence benchmarks the position and shape of their individual peaks. The fluorescence data indicates that there is a significant amount of LH3 fluorescence present in the 50:50% mixture but almost none of the LH3 fluorescence is seen in the membrane-disc sample. This lack of LH3 fluorescence suggests that there is energy transfer occurring within the doubly loaded membrane-discs and that one of each protein has been inserted into a single disc. A TCSPC fluorescent lifetime comparison of the 50:50% mixture of detergent solubilized proteins and doubly loaded membrane-discs (Figure 23B) was done. The doubly loaded membrane-discs show a biexponential decay with timescale of 96.4 ps and 1.34 ns and the 50:50% mixture of proteins shows monoexponential decay with a timescale of 1.7 ns. It is unclear why the doubly loaded membrane-discs showed biexponential decay. In previous literature, TCSPC was used to discern whether energy transfer and/or singlet-singlet annhilation is occurring within the membrane embedded proteins [72]. A monoexponential decay is seen when there is no protein-protein energy transfer occurring and a biexponential decay is observed when there is energy transfer due to singlet-singlet annihilation. However, the amplitude of the shorter time component was highly sensitive to excitation densities, suggesting singlet-singlet annhilation. The doubly loaded membrane-discs were insensitive to excitation densities and it is not likely that the biexponential decay shown is due to singlet-singlet annhilation. Perhaps the larger size of the doubly loaded membrane-discs produce scattering effects that contribute the shorter time component.

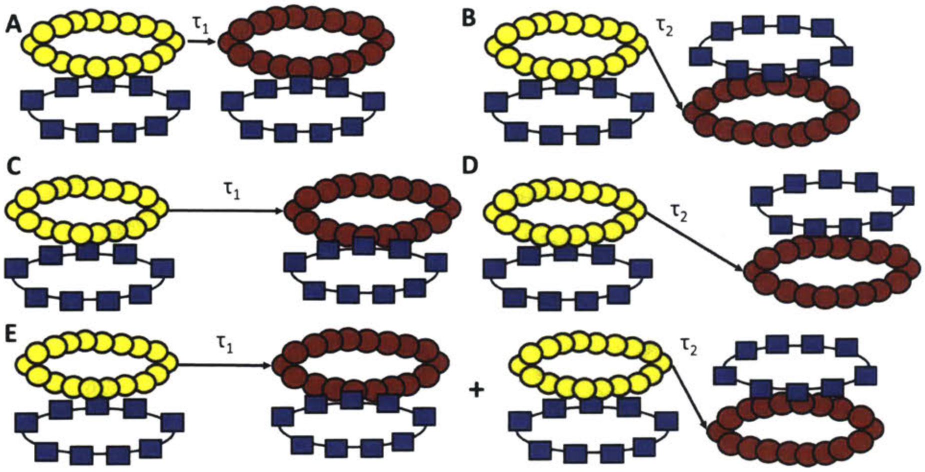

Figure 22: Energy transfer timescales change according to orientation and distance between two proteins within a membrane-disc. (A) Two proteins close together in correct orientation. (B) Proteins close together but in opposite orientation. (C) Proteins farther apart in correct orientation. (D) Proteins farther apart in opposite orientation. (E) Combination of distances and orientation.

To try and disentangle the structural features of the doubly loaded membrane-discs, many different biochemical technologies were considered. Previous studies have linked protein targets together to ensure their distances and orientations relative to each other using a number of different tools, such as complimentary DNA, tag specific linkers, click-chemistry, etc. [153–155]. However, the sequences of LH2 and LH3, their very small subunits that are almost entirely embedded in the membrane, and the repetitiveness of identical subunits makes protein modification and linking in just one spot on each protein very difficult. In this project particularly, gold nanoparticles were attached to the doubly loaded membrane-discs using primary amine chemistry (Figure 24). These were selected because they would label only one side of the protein (as both the α and β monomers have their N-termini on the same side of the whole protein), allowing identification of orientations and distances between proteins (Figure 24B). These nanoparticles were imaged using traditional negative stain TEM. Stoichiometrical ratios were selected to optimize for one particle to be attached to one protein. However, this proved difficult to optimize because the only available primary amines were at the amine terminus of each of the 16 monomers (Figure 24A), which gives 16 potential labeling sites for each protein. In fact, this technique proved to be to difficult to identify distances between two proteins in an individual membrane-disc for many reasons. Firstly, labeling the LH2 and LH3 complexes in detergent and then embedding them into the membrane-disc was unsuccessful most likely due to the detergent molecules perturbing labeling sites making them inaccessible. This complication required that labeling be done after the proteins were inserted into the membrane-discs, meaning that primary amines on the belting proteins were also susceptible to labeling. Labeling of belting protein increased the number of potential labeling sites from 32 to 62. Additionally, discerning which labels were on belting proteins and which were on light-harvesting complexes was more difficult (Figure 25A). It was assumed the labels close to the edge of the disc were attached to belting proteins but there is no certainty it is not a light-harvesting complex close to the edge of the membrane. Additional complications noticeable in Figure 25A, are that the discs can be different sizes. Unfortunately, as mentioned in Chapter 1, the larger the membrane-disc the less homogeneous the size becomes. Covalently circularized discs could potentially remove this ambiguity in future experiments. Lastly, as seen in Figure 25B, the label could attach to any site

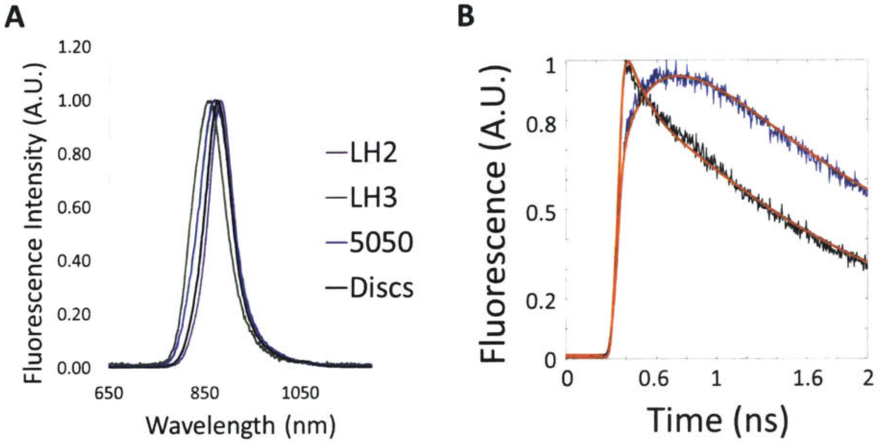

Figure 23: (A) Fluorescence intensity of LH2 (purple) and LH3 (green) from *Ph. moliscianum*, a 50:50% mixture of the two detergent solubilized proteins (blue) and the doubly loaded membrane-discs (black) (B) Fluorescence lifetimes of 50:50% mixture (blue) and doubly loaded membrane-discs (black).

on each protein making their relative location to one another very different despite the proteins locations being identical between two discs. Due to the number of labeling sites on each protein, the distance between labels does not accurately describe the distances between proteins (Figure 25B). Additionally, labels may attach to more than one site in each protein, making it difficult to discern if two labels are two different proteins or one protein.

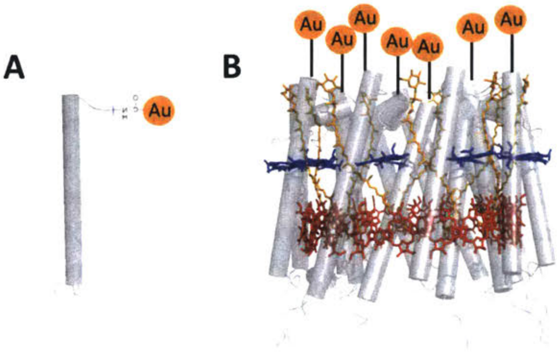

Figure 24: Experimental design to discern orientation and distances of two proteins embedded in membrane-discs. (A) Primary amine chemistry linkage to individual monomer of heterodimer. (B) Linkage of gold label only to N-terminal side of protein.

Alternatively, structural techniques could provide the information to disentangle the spatial and orientation information. Atomic force microscopy (AFM) imaging of the doubly loaded discs was done in collaboration with Peter Adams from the University of Leeds (Figure 26). A Brükner Fastscan AFM using Peak Force Tapping mode under liquid yielded images with ~2 nm spatial resolution. These images revealed successful incorporation of LH2 and LH3 into the membrane-discs. Statistical analysis of the well-resolved LH2 and LH3 determined that the complexes have a mean height of 4.75 ± 0.25 nm and mean diameter of 6.90 ± 0.59 nm (N = 26, 24, respectively), in agreement with previous AFM analyses of LH2 [143, 145, 146, 148]. Although streaking effects

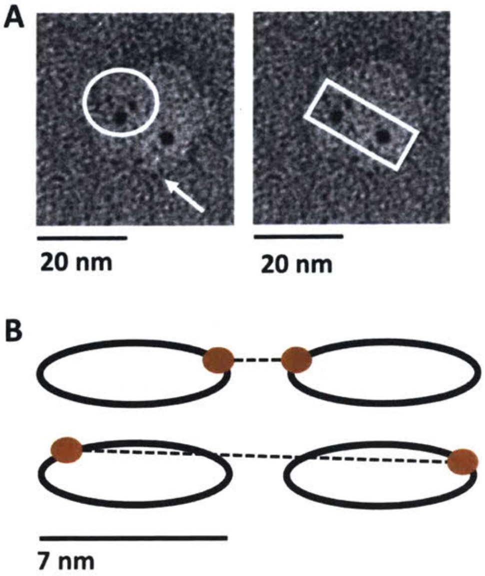

Figure 25: Labeling doubly loaded membrane-discs with gold nanoparticles. (A) TEM images of gold nanoparticle labeled doubly loaded membrane-discs. The circle indicates individual proteins multiply labeled. The square indicates two different proteins being labeled and the arrow indicates labeled belting protein. (B) Schematic of labeling variation that can produce distance information that is not an accurate description of protein distances.

in AFM caused partial clumping of membrane-discs, preventing definitive separation, out of the complexes that could be defined as LH2/LH3 (N = 29), approximately 55% were in "pairs" and 28% in "sets of four", and 10% were "single," showing successful association of proteins within the membrane-disc. Out of the "pairs", approximately two-thirds were adjacent (1 nm separation) and one-third was well separated (4-5 nm separation), revealing heterogeneous association within the membrane. These data suggest the two proteins do spatially vary in distance from one another from disc to disc.

An alternative strategy to discern the relative orientations or distances between proteins is using cryogenic electron microscopy (cryo-EM) to do single-particle reconstitution of the doubly loaded membrane-discs. A number of cryo-EM structural studies have been done on proteins embedded in membrane-discs [156–159]. To solve this problem, a high resolution structure may not be necessary, as a lower resolution structure could allow a decent fit of the many pigments within the protein and identify the correct orientation. The lack of need for high resolution is because incorrectly oriented pigments would show a variation in symmetry by comparison to the correctly oriented pigments. Then, by symmetry alone, it can be determined if one or two symmetrical populations are present and an approximate percentage of each. Additionally, if a top down view could be optimized during sample preparation, it may be possible to get an estimate of distances between complexes even at lower resolution. Optimization of sample preparation included varying sample concentrations as calculated in Appendix 3, choice of grids, and choice of blot times. Initially 0.25 mg/mL, 1 mg/mL, and 2.5 mg/mL concentrations were tested with blot times of 3, 5, and 7 s on standard R 1.2/1.3 carbon holey grids 200 mesh. Since 1 mg/mL at 5 s blot timed provided the best result from this set, a smaller concentration range was selected for optimization. The second round of optimization used 0.75, 0.1, and 0 1.25 mg/mL. Whereas 0.75 and 1 mg/mL both

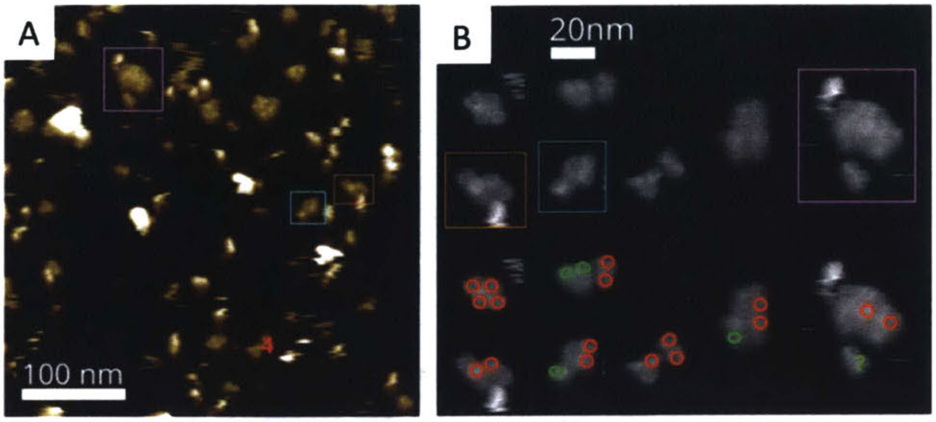

Figure 26: AFM images of discs loaded with two proteins. (A) Representative AFM image. (B) Regions of the AFM image containing discs loaded with one or more LH2 or LH3. Circular complexes are highlighted with red circles and squashed complexes are highlighted with green circles.

showed similar results, 1.25 mg/mL was too concentrated. This initial data set determined an effective concentration between 0.75 and 1 mg/mL. Because much of the sample also deposited onto the carbon outside of the holes, additional grids were tried. Standard R 1.2/1.3 carbon holey grids 300 and 400 mesh proved to be mostly similar to the 200 mesh. However, the smaller holes in 300 and 400 mesh produces less particles per hole but also slightly less visible aggregation as discussed below. Gold standard R 1.2/1.3 carbon holey grids 300 mesh improved the amount of protein within the holes and excluded more protein from adhering to the surface of the carbon outside the holes. The first data set of cryo-EM on the membrane-discs has been collected (Figure 27). It provides information that may make this technique very difficult to obtain the spatial and orientational information needed. As shown in Figure 27, there are several particles that are individual but the membrane-discs also seem to interact in a side-by-side fashion, organizing themselves into long strings. The main issue with this aggregation is that it makes it difficult to obtain enough individual particles for data analysis and structural reconstruction, as data collection is also a very time consuming process. The aggregation could potentially be due to belting protein interactions. The histidine tags on the belting proteins that are still attached could be causing this interaction. The histidine tags were cleaved from the belting protein and these experiments will be repeated. If cleaving the histidine tags does not improve the aggregation, other things could be tried, such as different grid types, using blot free grids, or adding surfactants. The second issue upon collecting the first data set is that no protein can be identified outside of the membrane-disc. The lack of protein density seen outside of the membrane is not surprising because the protein only protrudes from the membrane by $\sim$2 nm in the native organism. The major issue with very little protein density outside of the membrane is that this is the part of the protein that is used to do proper alignment during data analysis. Having little protein available for alignment may make analysis more difficult.

Initial TA experiments using just pump-probe TA with single wavelengths similarly to that described in Appendix 2, provided data that were very difficult to interpret, possibly due to the lack of information available on the spatial and orientational state of the two proteins in the membrane-disc. Because of the congested nature of the excited states of LH2 and LH3, this experiment requires the ability to detect multiple states simultaneously in order to get a clear picture of the energy transfer between the two protein complexes. To do this, it is necessary for the ultrafast TA spectroscopy setup to include spectrally-resolved detection. In the TA setup, the signal detection

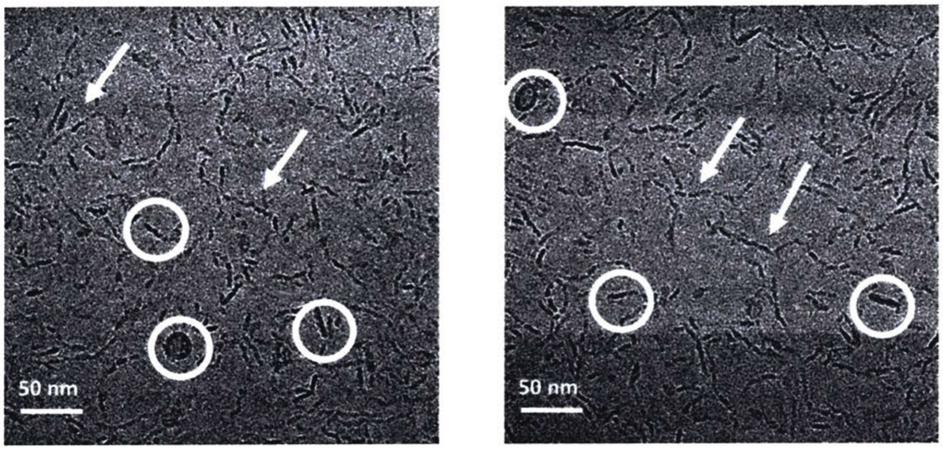

Figure 27: Initial Cryo-EM images of membrane-discs (~20 nm in diameter) containing two proteins. Although individual discs are observed (circles), discs interacting side by side also produce strings of discs making individual particle boundaries unidentifiable (arrows).

was limited to a single frequency and the setup was designed with spectral region access in the near-IR only. To expand the region in which dynamics can be probed, the spectral range was extended to access short laser pulses that can be used in a TA experiment. The detection module was reworked by adding two CCD arrays capable of achieving a spectral acquisition rate up to 37 KHz. Incorporating two fast CCD's in the detection allows spectrally-resolved TA experiments to be carried out on a shot-to-shot basis while taking into account any jitter or pulse-to-pulse instability. Overall, with the modified TA setup, the spectrally-resolved TA experiments on LH3 to LH2 energy transfer in the membrane environment will provide data with a higher signal-to-noise ratio while at the same time minimizing the data acquisition speed. Ultimately, it provides a more thorough probe of the excited state kinetics between these two proteins.

4.3 Conclusion

Although membrane-discs with LH2 and LH3 have been produced and partially characterized, there is still more characterization that needs to be done to understand the spatial and orientational information between the two proteins embedded in the membrane-disc. This information, in combination with the spectrally resolved TA setup, will allow the interpretation of the spectroscopic data to be more clear. Cryo-EM may provide the structural information necessary but it may prove to be a difficult challenge. Additional techniques, such as NMR, could also be used to obtain some structural information about the doubly loaded membrane-discs.

4.4 Materials and Methods

4.4.1 LH2 and LH3 Doubly Loaded Membrane-Discs

For doubly loaded membrane-discs containing LH2 and LH3 from *Ph. molischianum*, the belting protein ApoE422K was used as it was shown to produce larger sized discs [93]. The lipid chosen was DMPC as it is a native lipid to the organism, creates more stable discs across varying temperatures, and is cheap and accessible. Additionally, the first set of experiments comparing DMPC and POPC showed no significant changes in energy transfer rates between the two lipids [46]. Membrane-disc component ratios were first estimated based on calculations. A 20-25 nm membrane-disc was required to hold the two proteins, which are ~8 nm in diameter. The surface area of the proteins were estimated from the crystal structure [20]. The surface area of individual lipids was used from previous works [87]. The number of belting proteins to make this large of a disc was determined from previous works to be 6 ApoE422K [93]. This molar ratio of ApoE422K:LH2:LH3:DMPC was calculated to be 1:0.17:0.17:20. Complete double loading of every theoretically made membrane-disc was chosen in order to prevent a significant amount of singly loaded membrane-discs to form. Optimization of ratios was determined using FPLC (as decribed in Appendix 3 under "Optimization of Membrane-Disc Ratios by FPLC").

The optimal ApoE422K:LH2:LH3:DMPC molar ratio as determined by FPLC was mixed together at 1:0.125:0.125:22.2. The reaction was allowed to incubate on a rocker for 1 hr at room temperature. Bio-Beads SM-2 Resin was added to $^2/_3$ the volume of the reaction. Bio-Beads were allowed to incubate with the reaction on a rocker for 5 hrs at room temperature and then overnight at 4°C to ensure efficient detergent removal. Bio-Beads were removed through centrifugation.

The doubly loaded membrane-discs with LH2 and LH3 from *Ph. moliscianum* were purified by Ni-NTA. This purification step was to ensure the removal of any light harvesting complexes not embedded in discs. Some LH2 and LH3 did come through the flow through during this purification as expected due to the excess amount of photosynthetic complexes put into the initial reaction mixture. Doubly loaded membrane-discs were then purified by FPLC and characterized by SDS-PAGE, TEM, linear absorption, and fluorescence (as decribed in Appendix 3 under "Purification and Characterization of LH2 and LH3 Embedded Membrane-Discs Using ApoE422K").

4.4.2 Gold labeling of Doubly Loaded Membrane-Discs

C11-5-TNHS-DRY-50 functionalized gold nanoparticles (Nanopartz INC) were used to label the primary amine terminus of each LH2 and LH3 within the doubly loaded membrane-discs. All proteins and membrane-discs were buffer exchanged into 10 mM HEPES, 100 mM NaCl, pH 7.5 to prevent labeling of initial buffer components (Tris). Labeling of LH2 and LH3 in detergent was unsuccessful, likely due to the detergent blocking labeling sites. Labeling of doubly loaded discs was optimized by ratio of double membrane-disc to gold nanoparticle. Optimal ratio was very difficult to achieve but was determined to be 1:625 double-disc:gold nanoparticle. Labeling was carried out by dissolving the gold nanoparticle in 1 mL deionized water. Once the nanoparticle was reconstituted with water, it was used immediately because the functionalized ester is hydrolyzed in aqueous solution. The reconstituted gold nanoparticle solution was mixed with the dissolved protein at the ratio above. The reaction was incubated for 12-18 hours (overnight) at 4°C. Longer incubation times were not useful, as hydrolysis of the nanoparticle increases over time. The unbound gold particles were separated from the protein conjugates using gel filtration chromatography using a Superdex 200 Increase 10/300 GL (GE Healthcare Lifesciences) column. TEM samples were then prepared and imaged similarly to Chapter 2 (Materials and Methods).

4.4.3 AFM

AFM was performed on a Bruker FastScan AFM instrument using "Peak Force Tapping" imaging mode under liquid (an aqueous buffer of [20mM TRIS, 100mM NaCl, pH 7.5). Parameters were optimized whilst imaging to minimize applied forces, at low tapping amplitudes and moderate gains, typically scanning at 1–4 Hz and 1024 × 1024 pix. Topographs were processed and analysed using Nanoscope Analysis software (v1.8). Resolution is not normally precisely known with AFM as it depends on the AFM tip apex radius but was estimated to be around 2 nm. Sample concentration was determined as follows: starting from a stock of doubly loaded membrane-discs that had absorbance at 800 nm of approx. 1.3, samples were diluted between 1/10 to 1/50 and incubated with freshly cleaved mica for 60 min.

4.4.4 Cryo-EM

Calculation of the correct concentration of membrane-discs for Cryo-EM was done as follows. LH2-LH3 are 88,303 Da. ApoE422K is 21,943 Da. A single DMPC lipid is 678 Da. The ratio of membrane-disc components determined by optimization of membrane-disc reactions is 2 light harvesting complexes, 6 ApoE422K, and 120 DMPC which amount to a total weight of 389,614 Da or g/mol. Concentration of discs was found by identifying the concentration of LH2 by the absorption of the B850 band. That concentration and the molecular weight of the whole disc were used to find the membrane-disc concentration in mg/mL. Upon troubleshooting of CryoEM, a disc concentration of 0.75 to 1 mg/mL was optimal for data collection using a 5 s blot time and a blot force of 5 using a Vitrobot. Data were collected using a 200kV Talos Arctica with Falcon 3 direct electron detector. Individual micrographs were collected at 92kx magnification in integrating mode with an exposure of approximately 40 e- $\AA^{2}$

5 Conclusions and Future Outlooks

Overall, this work provides new insights and opens new underlying questions into light-harvesting within purple bacteria. This work illustrates the role of the membrane to shorten energy transfer timescales within the light-harvesting process of a single protein for the first time. Additional experiments, such as those described in Chapter 2, with light-harvesting proteins from other species of purple bacteria would be useful to determine if the shortening of the B800-B850 step is universal. Experiments altering the membrane lipid composition would also delve deeper into the role different membrane compositions may have on light-harvesting. Ultimately, the goal of light-harvesting within purple bacteria is to be efficient through the process as a whole, including the entire photosynthetic unit. Because increasing the rate of a single step may not benefit the overall efficiency, the effect the membrane has on various proteins in the photosynthetic unit or between species may vary. However, if every protein-protein energy transfer step is increased within the membrane then the complete light-harvesting process may be faster than believed previously. More work monitoring energy transfer in membrane-discs of various light-harvesting proteins, including LH1-RCs, between species would give a more comprehensive examination of the membrane's role in light-harvesting. This work begins to look at more protein-protein energy transfer steps in Chapter 4. Energy transfer steps of additional protein combinations can be examined within these membrane-discs, such as LH1-RC or LH2 to LH1-RC. Chapter 4 highlights some of the complications associated with monitoring energy transfer between two proteins within these discs. However, it provides many strategies that can be used to overcome obstacles. Finally, this work stresses the need to look at differences between these proteins under the same experimental conditions. Direct comparison of proteins from different species in Chapter 3 shows that, although many physical parameters influence energy transfer, the differences seen can be described by just distance, despite the changes in dipole orientations also being present. Looking at new spectral variants of LH2 (LH3) has brought forward important new fundamental questions. Despite the large increase in spectral overlap in LH3, the rates seem rather similar between LH2 and LH3. Although this is not the first time this phenomenon has been described in literature, it is the first time that this phenomenon has been shown to exist in other species besides *Rsp. acidophilla.* This suggests that the electronic structure of energy transfer in these proteins are indeed not fully characterized. Additional TA experiments, such as spectrally resolved pump-probe or two-dimensional TA, can further investigate the new questions brought forth from this work. A single-molecule-ultrafast technique may also provide more information on the heterogeneity between particles.

6 Appendix 1: Purification of Light-Harvesting Complexes of Purple Bacteria

6.1 Growth of *R. sphaeroides*

R. sphaeroides was grown in 1-L buffer bottles in media prepared from 1% tryptone (i.e. 10 grams/liter), 0.5% yeast extract (Sigma-Aldrich), 0.23 grams of NaCl, 810 μL of 1 M $MgCl_2$ or $MgSO_4$, and 510 μL of 1 M $CaCl_2$. Bottles were filled to top to reduce oxygen. Media was inoculated 1:100 v/v with live-growing cultures provided by the Blankenship Lab at University of Washington St. Louis. Bacteria were grown for three days at room temperature without shaking 1 m from a Tungsten light bulb (125 W, BR40 McMaster-Carr).

6.2 Growth of *Ph. moliscianum*

Wild type *Ph. molischianum* DSM120 was provided by the Sturgis lab at the Institute of Microbiology of the Mediterranean and grown in Hutner's broth (Figure 28) under anaerobic conditions. 500-mL of broth was bubbled with nitrogen for 1 hr in a 1-L bottle, sealed with an open cap and silicone septa, and then autoclaved for 20 minutes. Media was allowed to cool to room temperature and was inoculated with a live growing bacterial culture. For bacteria producing LH2, the flask was placed 6 inches from a 70 W Tungsten lamp (125 W, BR40 McMaster-Carr) to allow for high light conditions and warmer temperature (37°C). For LH3 producing bacteria, the flask was placed 1 meter away from the lamp with a white paper napkin covering the flask to allow for low light and low temperature (room temperature) conditions. Several rounds (~8-10) of inoculating new culture was necessary for full conversion to LH3 production. It was important to allow complete conversion of LH2 to LH3 production, as it has been shown that there can be proteins containing a mixture of peptides from the LH2 and LH3 gene operons with intermediate spectral and electrostatic properties [12]. Conversion of protein production was monitored with UV-Visible spectrophotometry by the shift between 820 nm and 850 nm. Cells were grown to late log phase after their linear absorption showed complete conversion to either LH2 or LH3.

6.3 Lysis of Light-Harvesting Complexes

Cells for both species were purified by the same protocol. Cells were spun down cells for 1 hr at 7,000 rpm by centrifugation in a Beckman Coulter Avanti J-26S XP using a JLA 8.1000 rotor at 4°C. They were resuspended in 20 mM Tris, 100 mM NaCl, 1 mM $MgCl_2$, pH 7.5 using 20-70 mL depending on the size of initial culture (20 for 500 mL and 70 for 1 L). DNase I (New England Biolabs) was added (300 units) to remove any DNA during lysis. 6 mg/mL of chicken egg white lysozyme (Sigma Aldrich) was added and allowed to incubate at room temperature for at least 3 hours. This removes the outer membrane of the cells, thus amplifying lysis and purified protein yield. Cells were then probe sonicated at 30% power for 5 min on ice for cycles of 30s on and 30s off. The lysate was pelleted by ultracentrifugation at 8,000 rpm for 1 hour in a Beckman Optima L-70K using a 60Ti rotor (Serial #3317) at 4°C. The soluble part was kept and the pellet of unlysed cells and debris was disgarded. The soluble portion was spun at 45,000 rpm in an ultracentrifuge (same as above) for a minimum of 4-18 hrs at 4°C. The next step is detergent solubilization. Once it is begun, the purification must continue in order to prevent the protein from being exposed to high detergent concentrations for long periods of time. If needed the ultracentrifugation step can be adjusted to be longer to prevent the necessity to leave protein in high concentrations of detergent. The length of this centrifugation step was adjusted according to what is necessary to continue steps consecutively. Freezing the preparation at any stage in this process is not recommended as

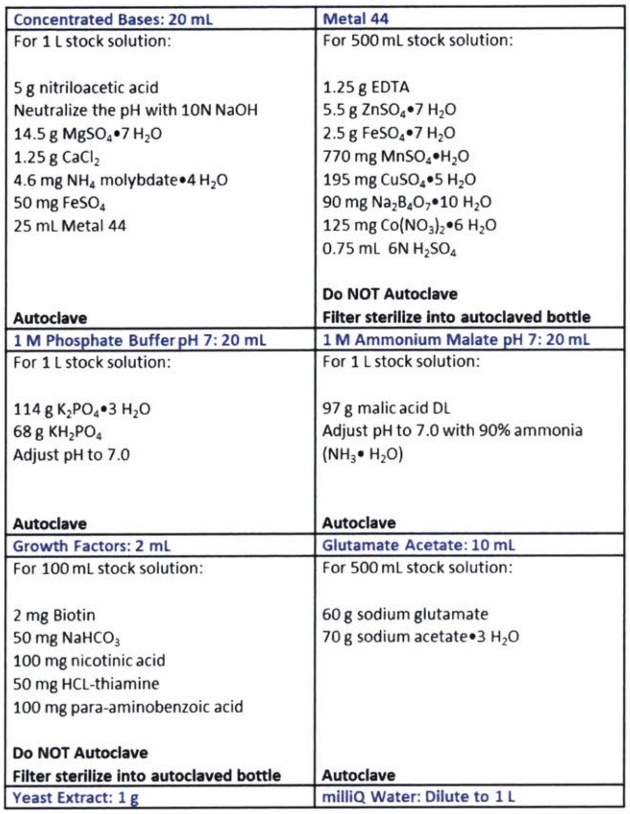

Concentrated Bases: 20 mL	**Metal 44**
For 1 L stock solution: 5 g nitriloacetic acid Neutralize the pH with 10N NaOH 14.5 g $MgSO_4 \bullet 7 H_2O$ 1.25 g $CaCl_2$ 4.6 mg NH_4 molybdate•4 H_2O 50 mg $FeSO_4$ 25 mL Metal 44 **Autoclave**	For 500 mL stock solution: 1.25 g EDTA 5.5 g $ZnSO_4 \bullet 7 H_2O$ 2.5 g $FeSO_4 \bullet 7 H_2O$ 770 mg $MnSO_4 \bullet H_2O$ 195 mg $CuSO_4 \bullet 5 H_2O$ 90 mg $Na_2B_4O_7 \bullet 10 H_2O$ 125 mg $Co(NO_3)_2 \bullet 6 H_2O$ 0.75 mL 6N H_2SO_4 **Do NOT Autoclave** **Filter sterilize into autoclaved bottle**
1 M Phosphate Buffer pH 7: 20 mL	**1 M Ammonium Malate pH 7: 20 mL**
For 1 L stock solution: 114 g $K_2PO_4 \bullet 3 H_2O$ 68 g KH_2PO_4 Adjust pH to 7.0 **Autoclave**	For 1 L stock solution: 97 g malic acid DL Adjust pH to 7.0 with 90% ammonia ($NH_3 \bullet H_2O$) **Autoclave**
Growth Factors: 2 mL	**Glutamate Acetate: 10 mL**
For 100 mL stock solution: 2 mg Biotin 50 mg $NaHCO_3$ 100 mg nicotinic acid 50 mg HCL-thiamine 100 mg para-aminobenzoic acid **Do NOT Autoclave** **Filter sterilize into autoclaved bottle**	For 500 mL stock solution: 60 g sodium glutamate 70 g sodium acetate•3 H_2O **Autoclave**
Yeast Extract: 1 g	**milliQ Water: Dilute to 1 L**

Figure 28: Recipe for Hutner's broth.

membrane proteins are more unstable when not properly solubilized. The pellet was resuspended in 20 mM Tris, pH 7.5. 1.5% lauryldimethylamine N-oxide (LDAO) or n-Dodecyl β-D-maltoside (DDM) was added dropwise while stirring on a stir plate at room temperature to solubilize protein. After 1 hour of solubilization, the solution was ultracentrifugated for 1 hour at 45,000 rpm at 4°C (same ultracentrifuge as above) to remove debris and aggregates. The supernatant was collected for purification. The linear absorption was taken after every step to monitor purification progress and make sure no significant damage comes to the protein preparation.

If desired, LDAO can be used for initial solubilization in order to simplify purification, as it destroys LH1. The protein can then be transfered into DDM after loading on the anion exchange column (See Section 5.4). Once on the anion exchange, 10 column volumes of 20 mM Tris, 0.1% DDM, pH 7.5 can be used to replace LDAO with DDM and ensure all LDAO is removed. Solubilizing *Ph. molischianum* complexes in LDAO is not recommended, as they are more unstable in this detergent and begin to dissociate.

6.4 Protein Purification

A HiPrep DEAE FF 16/10, 20-mL from GE Healthciences was equilibrated with 20 mM Tris, 0.1% LDAO or DDM, pH 7.5 on a Bio-Rad Fast Protein Liquid Chromatography (FPLC) system at 4°C. Protein was loaded onto the column through a sample pump. The column was allowed to be filled by 75% by monitoring the color change of the column as the protein was loaded. This allows the most protein to be added per run without loss of protein from over-saturation. Protein was eluted from the column using a salt gradient from 0% to 90% of 20 mM Tris, 0.1% LDAO or

DDM, pH 7.5 with secondary salt buffer of 20 mM Tris, 400 mM NaCl, 0.1% LDAO or DDM, pH 7.5. Flow rate was 0.75 mL/min and 1 mL fractions were collected for 15 column volumes (300 mL, this sets the salt gradient step size). This step was repeated until all protein had been ion exchanged. Re-equilibration of the column with 20 mM Tris, 0.1% LDAO or DDM, pH 7.5 was necessary to remove salt between multiple runs. Fractions were monitored at 280, 450, 575, and 800 nm. The edges of the peak with all four wavelengths was viewed more closely by taking a full linear absorption. The edge fractions with significant LH1 or RC contamination were discarded and all other fractions were concentrated to 5 mL for gel filtration. This was monitored by absorption peaks at 875 nm, shoulders on peaks at 800, 850, and 820 nm, and incorrect 800/850 nm or 800/820 nm peak ratios.

A HiPrep Sephacryl S-500 HR (GE Healthsciences) was equilibrated with 5 column volumes (600 mL) of 20 mM Tris, 0.1% LDAO or DDM, pH 7.5 on FPLC. The 5-mL of concentrated protein from anion exchange purification was loaded onto the FPLC through a 5 mL injection loop. Proteins were further purified at a flow rate of 0.75 mL/min in the same equilibration buffer. 2 mL fractions were collected for two column volumes (240 mL). Fractions were monitored at the same wavelengths and were subsequently collected and analyzed as the anion exchange purification step. The pure fractions were collected and inspected by UV-Visible spectrocopy (UV-Vis) and gel electrophoresis for purity. Purity was typically around 95%. Pure protein was aliquoted and flash frozen in liquid nitrogen and stored at -80°C.

Because 100% conversion between cells producing LH2 or LH3 is very difficult in this species, contaminating protein was taken into consideration using the following calculation. Both LH2 and LH3 contribute to the 800 nm absorption band equally. LH2 *R. sphaeroides* is used as a baseline because the species does not produce LH3. LH2 *R. sphaeroides* has a 800/850 nm peak ratio of 0.76. LH2 *Ph. molischianum* has a 800/850 nm peak ratio of 0.78. 0.78 - 0.76 = 0.02 which is due to the increase in absorption of the 800 nm band from LH3 contamination in LH2 *Ph. molischianum.* 0.02/0.78 *100 = 2.6% contamination of LH3. This typically varies between 2-5%.

LH3 has a 800/850 nm peak ratio of 1.2 due to the lower extinction coefficient of the 820 nm band in comparison to the B850. There is no standard from *R. sphaeroides* to use as a baseline. The absorption at 850 nm was found and used to calculate the 800 nm contribution using the known peak ratio. For example, X/0.210 = 0.76; X = 0.160. The 800 nm absorption maximum was used to get a percentage. For example, 0.160/1.737 * 100 = 9.2%. This typically varies from 5-25%. Alternatively, a spectral decomposition of the linear absorption or fluorescence can also give an estimate of amounts of contaminating protein in each prep as shown below.

6.5 Linear Absorption Spectral Decomposition

Figure 16 shows the spectral decomposition of the linear absorption spectra from the three variants of LH2. Since *R. sphaeroides* only produces LH2, its B800 peak was used as a standard for *Ph. molischianum* (Figure 16A). The B800 peak of LH2 and LH3 from *Ph. molischianum* were constrained to fit the B800 peak position and FWHM obtained from the *R. sphaeroides* fit. The B820 and B850 peak positions of LH3 and LH2 from *Ph. molischianum* were determined by fitting the spectra to two Gaussians initially. Then, the LH3 was fit to three Gaussians forcing the peak positions and FWHM of B820 and B850 from the two-Gaussian fits. The LH2 was fit to three Gaussians by forcing the B820 peak position and FWHM from LH3; however, the fit only converged to a physical result when the B850 peak was allowed to redshift by 1.6 nm from 846.7 nm to 848.3 nm. When the B850 peak was constrained to the peak position from the two-Gaussian fits, the area of the B820 peak in LH2 would become negative.

7 Appendix 2: Spectroscopy Experimental Set-Up

7.1 Spectroscopy System Layout

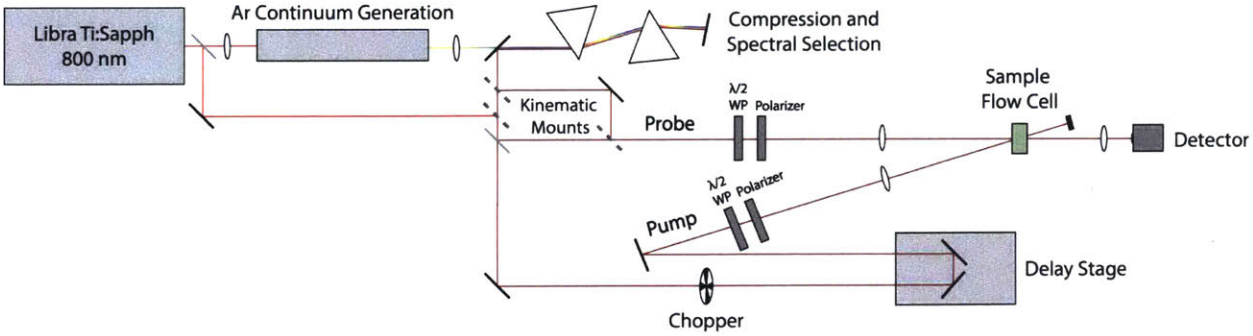

Figure 29: Schematic drawing of the transient absorption spectroscopy system in the Schlau-Cohen lab.

7.2 Transient Absorption Apparatus

The output of the regenerative amplifier (Libra, Coherent: 800 nm 40 fs, 5 kHz, 1 mJ per pulse), is split into two pulses. The pulse reflected off of the front face of the wedge (Figure 29) is used as the pump and probe for experiments using laser pulses centered at 800 nm while the transmitted pulse is used in 850 pulse generation, as discussed below. For one-color experiments, the pulse is steered through a beamsplitter where the pump and probe arms are generated. The pump arm is chopped to 1/2 repetition rate (2.5 kHz) and is delayed relative to the probe pulse by a retroreflector on a translation stage. This translation stage has 1 μm minimum step size, which equates to ~6.7 fs of time delay. The beams have independent waveplate-polarizer (WP) pairs to control power and polarization. Both beams go through 400 mm focusing lenses and the pump and probe beams are focused at the sample position with a crossing angle of $<10^o$. The spot size at the sample is 100 μm.

After the sample, the pump is blocked and the probe and reference (Figure 29) beams are recollimated with a 250 mm lens and detected on two photodiodes (Thorlabs). For all pump-probe conditions, the output of the two photodiodes is sent to an SR830 lock-in amplifier. For transient absorption experiments, the signals from the probe detector and from the reference detector are sent to the A and B channels of one lock-in amplifier and the lock-in is run in differential mode. The phase independent lock-in intensity is recorded via GPIB communication using a LabView program that also controls the delay stage. For transient anisotropy measurements, the signals from the probe and reference detectors are simultaneously measured via two separate lock-in amplifiers. The phase independent lock-in intensity is recorded for each of these signals.

7.3 850 nm Pulse Generation

The output of the regenerative amplifier is sent through a waveplate-polarizer (Meadowlark Optics) pair that sets the power to 3 W and is focused with a 1 m focal length lens into a tube of Argon to generate a high power supercontinuum. The Argon tube is held at 22 psi and has Brewster plate windows at the entrance and exit to minimize reflections. The tube is ~1 meter long and the focal spot is located 60 cm from the entrance window. The supercontinuum output is collimated with a 750 mm lens and sent into a prism compressor comprised of a double pass through a pair of fused silica prisms (Edmunds Optics). After the first pass the dispersed continuum is spatially filtered with a razor blade to select for 850 ± 20 nm. The pulse duration is measured to be <50 fs via second harmonic generagtion Frequency-Resolved Optical Gating (SHG FROG) at the sample position. For tighter control over pump and probe wavelengths, 10 nm bandpass filters were used. Pulse durations for smaller bandwidth experiments were measured to be 100-110 fs via SHG FROG at the sample position.

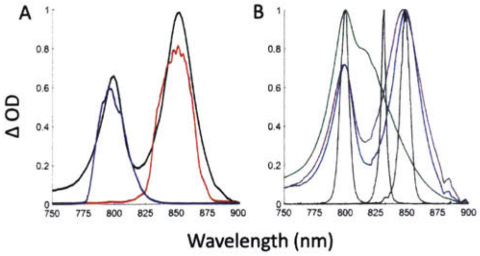

Figure 30: (A) LH2 absorption spectrum of the B800 and B850 bands for Chapter 2 experiments. The 800 nm regenerative amplifier output is shown in blue and the spectrally filtered supercontinuum pulse centered at 850 nm is shown in red. (B) LH2 and LH3 absorption spectra of the B800, B820, and B850 bands for Chapter 3 experiments. LH2 from *R. sphaeroides* is shown in blue. LH2 from *Ph. moliscianum* is shown in purple while LH3 is shown in green. Laser output pulses with 10 nm bandpass filters are shown in black.

7.4 Power Dependence Measurements

The power dependence of the energy transfer dynamics of LH2 were investigated to ensure spectral features seen were native to the system and not dependent on experimental parameters.

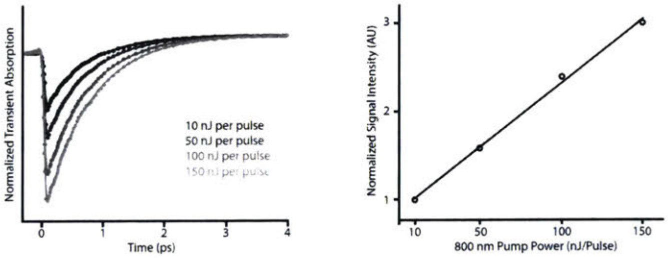

Figure 31: Power dependence data for the 800 pump - 800 probe data. Left: Magic angle data were acquired for LH2 solubilized in LDAO which were in agreement with the acquisition conditions used for the experiments shown in this work (50 nJ per pulse) in addition to two higher pump powers (100 and 150 nJ per pulse) and one lower pump power (10 nJ per pulse). All data was acquired with the same probe power, ~2 nJ per pulse. Right: Linear relationship of the maximum of the transient absorption signal scaled to the minimum pump power used.

7.5 Transient Absorption and Transient Anisotropy Measurements

The transient absorption apparatus is described in detail in the Supporting Information. Transient absorption measurements were performed for 800 nm pump – 850 nm probe for all four samples. The 800 nm pulse was the direct output of the regenerative amplifier system that operates at a

5 kHz repetition rate. At the sample position the pulse duration was measured by SHG-FROG to be <45 fs with ~30 nm bandwidth FWHM. White light supercontinuum was generated by focusing a portion of the regenerative amplifier output through argon [132,133]. The white light was compressed and spectrally filtered in a prism compressor and the resulting pulse was centered at 850 nm with a bandwidth of ~35 nm, <45 fs pulse duration. The power was adjusted such that the pump was ~50 nJ per pulse and the probe was ~2 nJ per pulse using neutral density filters and a waveplate-polarizer pair that also served to set the relative polarizations between the pump and probe. In the anisotropy experiments, simultaneously collected parallel (V – V) and perpendicular (V – H) transient absorption data were used to compute the numerator (N) and the denominator (D) of the anisotropy given by $N = \Delta A_{V-V} - \Delta A_{V-H}$ and $D = \Delta A_{V-V} + 2\Delta A_{V-H}$. These functions were globally fit to extract the anisotropy decay rates and relative weight of each decay component [134]. For transient anisotropy measurements with 800 nm pump – 800 nm probe and 850 nm pump – 850 nm probe, the probe path polarizer was set to 45° relative to the pump path polarizer. The transmitted probe pulse was then split into vertical and horizontal components with a polarizing beamsplitter and the individual components were detected on photodiodes with each output sent to separate lock-in amplifiers and detected with two GPIB channels.

7.6 Data Analysis Methods

For the transient absorption measurements, data was gathered, as described above, as a series of phase independent lock-in amplifier amplitudes. One such measurement was performed for each pump delay value. The delay values were spaced in three segments. The first segment has linear spacing from -300 or -100 fs (depending on the measurement) to +300 fs relative to t_o. The second segment goes from 300 fs to 1 ps with logarithmic spacing and the third segment goes from 1 ps to 4 ps with logarithmic spacing. In addition to acquiring data at each delay value, after each set of delay values, the lock-in amplifiers are set to acquire at the second harmonic of the reference frequency. This measurement is also stored via the LabView program and GPIB communication and is a measurement of the total power of the probe beam to be used in calculating the transient absorbance.

The data is analyzed by first computing the change in absorbance at each delay value. This is accomplished by directly computing the following:

$$\begin{aligned}\Delta\mathrm{Abs}(t_i) &= -\log_{10}\left(\frac{I(t_i)}{I_o}\right)\\ &= -\log_{10}\left(\frac{I_o + \Delta I(t_i)}{I_o}\right)\\ &= -\log_{10}\left(1 + \frac{\Delta I(t_i)}{I_o}\right)\end{aligned}$$

Where t_i is the i^{th} delay time, $\Delta\mathrm{Abs}(t_i)$ is the transient absorption signal at the delay time t_i, I_o is the total intensity of the probe, and $\Delta I(t_i)$ is the measured change in intensity of the probe signal by the lock-in amplifier. These absorbance values, as a function of delay, are computed for the Verticle-Vertical, Verticle-Horizontal, and Magic Angle data sets for each pump-probe condition and for each sample. Each set of three transient absorption decay curves is then fit with three exponential decay curves that share as global parameters the width of the convolved Gaussian (the IRF), and the time constants of decay. The relative weighting parameters for each of the three exponentials is allowed to vary for each polarization condition.

7.7 Calculation of Relative Energy Transfer Rates

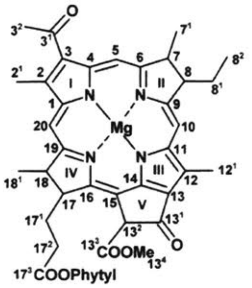

Figure 32: BChla molecule. Ring I nitrogen represents N_A. Ring II nitrogen represents N_B. Ring III nitrogen represents N_C. Ring IV nitrogen represents N_D.

To estimate the relative energy transfer rates, we use the diagonal form of the generalized Förster theory, which accounts for the coupling between chromophores within each ring and is known to provide adequate results for LH2 [40, 105]. The Multi-Chromophoric Förster energy transfer theory (MC-FRET) gives the resonant transfer rate between an aggregate of n_D donor molecules at equilibrium and n_A acceptor (Figure 32) molecules as

$$k_{DA} = \sum_{d,d'}^{n_D} \sum_{a,a'}^{n_A} V_{da} V_{d'a'} \int_{-\infty}^{\infty} d\omega \; E^D_{d'd}(\omega) I^A_{aa'}(\omega), \tag{1}$$

where the matrices $E^D(\omega)$ and $I^A(\omega)$ respectively account for the near-field emission and absorption spectra. The coupling between two chromophores separated by a distance $\vec{R}_{da}$ depends on the orientation factor $\kappa_{da} = \vec{\mu}_d \cdot \vec{\mu}_a - 3(\vec{\mu}_d \cdot \vec{R}_{da})(\vec{\mu}_a \cdot \vec{R}_{da})$, with $\vec{\mu}$ the transition dipole moments, and reads $V_{da} = K \mu_d \mu_a \kappa_{da} / R^3_{da}$, where K is a constant.

Following a series of approximations, an estimate of the pair-wise transfer rate relative to that in a reference geometry is obtained. First, the weak coupling between the B800 chromophores is used. In first order of the coupling, the emission tensor can be replaced by the monomer spectrum $E^D_0(\omega)$, as explicit e.g. using the approximation derived in Ref. [160].

The rate of interest thus becomes

$$k_{DA} = \sum_{d}^{n_d} \sum_{\alpha}^{n_a} k_{d\alpha} = \sum_{d,\alpha} V^2_{d\alpha} \int_{-\infty}^{\infty} d\omega E^D_0(\omega) I^A_\alpha(\omega), \tag{2}$$

now written in a diagonal form using the acceptor eigenbasis, with $V_{d\alpha} = \sum_a V_{da} \langle a|\alpha \rangle$.

Considering that the spectra from the different solubilization environments are only slightly shifted on the red part (Figure 9B), we approximate the spectral overlap as constant for the considered geometries. The pair-wise transfer rate for a B800 modified geometry $k_{d\alpha}(\theta)$ relative to that of a reference geometry (θ represents tilt angle) thus simplifies to

$$\tilde{k}_{d\alpha}(\theta) = \frac{k_{d\alpha}(\theta)}{k_{d\alpha}(0)} = \frac{V^2_{d\alpha}(\theta)}{V^2_{d\alpha}(0)}. \tag{3}$$

Using the geometry from PDB 1NKZ [104] as reference ($\theta = 0$), we obtain the direction of the transition dipole moments from the N_B to N_D atoms of each BChla (Figure 32). The tilt angle

θ is simulated shifting the vertical position of the N_B atoms on the BChlas of the B800 ring, and does not affect the B850 eigenbasis.

We verify that in the B800 ring, the rate between nearest neighbors is constant across the ring due to symmetry. For a given BChla on the B800 ring, the inter-ring transfer significantly depends on which B850 BChla serves as the acceptor. Figure 14 shows the B800-B850 relative rate obtained from averaging pair-wise rates, calculated between a fixed B800 BChla and each eigenstate formed by its six nearest B850 BChlas. Note that the enhancement of the B800-B850 rate mainly comes from the contribution of transfer to two BChlas in the six nearest neighbours, for which the tilt drastically influences the transfer rates. Also, the B800-B850 rate is very sensitive to the distance R, and hence the model chosen for the tilt. Disorder on the coupling can smooth this sharp dependence [106].

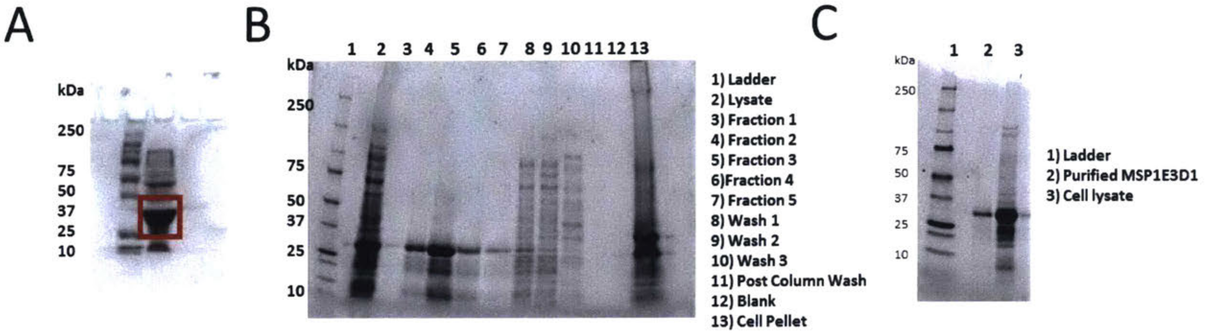

Figure 33: SDS-PAGE of expression and purification of MSP1E3D1 belting protein for membrane-discs. (A) Successful over-expression of 32.6 kDa MSP1E3D1. (B) His-tag purification of MSP1E3D1. (C) Purified MSP1E3D1 is approximately 95% pure.

8 Appendix 3: Assembly of Model-Membrane Discs

8.1 Production of Membrane-Disc Belting Protein MSP1E3D1

Over-expression of disc belting protein MSP1E3D1 was adapted from previously reported protocols [86,87]. The plasmid for the belting protein MSP1E3D1 was acquired from Addgene (plasmid #20066) containing a 6X histidine tag and kanamycin antibiotic resistance. MSP1E3D1 was transformed into One Shot BL21 Star (DE3) Chemically Competent *E. coli* (ThermoFisher Scientific #C601003) and glycerol stocks were made by flash freezing in liquid nitrogen and storing at -80°C. Over-expression was carried out on a shaker at 37°C. A 10-mL starter culture of Luria Bertani Broth was inoculated with the glycerol stock and grown overnight. The starter culture was used to inoculate 1-L of terrific broth. Protein over-expression was induced between 0.6-0.8 OD (at 600 nm) with a final concentration of 1 mM isopropyl β-D-1-thiogalactopyranoside. Cells were allowed to produce protein for 5-6 hours. The cell pellet was collected by centrifuging at 3,000 rpm at 4°C for 20 minutes in Beckman Coulter Avanti J-26S XP using a JLA 8.1000 rotor. The supernatant was discarded and the cell pellet was resuspended in 25 mL of 20 mM Tris, 150 mM NaCl, pH 7.4. Phenylmethylsulfonyl fluoride was added to a final concentration of 1 mM. Triton X-100 was added to 0.1% v/v. DNase I (New England Biolabs) was added (300 units) with a final concentration of 2.5 mM for magnesium chloride and 0.5 mM calcium chloride. Solution was homogenized in a tissue homogenizer. Solution was probe sonicated on ice for 5 minutes at 30% power for 30 seconds on and 30 seconds off. Solution was centrifuged at 4,000 rpm in an Eppendorf 5810 R using an A-4-62 rotor at 4°C for one hour to remove cellular debris. The supernatant lysate was loaded onto a 25-mL Ni-NTA chromatography column and allowed to equilibrate with the beads on a nutating mixer at 4°C overnight. Protein purification was carried out by previously established protocols [86,87]. The eluted protein was dialyzed 3 times with 1 L of 20 mM Tris, 100 mM NaCl, 0.5 mM EDTA, pH 7.4 to remove excess imidazole. Protein mass was verified by reverse-phase liquid-chromatography mass-spectrometry (LC-MS). Purity was determined by denaturing gel electrophoresis (SDS-PAGE, Figure 33) . To ensure there was no nucleic acid contamination, the 260/280 nm ratio was inspected by UV-VIS. Protein was concentrated to $\sim$500 μM and aliquoted into 50 μL aliquots, flash frozen in liquid nitrogen, and stored at -80°C for later experiments.

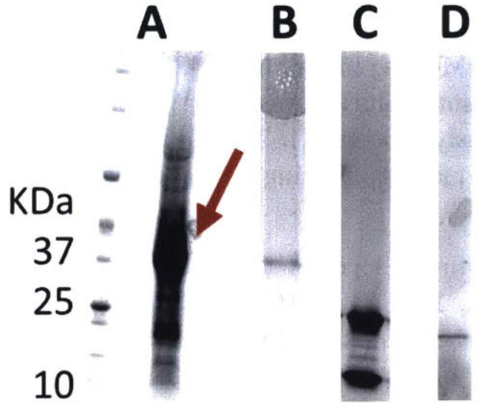

Figure 34: SDS-PAGE gel monitoring after each purification step of ApoE422K. (A) Post over-expression showing successfully made fusion-protein (red arrow). (B) Purified fusion-protein. (C) Cleaved fusion-protein showing the ApoE422k and thioredoxin as separate bands, both of lower molecular weight than the fusion-protein. (D) Final pure ApoE422k after removal of histidine tag.

8.2 Production of Membrane-Disc Belting Protein ApoE422K

Over-expression of disc belting protein ApoE422K was adapted from previously reported protocols [87, 161] (Figure 34). The plasmid for the belting protein ApoE422K was ordered from DNA 2.0. It contained a thioredoxin fusion-protein to improve *in vivo* solubility and increase expression of the belting protein, a thrombin cleavage sequence to remove the thioredoxin during purification, a 6X histidine tag, and kanamycin antibiotic resistance. Growth, lysis of the cells, and purification of protein were carried out just as the steps for the MSP1E3D1 shown above (Figure 34A, B). The eluted protein was dialyzed against 20 mM Tris, 100 mM NaCl, 5 mM EDTA, pH 7.4 to remove excess imidazole. Thrombin (Thermofisher, Catalog RP-43100) cleavage was then carried out by adding 10 μL of thrombin solution (10 cleavage units) per mg fusion protein and allowing the reaction to incubate at room temperature for 12 hours with gentle agitation from rocking. The cleaved protein was loaded onto a Ni-NTA column once again as described above (Figure 34C). Purification was carried out by washing with 50 mM Tris-HCl, 300 mM NaCl, 20 mM imidazole, pH 8.0 for 5 column volumes. Protein was eluted with 50 mM Tris-HCl, 300 mM NaCl, 400 mM imidazole, pH 8.0 for 3 column volumes in 5 mL fractions. The eluted protein was once again dialyzed against 20 mM Tris, 100 mM NaCl, 5 mM EDTA, pH 7.4 to remove excess imidazole. TEV protease (New England Biolabs) was added to the eluted and dialyzed protein according to the company's protocol. The reaction went over night at 4°C on a nutating mixer. The TEV protease and cleaved tag were removed with Ni affinity chromatography. The solution was resuspended on the Ni-NTA column and allowed to mix at 4°C for at least 3 hours to ensure all TEV protease and cleaved tags were bound to the column. The column flow-through and washes from 10 column volumes of 20 mM Tris, 150 mM NaCl, pH 7.5 was collected and concentrated to a final ApoE422K concentration of 500 μM (Figure 34D). Characterization and storage of protein was similar to that for MSP1E3D1. Protein was aliquoted, flash frozen and stored at -80°C for later experiments.

8.3 Lipid Preparation

1,2-dimyristoyl-sn-glycero-3-phosphocholine (DMPC) and 1-palmitoyl-2-oleoyl-sn-glycero-3-phosphocholine (POPC) were purchased from Avanti Polar lipids (#850345C and #850457, respectively). 1 mL of chloroform solubilized lipid was placed in culture tubes. Chloroform was evaporated under a gentle stream of argon gas and dessicated overnight under vacuum. Lipid was resuspended in 500 μL 20 mM Tris, 150 mM NaCl, 200 mM sodium cholate, pH 7.4 and sonified in a Branson Ultrasonic Bath until solution was clear. The concentration of lipid was determined by a phosphorus assay as previously reported [162]. Lipids were degassed of oxygen to prevent oxidation by bubbling in nitrogen, aliquoting, freezing in liquid nitrogen, and then storing at -80°C for later experiments.

Alternatively, the powdered form of the lipid (Avanti Polar Lipids) can be purchased and resuspended in 20 mM Tris, 150 mM NACl, 100 mM NaCholate, pH 7.5 according to the stock concentration provided by the company. Lipid concentration with this method was verified with the above phosphorus assay multiple times to be correct within 5%.

8.4 Loaded Membrane-Disc Reactions

Singly loaded membrane-discs incorporating LH2 from *R. sphaeroides* were produced using a construct from the common apolipoprotein ApoA1, MSP1E3D1 [80,86]. Empty membrane-disc reactions were prepared by the well-established protocol and ratio of MSP1E3D1 to DMPC [87]. A 1:160 ratio of MSP1E3D1: DMPC was used for empty membrane-discs. A new MSP1E3D1:DMPC molar ratio was determined for LH2 membrane-discs because some of the lipids are displaced by LH2. From the crystal structure of LH2 of *Rps. acidophila*, which is predicted to have a very similar structure to *R. sphaeroides*, the surface area of LH2 was calculated to be 314 nm^2 [17,18]. The surface area of DMPC is 5.7 nm^2 approximating that 55 lipid molecules will be displaced [81,86,87,91]. The surface area of POPC is close to that of DMPC, so the approximation that approximately 55 lipid molecules would be displaced was also used. The ratios were eventually experimentally optimized. Therefore, a molar ratio of MSP1E3D1: DMPC/POPC was changed to 1:105 rather than 1:160 when taking into consideration the incorporation of LH2 into discs. These ratios were selected to yield discs that were 1/4 filled with LH2 to prevent contamination of LH2 not embedded in the disc or multiply embedded proteins. Because not all of the discs will contain LH2, a new lipid ratio was calculated taking into consideration the weighted average of loaded to empty membrane-discs. LH2 membrane-disc reactions were incubated with the MSP1E3D1:LH2 molar ratios of 1:0.25 (50% loaded) and 1:0.125 (25% loaded). Small scale reactions of 250 μL and 100 μM MSP1E3D1 were initially used for troubleshooting Volumes were increased at fixed concentration for upscaling. MSP1E3D1:LH2:DMPC/POPC molar ratios were titrated around initial calculations to find the optimal ratio as described in the Section 7.8.

In final experimental samples, MSP1E3D1:DMPC/POPC:LH2 were mixed together with molar ratios of 1:131:0.125, which were experimentally determined optimal ratios. Bio-Beads SM-2 Resin was added to 2/3 the volume of the reaction. Bio-Beads were allowed to incubate with the reaction on a rocker for 1 hr at room temperature for DMPC and 4°C for POPC and then overnight at 4°C for both to ensure efficient detergent removal. Because, lauryldimethylamine oxide (LDAO) was used to solubilize antenna complexes in this reaction, the reaction was allowed to incubate on a rocker for 1 hr at room temperature for DMPC and 4°C for POPC, as LDAO is efficiently removed in this time frame as advised from collaborators in the Blankenship Lab at Washington University St. Louis. Bio-Beads were removed through centrifugation.

For doubly loaded membrane-discs containing LH2 and LH3 from *Ph. molischianum*, the belting protein ApoE422K was used as it was shown to produce larger sized discs [93]. The lipid chosen was DMPC as it is a native lipid to the organism, creates more stable discs across varying

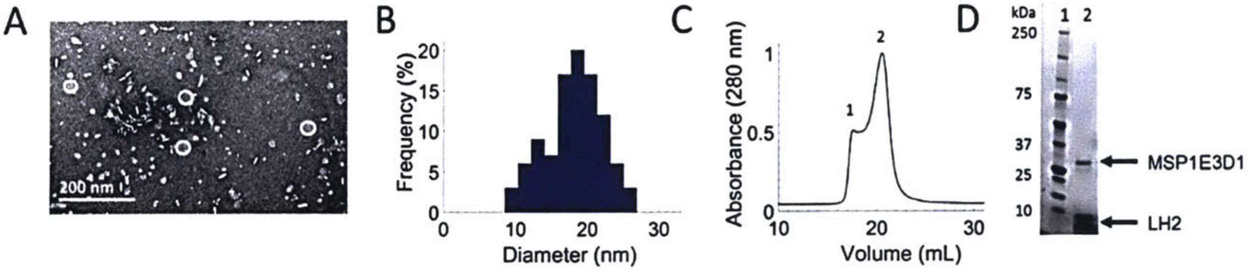

Figure 35: Successful incorporation of LH2 into membrane-discs using DMPC. (A) TEM image of FPLC purified LH2 discs. (B) TEM size distribution of >100 LH2 discs. Some 12 ± 2 nm empty discs remain after purification. LH2 discs are 20 ± 5 nm. (C) Size-exclusion chromatography from FPLC of LH2 discs. Peak 1 contains larger aggregates and peak 2 contains LH2 discs. (D) SDS-PAGE of peak 2 (C) from FPLC showing both the belting protein and LH2.

temperatures, and is cheap and accessible. Additionally, the first set of experiments comparing DMPC and POPC showed no significant changes in energy transfer rates between the two lipids [46]. Membrane-disc component ratios were first estimated based on calculations. A 20-25 nm membrane-disc was required to hold the two proteins, which are 8 nm in diameter. The surface area of the proteins were estimated from the crystal structure [20]. The surface area of individual lipids was used from previous works [87]. The number of belting proteins to make this large of a disc was determined from previous works to be 6 ApoE422K [93]. This molar ratio of ApoE422K:LH2:LH3:DMPC was calculated to be 1:0.17:0.17:20. Complete double loading of every theoretically made membrane-disc was chosen in order to prevent a significant amount of singly loaded membrane-discs to form. Optimization of ratios was determined using FPLC (See section Optimization of Membrane-Disc Ratios by FPLC below).

Based on optimization for doubly-loaded discs, the optimal ApoE422K:LH2:LH3:DMPC molar ratio was mixed together at 1:0.125:0.125:22.2. The concentration and volumes of reaction for initial trouble shooting were identical to that for singly loaded membrane-discs and volumes were increased at fixed concentration for upscaling. Because n-Dodecyl-β-Maltoside Detergent (DDM) was used for purification of these light-harvesting proteins, reactions were allowed to incubate on a rocker for 5 hours at room temperature and then overnight at 4°C with Bio-Beads to ensure efficient detergent removal as advised from collaborators in th Wagner group at Harvard Medical School, as DDM is more difficult to remove than LDAO. Bio-Beads were removed by centrifugation.

8.5 Purification and Characterization of LH2 Embedded Membrane-Discs Using MSP1E3D1

The singly-loaded membrane-disc reactions with *R. sphaeroides* and DMPC (Figure 35) or POPC (Figure 36) were purified by the 6× histidine tag of the belting protein on a 1 mL Ni-NTA column to remove any LH2 not incorporated into discs. The reaction was allowed to equilibrate with the beads for 1 hr at 4°C on a nutating mixer. Column flow-through was collected and the column was washed with 1 mL of 40 mM Tris, 300 mM NaCl, 20 mM imidazole, pH 8.0 three times. Discs were eluted with 40 mM Tris, 300 mM NaCl, 400 mM NaCl, pH 8.0. Fractions containing discs, as determined by SDS-PAGE, were dialyzed against 20 mM Tris, 100 mM NaCl, 0.5 mM EDTA, pH 7.4 to remove imidazole. Determined by SDS-PAGE, no excess LH2 was present in the flow-through or washes, indicating 100% incorporation of LH2 into discs.

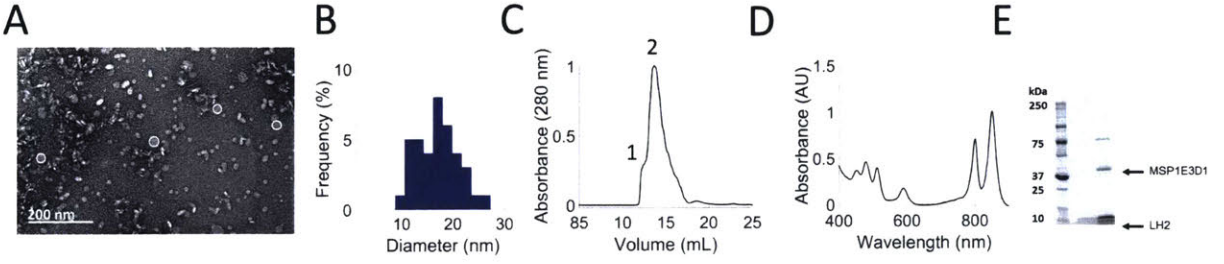

Figure 36: LH2 in discs using MSP1E3D1 and POPC. (A) TEM image of FPLC purified LH2 discs. (B) TEM size distribution of >100 LH2 discs. A bimodal distribution shows empty discs of 12 ± 5 nm and LH2 discs are 20 ± 5 nm. (C) Size-exclusion chromatography from FPLC of LH2 discs (peak 2). (D) Absorption Spectra of LH2 in discs using POPC shows the integrity of LH2 structure. (E) SDS-PAGE of LH2 peak (C) from FPLC shows both the belting protein and LH2.

Singly-loaded LH2 from *R. sphaeroides* and empty membrane-discs (Figure 37) were further purified by FPLC with a BioLogic DuoFlow (Bio-Rad) on a Superdex 200 Increase 10/300 GL (GE Healthcare Lifesciences) at a flow rate of 0.75 mL/min with 20 mM Tris, 150 mM NaCl, pH 7.4. Fractions of main peaks were collected and analyzed by SDS-PAGE, linear absorption, and TEM. The membrane-disc peak was collected, flash frozen in liquid nitrogen and stored at -80°C for future experiments.

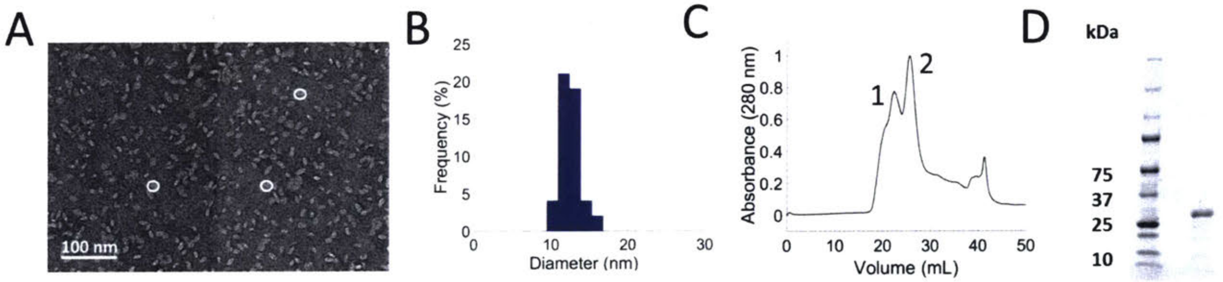

Figure 37: Empty discs using MSP1E3D1 and DMPC. (A) TEM image of FPLC-purified discs (Peak 2 from C). (B) TEM size distribution of >100 LH2 discs. Empty discs are 12 ± 2 nm. (C) Size-exclusion chromatography from FPLC discs. Peak 2 contains discs. Fractions beyond peak 2 showed no protein on SDS-PAGE and is attributed to excess lipid. (D) SDS-PAGE of Peak 2 (C) from FPLC shows only the belting protein.

8.6 Purification and Characterization of LH2 and LH3 Embedded Membrane-Discs Using ApoE422K

The doubly loaded membrane-discs with LH2 and LH3 from *Ph. moliscianum* were purified by Ni-NTA using the same protocol as that for the singly-loaded discs. This purification step was to ensure the removal of any light harvesting complexes not embedded in discs. Some LH2 and LH3 did come through the flow through during this purification as expected due to the excess amount of photosynthetic complexes put into the initial reaction mixture. Doubly loaded membrane-discs were then purified by FPLC and characterized similarly to the singly-loaded discs above. Additionally, the fluorescence of the doubly loaded discs were compared to that of LH2, LH3, and a 50-50% mixture of the two solubilized in detergent as described in Chapter 4. The fluorescence from LH3 is almost completely diminished in the doubly loaded membrane-disc sample. Monitoring the linear absorption and the structural composition of the sample by TEM indicates that the proteins are inserted into membrane-discs without aggregates present.

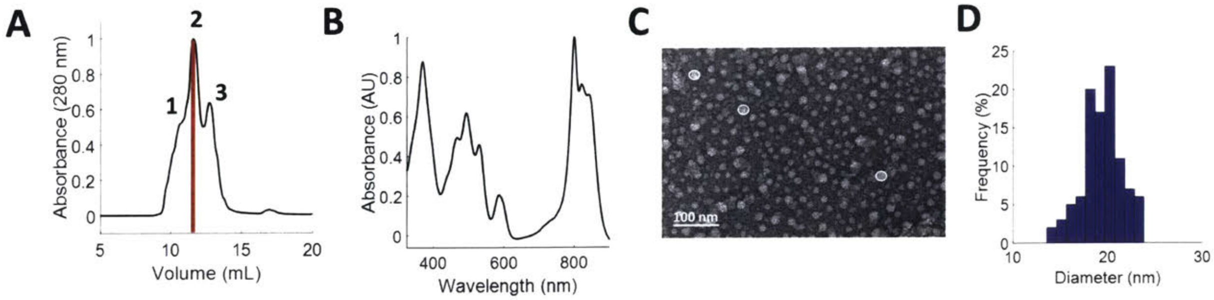

Figure 38: (A) FPLC trace of membrane-discs with two proteins embedded. The red slice represents the doubly loaded membrane-discs that underwent further characterization. (B) Linear absorption of doubly loaded membrane-discs. (C) TEM image of membrane-discs with two proteins embedded. (D) Distribution of doubly loaded membrane-disc particles.

8.7 Optimization of Membrane-Disc Ratios by FPLC

Monitoring the elution of the singly loaded LH2 from *R. sphaeroides* and empty membrane-discs at 280 yielded two peaks for each sample on the FPLC traces (Figure 39A-C). A shift to shorter elution volumes for the LH2 (14 mL) versus empty (16 mL) membrane-discs suggests a slightly larger size for the LH2 membrane-discs (Figure 39A, B). Upon increasing the amount of membrane-discs loaded with LH2 from 25% to 50%, an increase in height of peak 1 and a decrease in height of peak 2 can be observed (Figure 39B, C). This suggests that peak 1 contains LH2 membrane-discs. SDS-PAGE confirms only MSP1E3D1 is present in empty membrane-disc reactions while MSP1E3D1 and LH2 are present in both peaks for the LH2 membrane-disc reactions (Figure 39D). Due to the overlap of the peaks, this is expected. A high loading of purified MSP1E3D1 on SDS-PAGE indicated that there are some protein contaminants (10%), which have been identified with an antibody that recognizes the hexahistidine tag as smaller fragments of MSP1E3D1 using Western Blot analysis. This is due to its susceptibility to *in-vivo* degradation [86]. The removal of these contaminants is not possible with nickel-affinity purification by the hexahistidine tag because each contaminating fragment contains the tag. While these fragments could form discs themselves that contribute to peak two, they are likely too small for incorporation of LH2 since UV-visible spectrophotometer data confirm that most LH2 is incorporated into peak one (Figure 39E). Peak 2 on the LH2 membrane-discs FPLC trace may contain empty membrane-discs, excess MSP1E3D1, or smaller discs formed from the MSP1E3D1 contaminants. Empty membrane-discs may also contribute to peak 1 due to their similarity in size to the loaded membrane-discs. Spectroscopic separation of the target protein from empty discs is achievable due to its lack of absorption in the near-infrared wavelength range. Because LH2 and empty membrane-discs can be spectrally resolved, it is not an issue to have both contained in the sample.

Optimization of membrane-discs containing two complexes was done similarly to the protocol used for singly loaded discs. Due to the large excess of protein put into these reaction mixtures, many aggregates were formed. Optimization was determined by decreasing the aggregate peak and increasing the doubly loaded membrane-disc peak (Figure 40).

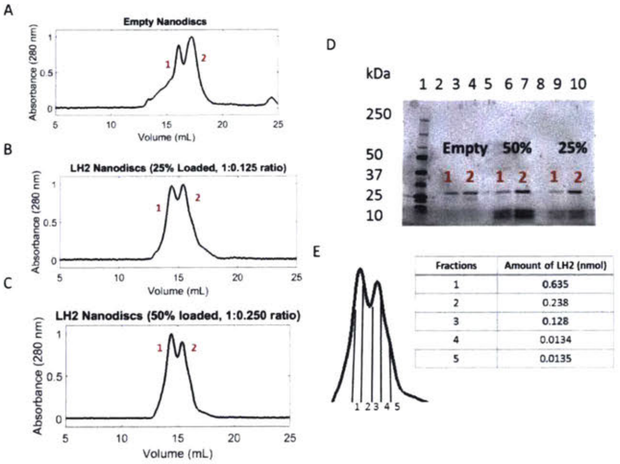

Fractions	Amount of LH2 (nmol)
1	0.635
2	0.238
3	0.128
4	0.0134
5	0.0135

Figure 39: FPLC of Nanodiscs. (A) Empty Nanodiscs. (B) LH2 Nanodiscs with discs 25% filled. (C) LH2 Nanodiscs with a 50% of the discs filled. (D) SDS-PAGE of FPLC peaks showing only MSP1E3D1 (32.6 kDa) for the empty discs peaks 1 and 2 (lanes 3-4) and both MSP1E3D1 and LH2 (5.4, 5.6 kDa) for the LH2 Nanodisc peaks 1 and 2. 50% loaded discs (lanes 6-7) and 25% loaded discs (lanes 9-10). (E) Table with LH2 quantified at 850 nm from fractions that were collected across the peaks of the LH2.

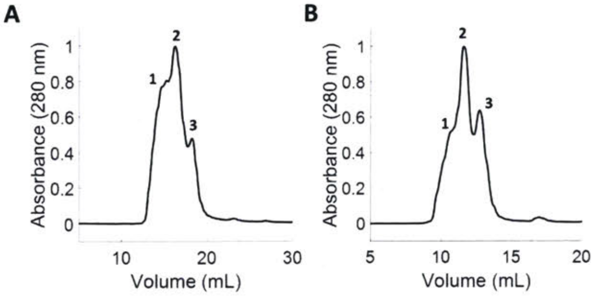

Figure 40: (A) FPLC trace of membrane-discs before optimization. (B) FPLC trace of membrane-discs after optimization. The aggregate peak 1 is decreased while the doubly loaded disc peak 2 is maintained. Peak 3 is singly loaded and empty discs.

8.8 Membrane-Disc Stability

The stability of membrane-discs with a single LH2 from *R. sphaeroides* at 4°C was monitored by TEM and linear absorption (Figure 41). The linear absorption does indicate a small increase in scattering over the Rayleigh range with time, indicating aggregation. In agreement, the TEM distribution of sizes also indicate aggregation with time. The linear absorption, which is normalized to the B850 peak, identifies the loss of BChla from the B800 band, thus reducing its absorbance. From these results, samples were given a lifetime of seven days at 4°C.

8.9 Linear Absorption and Fluorescence Measurements

Room temperature linear absorption measurements before TA measurements were taken on an Epoch microplate spectrophotometer (BioTek).

The low temperature linear absorption measurements were performed by drying each sample in a sugar matrix overnight in a quartz cuvette. The samples were placed in a cryostat that was depressurized and cooled down to 80 K using liquid nitrogen. A room temperature linear absorption spectrum of each sample was taken before each low temperature measurement on the same spectrometer for comparison. The absorbance spectra were recorded using a Cary 5000 UV–vis–NIR infrared spectrometer.

The fluorescence measurements were taken using a homebuilt fluorescence setup in the Bawendi Lab at MIT with 532 nm excitation, an 800 nm 150 g/mm grating, and a PIXIS CCD camera (Princeton Instruments) as the detector.

8.10 Transmission Electron Microscopy

TEM samples were prepared on 400-mesh Cu-carbon coated films (Electron Microscopy Sciences) that were negatively glow-discharged for 60 s at -15 mA in a Pelco easiGlow. 5 μL of sample with appropriate dilution, as determined by trial and error by analyzing TEM images, was added to the grid the for 1 minute. Excess sample was removed with Whatman filter paper from the edge to prevent deposition of fibers onto the grid. 5 μL of 2% ammonium molybdate tetrahydrate was added for 30 seconds. Excess stain was removed similarly to the sample. 5 μL of 2% uranyl acetate in water was added for 30 seconds. Excess stain was removed similarly as above. Excess stain was removed similarly to the sample. Samples were allowed to air dry for at least 1 min. Samples were imaged on a FEI Tecnai (G2 Spirit TWIN) at 120 kV. The distribution of disc sizes was analyzed using more than 100 particles by ImageJ software (https://imagej.nih.gov).

8.11 Cryo-EM to Discern Relative Orientation of LH2 and LH3 in Membrane-Discs

Calculation of the correct concentration of membrane-discs for Cryo-EM was done as follows. LH2-LH3 are 88,303 Da. ApoE422K is 21,943 Da A single DMPC lipid is 678 Da. The ratio of membrane-disc components determined by optimization of membrane-disc reactions is 2 light harvesting complexes, 6 ApoE422K, and 120 DMPC which amount to a total weight of 389,614 Da or g/mol. Concentration of discs was found by identifying the concentration of LH2 by the absorption of the B850 band. That concentration and the molecular weight of the whole disc were used to find the membrane-disc concentration in mg/mL. Upon troubleshooting of CryoEM, a disc concentration of 0.75 to 1 mg/mL was optimal for data collection using a 5 s blot time and a blot force of 5 using a Vitrobot.

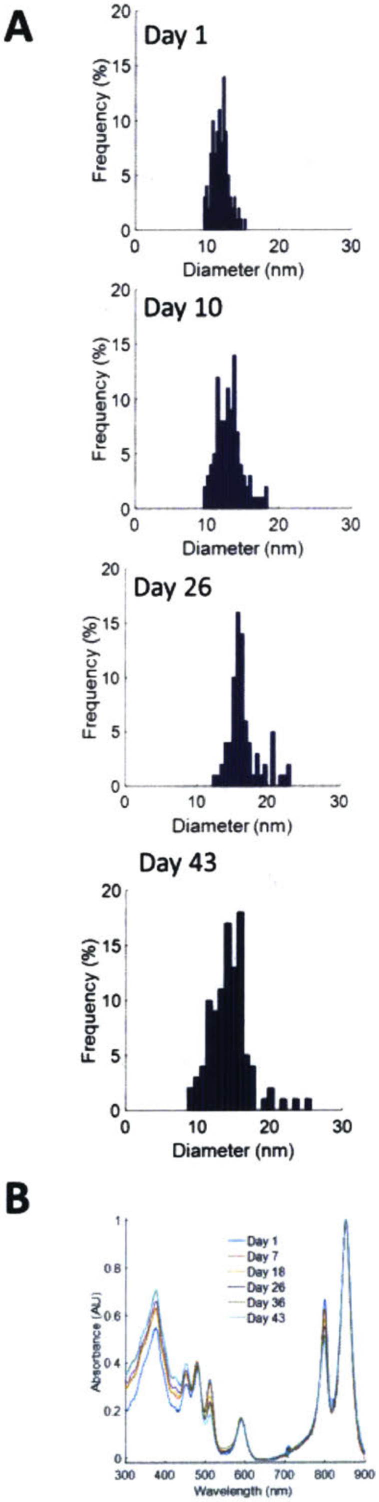

Figure 41: (A) TEM size distribution of membrane-disc particles over 43 days (B) Change in linear absorption of membrane-discs over 43 days

9 Acknowledgements

A number of people have contributed scientifically and provided support throughout this project and my graduate studies. I am grateful for the mentorship and scientific insight of my graduate adviser Professor Gabriela Schlau-Cohen. Thank you for providing a supportive research environment to grow and develop my scientific expertise. Your keen physical insight and ability to think about fundamental questions broadly and in depth has given me new ways to think about important scientific questions. Thank you for articulating and teaching me many new physical principles and your patience as I learned them for the first time. Thank you for understanding and encouraging work-life balance for my family and I. Being a parent during graduate studies has often been challenging but you have always provided me with support and encouragement in all situations. I am also grateful for Professors Alex Shalek and Cathy Drennan for always having an open door.

All of the members of the Schlau-Cohen group have been supportive colleagues and friends. They have all provided suggestions and useful ideas without hesitation and provided a fun and scientifically exciting environment. A special thank you to Dr. John Ogren for teaching me optics. As someone with almost no background in optics or physics, you're patience and incredible ability to teach allowed me to learn complex new principles even with my limited background. I owe thanks to Olivia Fiebig for her collaboration in this work. Thank you for your physical insight and technical proficiency in optics. I am honored to have had the chance to work beside you, to mentor you, and to now call you friend. Thank you to Minjung Son for discussing physical principles within this project with me and providing me with insightful ways to think about the fundamental questions. Thank you to Dr. Toru Kondo and Wei Chen for your additional help carrying out fluorescence experiments. Thanks to Jesse Gordon for all the laughs in our office. Your whimsical humor changed my bad mood more than you know. To the rest of the Schlau-Cohen group, thank you for your continued support, for always having an ear to listen, and for your friendship. I would also like to acknowledge the Muddy for getting me through tough days and weeks. I will miss making memories with my groupmates at the Muddy Charles.

Professor Robert Blankenship and Professor James Sturgis generously provided bacterial strains of purple bacteria and many proteins and patiently answered my many questions. Thank you to Dr. Marcel Giansily and Dr. Yue Lu from their labs for aiding me with protocols and also answering all of my questions. Thank you to Professor Jianshu Cao and Dr. Aurelia Chenu for your collaboration with theoretical predictions within this work. Thank you to Professor Moungi Bawendi and Professor Anthony Schwartz for the use of their instrumentation. I would like to thank Professor Elizabeth Nolan and Dr. Toshiki Nakashige for supporting me and teaching me biochemistry my first summer at MIT. Your mentorship provided me with a skill set that allowed me to set up the Schlau-Cohen lab as the first graduate student. Many thanks to Professor Joanne Stubbe for allowing me to work in her lab my first year as our lab space was being renovated and to Dr. Kanchana Ravichandran for providing support and for answering any and all biochemistry questions as I ventured into uncharted waters on my own. I owe thanks to Professor Martin Bollinger and Professor Carsten Krebs for their mentorship during my summer REU. Thank you to Dr. Laren Rajakovich for teaching me new skills during my REU and being so patient. This greatly contributed to my success as a graduate student. Many many thanks to Professor Gretchen Anderson and all of my undergraduate professors. Your encouragement to dive into science and apply to graduate school was life changing. Your teaching was top quality and gave me the preparation necessary to become a knowledgeable scientist.

Thank you to my husband Dustin and my daughter Atlanta for being supportive, understand-

ing, and encouraging throughout these years. Your constant support kept me motivated to be my best self. A special thaanks to my mother Nina Byler who taught me that no matter what hand you ar dealt, you can build the hand you always wanted in the end. Many thanks to all of my family for your continued support and encouragement to pursue any and all of my dreams. Thank you to Dr. Stacey Gelsheimer for always being a shoulder to lean on. Finally thank you to ILKB Cambridge and Upperkuts Boxing Club for keeping my stress levels at bay.

References

[1] John Whitmarsh and JA Govindjee. The photosynthetic process. *Concepts in Photobiology: Photosynthesis and Photomorphogenesis*, pages 11–51, 1999.

[2] Robert E Blankenship. Origin and early evolution of photosynthesis. *Photosynthesis Research*, 33(2):91–111, 1992.

[3] Alexandra Olaya-Castro, Chiu Fan Lee, Francesca Fassioli Olsen, and Neil F Johnson. Efficiency of energy transfer in a light-harvesting system under quantum coherence. *Physical Review B*, 78(8):085115, 2008.

[4] Gitt Panitchayangkoon, Dmitri V Voronine, Darius Abramavicius, Justin R Caram, Nicholas HC Lewis, Shaul Mukamel, and Gregory S Engel. Direct evidence of quantum transport in photosynthetic light-harvesting complexes. *Proceedings of the National Academy of Sciences*, 108(52):20908–20912, 2011.

[5] Xiche Hu, Thorsten Ritz, Ana Damjanović, Felix Autenrieth, and Klaus Schulten. Photosynthetic apparatus of purple bacteria. *Quarterly reviews of biophysics*, 35(1):1–62, 2002.

[6] Miroslav Z Papiz, Anna M Hawthornthwaite-Lawless, Steve M Prince, Gerry McDermott, Andy A Freer, Neil W Isaacs, and Richard J Cogdell. A model for the photosynthetic apparatus of purple bacteria. *Trends in Plant Science*, 1(6):198–206, 1996.

[7] Xiche Hu, Ana Damjanović, Thorsten Ritz, and Klaus Schulten. Architecture and mechanism of the light-harvesting apparatus of purple bacteria. *Proceedings of the National Academy of Sciences*, 95(11):5935–5941, 1998.

[8] Richard J Cogdell, Neil W Isaacs, Andy A Freer, Juan Arrelano, Tina D Howard, Miroslav Z Papiz, Anna M Hawthornthwaite-Lawless, and Stephen Prince. The structure and function of the lh2 (b800–850) complex from the purple photosynthetic bacterium rhodopseudomonas acidophila strain 10050. *Progress in biophysics and molecular biology*, 68(1):1–27, 1997.

[9] Leszek Fiedor, Agnieszka Kania, Beata Myśliwa-Kurdziel, Łukasz Orzeł, and Grażyna Stochel. Understanding chlorophylls: central magnesium ion and phytyl as structural determinants. *Biochimica et Biophysica Acta (BBA)-Bioenergetics*, 1777(12):1491–1500, 2008.

[10] HA Frank and RJ Cogdell. The photochemistry and function of carotenoids in photosynthesis. In *Carotenoids in photosynthesis*, pages 252–326. Springer, 1993.

[11] GJS Fowler, GD Sockalingum, B Robert, and CN Hunter. Blue shifts in bacteriochlorophyll absorbance correlate with changed hydrogen bonding patterns in light-harvesting 2 mutants of rhodobacter sphaeroides with alterations at α-tyr-44 and α-tyr-45. *Biochemical Journal*, 299(3):695–700, 1994.

[12] Camille Mascle-Allemand, Katia Duquesne, Regine Lebrun, Simon Scheuring, and James N Sturgis. Antenna mixing in photosynthetic membranes from phaeospirillum molischianum. *Proceedings of the National Academy of Sciences*, 107(12):5357–5362, 2010.

[13] Camille Mascle-Allemand, Jérôme Lavergne, Alain Bernadac, and James N Sturgis. Organisation and function of the phaeospirillum molischianum photosynthetic apparatus. *Biochimica et Biophysica Acta (BBA)-Bioenergetics*, 1777(12):1552–1559, 2008.

[14] K McLuskey, SM Prince, RJ Cogdell, and NW Isaacs. The crystallographic structure of the b800-820 lh3 light-harvesting complex from the purple bacteria rhodopseudomonas acidophila strain 7050. *Biochemistry*, 40(30):8783–8789, 2001.

[15] Geurt Deinum, Stephan CM Otte, Alastair T Gardiner, Thijs J Aartsma, Richard J Cogdell, and Jan Amesz. Antenna organization of rhodopseudomonas acidophila: a study of the excitation migration. *Biochimica et Biophysica Acta (BBA)-Bioenergetics*, 1060(1):125–131, 1991.

[16] Richard J Cogdell, Andrew Gall, and Jürgen Köhler. The architecture and function of the light-harvesting apparatus of purple bacteria: from single molecules to in vivo membranes. *Quarterly Reviews of Biophysics*, 39(3):227–324, 2006.

[17] SM Prince, TD Howard, DAA Myles, C Wilkinson, MZ Papiz, AA Freer, RJ Cogdell, and NW Isaacs. Detergent structure in crystals of the integral membrane light-harvesting complex lh2 from rhodopseudomonas acidophila strain 10050. *Journal of molecular biology*, 326(1):307–315, 2003.

[18] Thomas Walz, Stuart J Jamieson, Claire M Bowers, Per A Bullough, and C Neil Hunter. Projection structures of three photosynthetic complexes from rhodobacter sphaeroides: Lh2 at 6 å, lh1 and rc-lh1 at 25 å. *Journal of molecular biology*, 282(4):833–845, 1998.

[19] H Komiya, TO Yeates, DC Rees, James Paul Allen, and G Feher. Structure of the reaction center from rhodobacter sphaeroides r-26 and 2.4. 1: symmetry relations and sequence comparisons between different species. *Proceedings of the National Academy of Sciences*, 85(23):9012–9016, 1988.

[20] Juergen Koepke, Xiche Hu, Cornelia Muenke, Klaus Schulten, and Hartmut Michel. The crystal structure of the light-harvesting complex ii (b800–850) from rhodospirillum molischianum. *Structure*, 4(5):581–597, 1996.

[21] Richard J Cogdell and Hugo Scheer. Circular dichroism of light-harvesting complexes from purple photosynthetic bacteria. *Photochemistry and photobiology*, 42(6):669–678, 1985.

[22] Iwan Bissig, René A Brunisholz, Franz Suter, Richard J Cogdell, and Herbert Zuber. The complete amino acid sequences of the b 800—850 antenna polypeptides from rhodopseudomonas acidophila strain 7750. *Zeitschrift für Naturforschung C*, 43(1-2):77–83, 1988.

[23] René A Brunisholz and Herbert Zuber. Structure, function and organization of antenna polypeptides and antenna complexes from the three families of rhodospirillaneae. *Journal of Photochemistry and Photobiology B: Biology*, 15(1-2):113–140, 1992.

[24] James N Sturgis, Vladimira Jirsakova, Francoise Reiss-Husson, Richard J Cogdell, and Bruno Robert. Structure and properties of the bacteriochlorophyll binding site in peripheral light-harvesting complexes of purple bacteria. *Biochemistry*, 34(2):517–523, 1995.

[25] James N Sturgis and B Robert. Pigment binding-site and electronic properties in light-harvesting proteins of purple bacteria. *The Journal of Physical Chemistry B*, 101(37):7227–7231, 1997.

[26] E Gudowska-Nowak, MD Newton, and J Fajer. Conformational and environmental effects on bacteriochlorophyll optical spectra: correlations of calculated spectra with structural results. *Journal of Physical Chemistry*, 94(15):5795–5801, 1990.

[27] DE Tronrud, MF Schmid, and BW Matthews. Structure and x-ray amino acid sequence of a bacteriochlorophyll a protein from prosthecochloris aestuarii refined at 1.9 å resolution. *Journal of molecular biology*, 188(3):443–454, 1986.

[28] Elad Harel and Gregory S Engel. Quantum coherence spectroscopy reveals complex dynamics in bacterial light-harvesting complex 2 (lh2). *Proceedings of the National Academy of Sciences*, 109(3):706–711, 2012.

[29] Villy Sundström, Tõnu Pullerits, and Rienk van Grondelle. Photosynthetic light-harvesting: reconciling dynamics and structure of purple bacterial lh2 reveals function of photosynthetic unit, 1999.

[30] S Hess, M Chachisvilis, K Timpmann, MR Jones, GJ Fowler, CN Hunter, and V Sundström. Temporally and spectrally resolved subpicosecond energy transfer within the peripheral antenna complex (lh2) and from lh2 to the core antenna complex in photosynthetic purple bacteria. *Proceedings of the National Academy of Sciences*, 92(26):12333–12337, 1995.

[31] John TM Kennis, Alexandre M Streltsov, Simone IE Vulto, Thijs J Aartsma, Tsunenori Nozawa, and Jan Amesz. Femtosecond dynamics in isolated lh2 complexes of various species of purple bacteria. *The Journal of Physical Chemistry B*, 101(39):7827–7834, 1997.

[32] Rienk van Grondelle, Jan P Dekker, Tomas Gillbro, and Villy Sundstrom. Energy transfer and trapping in photosynthesis. *Biochimica et Biophysica Acta (BBA)-Bioenergetics*, 1187(1):1–65, 1994.

[33] Sussan Hess, Felix Feldchtein, Alexey Babin, Ildus Nurgaleev, Tonu Pullerits, Alexander Sergeev, and Villy Sundström. Femtosecond energy transfer within the lh2 peripheral antenna of the photosynthetic purple bacteria rhodobacter sphaeroides and rhodopseudomonas palustris ll. *Chemical physics letters*, 216(3-6):247–257, 1993.

[34] Peter D Dahlberg, Graham J Norris, Cheng Wang, Subha Viswanathan, Ved P Singh, and Gregory S Engel. Communication: coherences observed in vivo in photosynthetic bacteria using two-dimensional electronic spectroscopy, 2015.

[35] Tobias J Pflock, Silke Oellerich, June Southall, Richard J Cogdell, G Matthias Ullmann, and Jurgen Kohler. The electronically excited states of lh2 complexes from rhodopseudomonas acidophila strain 10050 studied by time-resolved spectroscopy and dynamic monte carlo simulations. i. isolated, non-interacting lh2 complexes. *The Journal of Physical Chemistry B*, 115(28):8813–8820, 2011.

[36] Kou Timpmann, Neal W Woodbury, and Arvi Freiberg. Unraveling exciton relaxation and energy transfer in lh2 photosynthetic antennas. *The Journal of Physical Chemistry B*, 104(42):9769–9771, 2000.

[37] JK Trautman, AP Shreve, CA Violette, Harry A Frank, TG Owens, and AC Albrecht. Femtosecond dynamics of energy transfer in b800-850 light-harvesting complexes of rhodobacter sphaeroides. *Proceedings of the National Academy of Sciences*, 87(1):215–219, 1990.

[38] S Hess, E Akesson, RJ Cogdell, T Pullerits, and V Sundström. Energy transfer in spectrally inhomogeneous light-harvesting pigment-protein complexes of purple bacteria. *Biophysical Journal*, 69(6):2211–2225, 1995.

[39] R Van Grondelle, H Bergström, V Sundström, and T Gillbro. Energy transfer within the bacteriochlorophyll antenna of purple bacteria at 77 k, studied by picosecond absorption recovery. *Biochimica et Biophysica Acta-Bioenergetics*, 894(2):313–326, 1987.

[40] Koichiro Mukai, Shuji Abe, and Hitoshi Sumi. Theory of rapid excitation-energy transfer from b800 to optically-forbidden exciton states of b850 in the antenna system lh2 of photosynthetic purple bacteria. *The Journal of Physical Chemistry B*, 103(29):6096–6102, 1999.

[41] Taiha Joo, Yiwei Jia, Jae-Young Yu, David M Jonas, and Graham R Fleming. Dynamics in isolated bacterial light harvesting antenna (lh2) of rhodobacter sphaeroides at room temperature. *The Journal of Physical Chemistry*, 100(6):2399–2409, 1996.

[42] Jevgenij Chmeliov, Egidijus Songaila, Olga Rancova, Andrew Gall, Bruno Robert, Darius Abramavicius, and Leonas Valkunas. Excitons in the lh3 complexes from purple bacteria. *The Journal of Physical Chemistry B*, 117(38):11058–11068, 2013.

[43] Anne-Marie Carey, Kirsty Hacking, Nichola Picken, Suvi Honkanen, Sharon Kelly, Dariusz M Niedzwiedzki, Robert E Blankenship, Yuuki Shimizu, Zheng-Yu Wang-Otomo, and Richard J Cogdell. Characterisation of the lh2 spectral variants produced by the photosynthetic purple sulphur bacterium allochromatium vinosum. *Biochimica et Biophysica Acta (BBA)-Bioenergetics*, 1837(11):1849–1860, 2014.

[44] Donatas Zigmantas, Elizabeth L Read, Tomáš Mančal, Tobias Brixner, Alastair T Gardiner, Richard J Cogdell, and Graham R Fleming. Two-dimensional electronic spectroscopy of the b800–b820 light-harvesting complex. *Proceedings of the National Academy of Sciences*, 103(34):12672–12677, 2006.

[45] Mark B Evans, Anna M Hawthornthwaite, and Richard J Cogdell. Isolation and characterisation of the different b800–850 light-harvesting complexes from low-and high-light grown cells of rhodopseudomonas palustris, strain 2.1. 6. *Biochimica et Biophysica Acta (BBA)-Bioenergetics*, 1016(1):71–76, 1990.

[46] John I Ogren, Ashley L Tong, Samuel C Gordon, Aurélia Chenu, Yue Lu, Robert E Blankenship, Jianshu Cao, and Gabriela S Schlau-Cohen. Impact of the lipid bilayer on energy transfer kinetics in the photosynthetic protein lh2. *Chemical science*, 9(12):3095–3104, 2018.

[47] Andrew F Fidler, Ved P Singh, Phillip D Long, Peter D Dahlberg, and Gregory S Engel. Probing energy transfer events in the light harvesting complex 2 (lh2) of rhodobacter sphaeroides with two-dimensional spectroscopy. *The Journal of chemical physics*, 139(15):10B614_1, 2013.

[48] Ralph Jimenez, Srivatsan N Dikshit, Stephen E Bradforth, and Graham R Fleming. Electronic excitation transfer in the lh2 complex of rhodobacter sphaeroides. *The Journal of Physical Chemistry*, 100(16):6825–6834, 1996.

[49] JL Herek, NJ Fraser, T Pullerits, P Martinsson, T Polivka, H Scheer, RJ Cogdell, and V Sundström. B800→ b850 energy transfer mechanism in bacterial lh2 complexes investigated by b800 pigment exchange. *Biophysical journal*, 78(5):2590–2596, 2000.

[50] Tõnu Pullerits, Susan Hess, Jennifer L Herek, and Villy Sundström. Temperature dependence of excitation transfer in lh2 of rhodobacter sphaeroides. *The Journal of Physical Chemistry B*, 101(49):10560–10567, 1997.

[51] René Monshouwer, Iñaki Ortiz de Zarate, Frank van Mourik, and Rienk van Grondelle. Low-intensity pump-probe spectroscopy on the b800 to b850 transfer in the light harvesting 2 complex of rhodobacter sphaeroides. *Chemical physics letters*, 246(3):341–346, 1995.

[52] Jante M Salverda, Frank van Mourik, Gert van der Zwan, and Rienk van Grondelle. Energy transfer in the b800 rings of the peripheral bacterial light-harvesting complexes of rhodopseudomonas acidophila and rhodospirillum molischianum studied with photon echo techniques. *The Journal of Physical Chemistry B*, 104(47):11395–11408, 2000.

[53] Janne A Ihalainen, Juha Linnanto, Pasi Myllyperkiö, Ivo HM van Stokkum, Beate Ücker, Hugo Scheer, and Jouko EI Korppi-Tommola. Energy transfer in lh2 of rhodospirillum m olischianum, studied by subpicosecond spectroscopy and configuration interaction exciton calculations. *The Journal of Physical Chemistry B*, 105(40):9849–9856, 2001.

[54] Markus Wendling, Frank van Mourik, Ivo HM van Stokkum, Jante M Salverda, Hartmut Michel, and Rienk van Grondelle. Low-intensity pump-probe measurements on the b800 band of rhodospirillum molischianum. *Biophysical journal*, 84(1):440–449, 2003.

[55] H-M Wu, NRS Reddy, RJ Cogdell, C Muenke, H Michel, and GJ Small. A comparison of the lh2 antenna complex of three purple bacteria by hole burning and absorption spectroscopes. *Molecular Crystals and Liquid Crystals Science and Technology. Section A. Molecular Crystals and Liquid Crystals*, 291(1):163–173, 1996.

[56] C De Caro, RW Visschers, R Van Grondelle, and S Völker. Inter-and intraband energy transfer in lh2-antenna complexes of purple bacteria. a fluorescence line-narrowing and hole-burning study. *The Journal of Physical Chemistry*, 98(41):10584–10590, 1994.

[57] Ying-Zhong Ma, Richard J Cogdell, and Tomas Gillbro. Femtosecond energy-transfer dynamics between bacteriochlorophylls in the b800- 820 antenna complex of the photosynthetic purple bacterium rhodopseudomonas acidophila (strain 7750). *The Journal of Physical Chemistry B*, 102(5):881–887, 1998.

[58] Martijn Ketelaars, Jean-Manuel Segura, Silke Oellerich, Ward PF de Ruijter, Gerhard Magis, Thijs J Aartsma, Michio Matsushita, Jan Schmidt, Richard J Cogdell, and Jürgen Köhler. Probing the electronic structure and conformational flexibility of individual light-harvesting 3 complexes by optical single-molecule spectroscopy. *The Journal of Physical Chemistry B*, 110(37):18710–18717, 2006.

[59] Th Forster. Delocalization excitation and excitation transfer. *Modern quantum chemistry*, 1965.

[60] Markus Schröder, Ulrich Kleinekathöfer, and Michael Schreiber. Calculation of absorption spectra for light-harvesting systems using non-markovian approaches as well as modified redfield theory. *The Journal of chemical physics*, 124(8):084903, 2006.

[61] MHC Koolhaas, RN Frese, GJS Fowler, TS Bibby, S Georgakopoulou, G Van der Zwan, CN Hunter, and R Van Grondelle. Identification of the upper exciton component of the b850 bacteriochlorophylls of the lh2 antenna complex, using a b800-free mutant of rhodobacter sphaeroides. *Biochemistry*, 37(14):4693–4698, 1998.

[62] Vladimir Novoderezhkin, Markus Wendling, and Rienk Van Grondelle. Intra-and interband transfers in the b800- b850 antenna of rhodospirillum m olischianum: Redfield theory model-

ing of polarized pump- probe kinetics. *The Journal of Physical Chemistry B*, 107(41):11534–11548, 2003.

[63] O Zerlauskiene, G Trinkunas, A Gall, B Robert, V Urboniene, and L Valkunas. Static and dynamic protein impact on electronic properties of light-harvesting complex lh2. *The Journal of Physical Chemistry B*, 112(49):15883–15892, 2008.

[64] Melih Şener, Johan Strümpfer, Jen Hsin, Danielle Chandler, Simon Scheuring, C Neil Hunter, and Klaus Schulten. Förster energy transfer theory as reflected in the structures of photosynthetic light-harvesting systems. *ChemPhysChem*, 12(3):518–531, 2011.

[65] Annela M Seddon, Paul Curnow, and Paula J Booth. Membrane proteins, lipids and detergents: not just a soap opera. *Biochimica et Biophysica Acta (BBA)-Biomembranes*, 1666(1):105–117, 2004.

[66] Charles Tanford and Jacqueline A Reynolds. Characterization of membrane proteins in detergent solutions. *Biochimica et Biophysica Acta (BBA)-Reviews on Biomembranes*, 457(2):133–170, 1976.

[67] Niall J Fraser, Peter J Dominy, Beaté Ücker, Ingrid Simonin, Hugo Scheer, and Richard J Cogdell. Selective release, removal, and reconstitution of bacteriochlorophyll a molecules into the b800 sites of lh2 complexes from rhodopseudomonas acidophila 10050. *Biochemistry*, 38(30):9684–9692, 1999.

[68] Arvi Freiberg, Margus Rätsep, and Kõu Timpmann. A comparative spectroscopic and kinetic study of photoexcitations in detergent-isolated and membrane-embedded lh2 light-harvesting complexes. *Biochimica et Biophysica Acta (BBA)-Bioenergetics*, 1817(8):1471–1482, 2012.

[69] Erwin London and H Gobind Khorana. Denaturation and renaturation of bacteriorhodopsin in detergents and lipid-detergent mixtures. *Journal of Biological Chemistry*, 257(12):7003–7011, 1982.

[70] Larry T Mimms, Guido Zampighi, Yasuhiko Nozaki, Charles Tanford, and Jacqueline A Reynolds. Phospholipid vesicle formation and transmembrane protein incorporation using octyl glucoside. *Biochemistry*, 20(4):833–840, 1981.

[71] J-L Rigaud. Membrane proteins: functional and structural studies using reconstituted proteoliposomes and 2-d crystals. *Brazilian Journal of Medical and Biological Research*, 35(7):753–766, 2002.

[72] Tobias Pflock, Manuela Dezi, Giovanni Venturoli, Richard J Cogdell, Jürgen Köhler, and Silke Oellerich. Comparison of the fluorescence kinetics of detergent-solubilized and membrane-reconstituted lh2 complexes from rps. acidophila and rb. sphaeroides. *Photosynthesis research*, 95(2-3):291–298, 2008.

[73] Ismael Moya, Mariuccia Silvestri, Olivier Vallon, Gianfelice Cinque, and Roberto Bassi. Time-resolved fluorescence analysis of the photosystem ii antenna proteins in detergent micelles and liposomes. *Biochemistry*, 40(42):12552–12561, 2001.

[74] John D Olsen, Jaimey D Tucker, John A Timney, Pu Qian, Cvetelin Vassilev, and C Neil Hunter. The organization of lh2 complexes in membranes from rhodobacter sphaeroides. *Journal of Biological Chemistry*, 283(45):30772–30779, 2008.

[75] Danielle E Chandler, Johan Strümpfer, Melih Sener, Simon Scheuring, and Klaus Schulten. Light harvesting by lamellar chromatophores in rhodospirillum photometricum. *Biophysical journal*, 106(11):2503–2510, 2014.

[76] Fan Yang, Long-Jiang Yu, Peng Wang, Xi-Cheng Ai, Zheng-Yu Wang, and Jian-Ping Zhang. Effects of aggregation on the excitation dynamics of lh2 from thermochromatium tepidum in aqueous phase and in chromatophores. *The Journal of Physical Chemistry B*, 115(24):7906–7913, 2011.

[77] Willem HJ Westerhuis, Marcel Vos, Rienk van Grondelle, Jan Amesz, and Robert A Niederman. Altered organization of light-harvesting complexes in phospholipid-enriched rhodobacter sphaeroides chromatophores as determined by fluorescence yield and singlet-singlet annihilation measurements. *Biochimica et Biophysica Acta (BBA)-Bioenergetics*, 1366(3):317–329, 1998.

[78] B Driscoll, C Lunceford, S Lin, K Woronowicz, RA Niederman, and NW Woodbury. Energy transfer properties of rhodobacter sphaeroides chromatophores during adaptation to low light intensity. *Physical Chemistry Chemical Physics*, 16(32):17133–17141, 2014.

[79] C Neil Hunter, Hans Bergstroem, Rienk Van Grondelle, and Villy Sundstroem. Energy-transfer dynamics in three light-harvesting mutants of rhodobacter sphaeroides: a picosecond spectroscopy study. *Biochemistry*, 29(13):3203–3207, 1990.

[80] Timothy H Bayburt and Stephen G Sligar. Membrane protein assembly into nanodiscs. *FEBS letters*, 584(9):1721–1727, 2010.

[81] Ilia G Denisov, Yelena V Grinkova, Anne A Lazarides, and Sephen G Sligar. Directed self-assembly of monodisperse phospholipid bilayer nanodiscs with controlled size. *Journal of the American Chemical Society*, 126(11):3477–3487, 2004.

[82] Abhinav Nath, William M Atkins, and Stephen G Sligar. Applications of phospholipid bilayer nanodiscs in the study of membranes and membrane proteins. *Biochemistry*, 46(8):2059–2069, 2007.

[83] Thomas Boldog, Stephen Grimme, Mingshan Li, Stephen G Sligar, and Gerald L Hazelbauer. Nanodiscs separate chemoreceptor oligomeric states and reveal their signaling properties. *Proceedings of the National Academy of Sciences*, 103(31):11509–11514, 2006.

[84] Ilia G Denisov and Stephen G Sligar. Nanodiscs in membrane biochemistry and biophysics. *Chemical Reviews*, 117(6):4669–4713, 2017.

[85] Maryvonne ROSSENEU, Philippe VAN TORNOUT, Marie-José LIEVENS, Gerd SCHMITZ, and Gerd ASSMANN. Dissociation of apolipoprotein ai from apoprotein-lipid complexes and from high-density lipoproteins: A fluorescence study. *European journal of biochemistry*, 128(2-3):455–460, 1982.

[86] Timothy H Bayburt, Yelena V Grinkova, and Stephen G Sligar. Self-assembly of discoidal phospholipid bilayer nanoparticles with membrane scaffold proteins. *Nano Letters*, 2(8):853–856, 2002.

[87] TK Ritchie, YV Grinkova, TH Bayburt, IG Denisov, JK Zolnerciks, WM Atkins, and SG Sligar. Chapter eleven-reconstitution of membrane proteins in phospholipid bilayer nanodiscs. *Methods in Enzymology*, 464:211–231, 2009.

[88] Nicholas Skar-Gislinge, Nicolai Tidemand Johansen, Rasmus Høiberg-Nielsen, and Lise Arleth. Comprehensive study of the self-assembly of phospholipid nanodiscs: What determines their shape and stoichiometry? *Langmuir*, 34(42):12569–12582, 2018.

[89] Rongfu Zhang, Indra D Sahu, Lishan Liu, Anna Osatuke, Raven G Comer, Carole Dabney-Smith, and Gary A Lorigan. Characterizing the structure of lipodisq nanoparticles for membrane protein spectroscopic studies. *Biochimica et Biophysica Acta-Biomembranes*, 1848(1):329–333, 2015.

[90] Franz Hagn, Manuel Etzkorn, Thomas Raschle, and Gerhard Wagner. Optimized phospholipid bilayer nanodiscs facilitate high-resolution structure determination of membrane proteins. *Journal of the American Chemical Society*, 135(5):1919–1925, 2013.

[91] Timothy H Bayburt, Yelena V Grinkova, and Stephen G Sligar. Assembly of single bacteriorhodopsin trimers in bilayer nanodiscs. *Archives of biochemistry and biophysics*, 450(2):215–222, 2006.

[92] Craig D Blanchette, Richard Law, W Henry Benner, Joseph B Pesavento, Jenny A Cappuccio, Vicki Walsworth, Edward A Kuhn, Michele Corzett, Brett A Chromy, Brent W Segelke, et al. Quantifying size distributions of nanolipoprotein particles with single-particle analysis and molecular dynamic simulations. *Journal of lipid research*, 49(7):1420–1430, 2008.

[93] Oscar D Bello, Sarah M Auclair, James E Rothman, and Shyam S Krishnakumar. Using apoe nanolipoprotein particles to analyze snare-induced fusion pores. *Langmuir*, 32(12):3015–3023, 2016.

[94] Wei He, Juntao Luo, Feliza Bourguet, Li Xing, Sun K Yi, Tingjuan Gao, Craig Blanchette, Paul T Henderson, Edward Kuhn, Mike Malfatti, et al. Controlling the diameter, monodispersity, and solubility of apoa1 nanolipoprotein particles using telodendrimer chemistry. *Protein Science*, 22(8):1078–1086, 2013.

[95] Vincent Postis, Shaun Rawson, Jennifer K Mitchell, Sarah C Lee, Rosemary A Parslow, Tim R Dafforn, Stephen A Baldwin, and Stephen P Muench. The use of smalps as a novel membrane protein scaffold for structure study by negative stain electron microscopy. *Biochimica et Biophysica Acta (BBA)-Biomembranes*, 1848(2):496–501, 2015.

[96] Marcella C Orwick, Peter J Judge, Jan Procek, Ljubica Lindholm, Andrea Graziadei, Andreas Engel, Gerhard Gröbner, and Anthony Watts. Detergent-free formation and physicochemical characterization of nanosized lipid–polymer complexes: Lipodisq. *Angewandte Chemie International Edition*, 51(19):4653–4657, 2012.

[97] Alvin CK Teo, Sarah C Lee, Naomi L Pollock, Zoe Stroud, Stephen Hall, Alpesh Thakker, Andrew R Pitt, Timothy R Dafforn, Corinne M Spickett, and David I Roper. Analysis of smalp co-extracted phospholipids shows distinct membrane environments for three classes of bacterial membrane protein. *Scientific reports*, 9(1):1813, 2019.

[98] Mahmoud L Nasr, Diego Baptista, Mike Strauss, Zhen-Yu J Sun, Simina Grigoriu, Sonja Huser, Andreas Plückthun, Franz Hagn, Thomas Walz, James M Hogle, et al. Covalently circularized nanodiscs for studying membrane proteins and viral entry. *Nature methods*, 14(1):49, 2017.

[99] Martin F Richter, Jürgen Baier, Richard J Cogdell, Jürgen Köhler, and Silke Oellerich. Single-molecule spectroscopic characterization of light-harvesting 2 complexes reconstituted into model membranes. *Biophysical Journal*, 93(1):183–191, 2007.

[100] Kou Timpmann, Aleksandr Ellervee, Tonu Pullerits, Rein Ruus, Villy Sundström, and Arvi Freiberg. Short-range exciton couplings in lh2 photosynthetic antenna proteins studied by high hydrostatic pressure absorption spectroscopy. *The Journal of Physical Chemistry B*, 105(35):8436–8444, 2001.

[101] James L Banal, Toru Kondo, Remi Veneziano, Mark Bathe, and Gabriela S Schlau-Cohen. Photophysics of j-aggregate-mediated energy transfer on dna. *The journal of physical chemistry letters*, 8(23):5827–5833, 2017.

[102] Lu-Ning Liu, Thijs J Aartsma, and Raoul N Frese. Dimers of light-harvesting complex 2 from rhodobacter sphaeroides characterized in reconstituted 2d crystals with atomic force microscopy. *The FEBS Journal*, 275(12):3157–3166, 2008.

[103] GM McDermott, SM Prince, AA Freer, AM Hawthornthwaite-Lawless, and et al. Crystal structure of an integral membrane light-harvesting complex from photosynthetic bacteria. *Nature*, 374(6522):517, 1995.

[104] Miroslav Z Papiz, Steve M Prince, Tina Howard, Richard J Cogdell, and Neil W Isaacs. The structure and thermal motion of the b800–850 lh2 complex from rps. acidophila at 2.0 å resolution and 100k: new structural features and functionally relevant motions. *Journal of Molecular Biology*, 326(5):1523–1538, 2003.

[105] Seogjoo Jang, Marshall D Newton, and Robert J Silbey. Multichromophoric förster resonance energy transfer. *Physical Review Letters*, 92(21):218301, 2004.

[106] Liam Cleary and Jianshu Cao. Optimal thermal bath for robust excitation energy transfer in disordered light-harvesting complex 2 of purple bacteria. *New Journal of Physics*, 15(12):125030, 2013.

[107] Svetlana Bahatyrova, Raoul N Frese, A Siebert, John D Olsen, Kees O van der Werf, Rienk van Grondelle, Robert A Niederman, Per A Bullough, Cees Otto, and C Neil Hunter. The native architecture of a photosynthetic membrane. *Nature*, 430(7003):1058–1062, 2004.

[108] TO Yeates, H Komiya, DC Rees, JP Allen, and G Feher. Structure of the reaction center from rhodobacter sphaeroides r-26: membrane-protein interactions. *Proceedings of the National Academy of Sciences*, 84(18):6438–6442, 1987.

[109] John F Nagle and Stephanie Tristram-Nagle. Structure of lipid bilayers. *Biochimica et Biophysica Acta-Reviews on Biomembranes*, 1469(3):159–195, 2000.

[110] Vadim Cherezov, Jeffrey Clogston, Miroslav Z Papiz, and Martin Caffrey. Room to move: crystallizing membrane proteins in swollen lipidic mesophases. *Journal of Molecular Biology*, 357(5):1605–1618, 2006.

[111] PA Timmins, M Leonhard, HU Weltzien, T Wacker, and W Welte. A physical characterization of some detergents of potential use for membrane protein crystallization. *FEBS Letters*, 238(2):361–368, 1988.

[112] M Roth, A Lewit-Bentley, H Michel, J Deisenhofer, R Huber, and D Oesterhelt. Detergent structure in crystals of a bacterial photosynthetic reaction centre. *Nature*, 340(6235):659–662, 1989.

[113] JA Lundbaek, P Birn, J Girshman, AJ Hansen, and OS Andersen. Membrane stiffness and channel function. *Biochemistry*, 35(12):3825–3830, 1996.

[114] Michael F Brown. Modulation of rhodopsin function by properties of the membrane bilayer. *Chemistry and Physics of Lipids*, 73(1):159–180, 1994.

[115] Melih Şener, Johan Strümpfer, John A Timney, Arvi Freiberg, C Neil Hunter, and Klaus Schulten. Photosynthetic vesicle architecture and constraints on efficient energy harvesting. *Biophysical Journal*, 99(1):67–75, 2010.

[116] Erik Lindahl and Olle Edholm. Spatial and energetic-entropic decomposition of surface tension in lipid bilayers from molecular dynamics simulations. *The Journal of Chemical Physics*, 113(9):3882–3893, 2000.

[117] Daniel Harries and Avinoam Ben-Shaul. Conformational chain statistics in a model lipid bilayer: comparison between mean field and monte carlo calculations. *The Journal of Chemical Physics*, 106(4):1609–1619, 1997.

[118] Robert S Cantor. The lateral pressure profile in membranes: a physical mechanism of general anesthesia. *Biochemistry*, 36(9):2339–2344, 1997.

[119] Robert S Cantor. Size distribution of barrel-stave aggregates of membrane peptides: influence of the bilayer lateral pressure profile. *Biophysical Journal*, 82(5):2520–2525, 2002.

[120] J Antoinette Killian, Ben de Kruijff, and et al. Nonbilayer lipids affect peripheral and integral membrane proteins via changes in the lateral pressure profile. *Biochimica et Biophysica Acta-Biomembranes*, 1666(1):275–288, 2004.

[121] S Scarlata. The effect of hydrostatic pressure on membrane-bound proteins. *Brazilian Journal of mMedical and Biological Research*, 38(8):1203–1208, 2005.

[122] Markus R Wenk, Thomas Alt, Anna Seelig, and Joachim Seelig. Octyl-beta-d-glucopyranoside partitioning into lipid bilayers: thermodynamics of binding and structural changes of the bilayer. *Biophysical Journal*, 72(4):1719–1731, 1997.

[123] Parveen Akhtar, Márta Dorogi, Krzysztof Pawlak, László Kovács, Attila Bóta, Terëz Kiss, Győző Garab, and Petar H Lambrev. Pigment interactions in light-harvesting complex ii in different molecular environments. *Journal of Biological Chemistry*, 290(8):4877–4886, 2015.

[124] Xing-Hai Chen, Lei Zhang, Yu-Xiang Weng, Lu-Chao Du, Man-Ping Ye, Guo-Zhen Yang, Ritsuko Fujii, Ferdy S Rondonuwu, Yasushi Koyama, Yi-Shi Wu, and et al. Protein structural deformation induced lifetime shortening of photosynthetic bacteria light-harvesting complex lh2 excited state. *Biophysical Journal*, 88(6):4262–4273, 2005.

[125] Anjali Pandit, Michael Reus, Tomas Morosinotto, Roberto Bassi, Alfred R Holzwarth, and Huub JM de Groot. An nmr comparison of the light-harvesting complex ii (lhcii) in active and photoprotective states reveals subtle changes in the chlorophyll a ground-state electronic structures. *Biochimica et Biophysica Acta (BBA)-Bioenergetics*, 1827(6):738–744, 2013.

[126] Emanuela Crisafi and Anjali Pandit. Disentangling protein and lipid interactions that control a molecular switch in photosynthetic light harvesting. *Biochimica et Biophysica Acta (BBA)-Biomembranes*, 1859(1):40–47, 2017.

[127] Anjali Pandit, Nazhat Shirzad-Wasei, Lucyna M Wlodarczyk, Henny van Roon, Egbert J Boekema, Jan P Dekker, and J Willem. Assembly of the major light-harvesting complex ii in lipid nanodiscs. *Biophysical Journal*, 101(10):2507–2515, 2011.

[128] Sofia Georgakopoulou, Raoul N Frese, Evelyn Johnson, Corline Koolhaas, Richard J Cogdell, Rienk van Grondelle, and Gert van der Zwan. Absorption and cd spectroscopy and modeling of various lh2 complexes from purple bacteria. *Biophysical Journal*, 82(4):2184–2197, 2002.

[129] Thomas Boldog, Mingshan Li, and Gerald L Hazelbauer. [14]-using nanodiscs to create water-soluble transmembrane chemoreceptors inserted in lipid bilayers. *Methods in Enzymology*, 423:317–335, 2007.

[130] Richard J Cogdell, Irene Durant, Jane Valentine, J Gordon Lindsay, and Karin Schmidt. The isolation and partial characterisation of the light-harvesting pigment-protein complement of rhodopseudomonas acidophila. *Biochimica et Biophysica Acta (BBA)-Bioenergetics*, 722(3):427–435, 1983.

[131] Yoshitaka Saga and Keiya Hirota. Determination of the molar extinction coefficients of the b800 and b850 absorption bands in light-harvesting complexes 2 derived from three purple photosynthetic bacteria rhodoblastus acidophilus, rhodobacter sphaeroides, and phaeospirillum molischianum by extraction of bacteriochlorophyll a. *Analytical Sciences*, 32(7):801–804, 2016.

[132] Kyriaki Kosma, Sergei A Trushin, Werner Fuß, and Wolfram E Schmid. Characterization of the supercontinuum radiation generated by self-focusing of few-cycle 800 nm pulses in argon. *Journal of Modern Optics*, 55(13):2141–2177, 2008.

[133] Boris Spokoyny, Christine J Koh, and Elad Harel. Stable and high-power few cycle supercontinuum for 2d ultrabroadband electronic spectroscopy. *Optics Letters*, 40(6):1014–1017, 2015.

[134] Harshad D Vishwasrao, Ahmed A Heikal, Karl A Kasischke, and Watt W Webb. Conformational dependence of intracellular nadh on metabolic state revealed by associated fluorescence anisotropy. *Journal of Biological Chemistry*, 280(26):25119–25126, 2005.

[135] Brent P Krueger, Gregory D Scholes, and Graham R Fleming. Calculation of couplings and energy-transfer pathways between the pigments of lh2 by the ab initio transition density cube method. *The Journal of Physical Chemistry B*, 102(27):5378–5386, 1998.

[136] Sergei Tretiak, Chris Middleton, Vladimir Chernyak, and Shaul Mukamel. Bacteriochlorophyll and carotenoid excitonic couplings in the lh2 system of purple bacteria. *The Journal of Physical Chemistry B*, 104(40):9540–9553, 2000.

[137] Hitoshi Sumi. Theory on rates of excitation-energy transfer between molecular aggregates through distributed transition dipoles with application to the antenna system in bacterial photosynthesis. *The Journal of Physical Chemistry B*, 103(1):252–260, 1999.

[138] Lucas MP Beekman, Frank van Mourik, Michael R Jones, H Matthieu Visser, C Neil Hunter, and Rienk van Grondelle. Trapping kinetics in mutants of the photosynthetic purple bac-

terium rhodobacter sphaeroides: influence of the charge separation rate and consequences for the rate-limiting step in the light-harvesting process. *Biochemistry*, 33(11):3143–3147, 1994.

[139] Graham R Fleming and Rienk van Grondelle. Femtosecond spectroscopy of photosynthetic light-harvesting systems. *Current opinion in structural biology*, 7(5):738–748, 1997.

[140] M Krikunova, A Kummrow, B Voigt, M Rini, H Lokstein, A Moskalenko, H Scheer, A Razjivin, and D Leupold. Fluorescence of native and carotenoid-depleted lh2 from chromatium minutissimum, originating from simultaneous two-photon absorption in the spectral range of the presumed (optically 'dark') s1 state of carotenoids. *FEBS letters*, 528(1-3):227–229, 2002.

[141] Daisuke Kosumi, Tomoko Horibe, Mitsuru Sugisaki, Richard J Cogdell, and Hideki Hashimoto. Photoprotection mechanism of light-harvesting antenna complex from purple bacteria. *The Journal of Physical Chemistry B*, 120(5):951–956, 2016.

[142] Harry A Frank. Spectroscopic studies of the low-lying singlet excited electronic states and photochemical properties of carotenoids. *Archives of biochemistry and biophysics*, 385(1):53–60, 2001.

[143] Simon Scheuring, Jean-Louis Rigaud, and James N Sturgis. Variable lh2 stoichiometry and core clustering in native membranes of rhodospirillum photometricum. *The EMBO journal*, 23(21):4127–4133, 2004.

[144] Tatas HP Brotosudarmo, Aaron M Collins, Andrew Gall, Aleksander W Roszak, Alastair T Gardiner, Robert E Blankenship, and Richard J Cogdell. The light intensity under which cells are grown controls the type of peripheral light-harvesting complexes that are assembled in a purple photosynthetic bacterium. *Biochemical Journal*, 440(1):51–61, 2011.

[145] James N Sturgis and Robert A Niederman. Atomic force microscopy reveals multiple patterns of antenna organization in purple bacteria: implications for energy transduction mechanisms and membrane modeling. *Photosynthesis research*, 95(2-3):269–278, 2008.

[146] James N Sturgis, Jaimey D Tucker, John D Olsen, C Neil Hunter, and Robert A Niederman. Atomic force microscopy studies of native photosynthetic membranes. *Biochemistry*, 48(17):3679–3698, 2009.

[147] Simon Scheuring, James N Sturgis, Valerie Prima, Alain Bernadac, Daniel Lévy, and Jean-Louis Rigaud. Watching the photosynthetic apparatus in native membranes. *Proceedings of the National Academy of Sciences*, 101(31):11293–11297, 2004.

[148] Simon Scheuring and James N Sturgis. Chromatic adaptation of photosynthetic membranes. *Science*, 309(5733):484–487, 2005.

[149] Ritesh Agarwal, Abbas H Rizvi, Bradley S Prall, John D Olsen, C Neil Hunter, and Graham R Fleming. Nature of disorder and inter-complex energy transfer in lh2 at room temperature: a three pulse photon echo peak shift study. *The Journal of Physical Chemistry A*, 106(33):7573–7578, 2002.

[150] JM Linnanto and JEI Korppi-Tommola. Modelling excitonic energy transfer in the photosynthetic unit of purple bacteria. *Chemical Physics*, 357(1-3):171–180, 2009.

[151] Mino Yang, Ritesh Agarwal, and Graham R Fleming. The mechanism of energy transfer in the antenna of photosynthetic purple bacteria. *Journal of Photochemistry and Photobiology A: Chemistry*, 142(2-3):107–119, 2001.

[152] Yee-Hung M Chan and Steven G Boxer. Model membrane systems and their applications. *Current opinion in chemical biology*, 11(6):581–587, 2007.

[153] Wang Dong and James N Sturgis. Making dimers of oligomeric membrane proteins using copper-free click chemistry. *F1000Research*, 5, 2016.

[154] Thomas Raschle, Chenxiang Lin, Ralf Jungmann, William M Shih, and Gerhard Wagner. Controlled co-reconstitution of multiple membrane proteins in lipid bilayer nanodiscs using dna as a scaffold. *ACS chemical biology*, 10(11):2448–2454, 2015.

[155] Chang Sun and Robert B Gennis. Single-particle cryo-em studies of transmembrane proteins in sma copolymer nanodiscs. *Chemistry and physics of lipids*, 2019.

[156] XP Xu, D Zhai, E Kim, M Swift, JC Reed, N Volkmann, and D Hanein. Three-dimensional structure of bax-mediated pores in membrane bilayers. *Cell death & disease*, 4(6):e683, 2013.

[157] Yuan Gao, Erhu Cao, David Julius, and Yifan Cheng. Trpv1 structures in nanodiscs reveal mechanisms of ligand and lipid action. *Nature*, 534(7607):347, 2016.

[158] Jens Frauenfeld, James Gumbart, Eli O Van Der Sluis, Soledad Funes, Marco Gartmann, Birgitta Beatrix, Thorsten Mielke, Otto Berninghausen, Thomas Becker, Klaus Schulten, et al. Cryo-em structure of the ribosome–secye complex in the membrane environment. *Nature structural & molecular biology*, 18(5):614, 2011.

[159] Soung-Hun Roh, Nicholas J Stam, Corey F Hryc, Sergio Couoh-Cardel, Grigore Pintilie, Wah Chiu, and Stephan Wilkens. The 3.5-å cryoem structure of nanodisc-reconstituted yeast vacuolar atpase vo proton channel. *Molecular cell*, 69(6):993–1004, 2018.

[160] Aurélia Chenu and Jianshu Cao. Construction of multichromophoric spectra from monomer data: Applications to resonant energy transfer. *Physical review letters*, 118(1):013001, 2017.

[161] Natanya R Civjan, Timothy H Bayburt, Mary A Schuler, and Stephen G Sligar. Direct solubilization of heterologously expressed membrane proteins by incorporation into nanoscale lipid bilayers. *Biotechniques*, 35(3):556–563, 2003.

[162] Thomas Boldog, Mingshan Li, and Gerald L Hazelbauer. Using nanodiscs to create water-soluble transmembrane chemoreceptors inserted in lipid bilayers. In *Methods in enzymology*, volume 423, pages 317–335. Elsevier, 2007.